

Article

# Nondestructive Ultrasonic Inspection of Composite Materials: A Comparative Advantage of Phased Array Ultrasonic

Hossein Taheri <sup>1,\*</sup> and Ahmed Arabi Hassen <sup>2,3</sup>

<sup>1</sup> Department of Manufacturing Engineering, Georgia Southern University, Statesboro, GA 30460, USA

<sup>2</sup> Manufacturing Demonstration Facility (MDF), Oak Ridge National Laboratory (ORNL), Knoxville, TN 37932, USA; hassena@ornl.gov

<sup>3</sup> Department of Mechanical, Aerospace and Biomedical Engineering, University of Tennessee, Estabrook Rd, Knoxville, TN 37916, USA

\* Correspondence: htaheri@georgiasouthern.edu; Tel.: +1-912-478-7463

Received: 17 March 2019; Accepted: 16 April 2019; Published: 19 April 2019

**Featured Application:** The featured application of the proposed study is to develop the application and describe the advantages of phased array ultrasonic technique for the inspection of composite materials. The proposed method not only enhances the probability of detection of the defects in composite materials, but also increases the distance over which the defects are detectable with a single inspection location.

**Abstract:** Carbon- and glass fiber-reinforced polymer (CFRP and GFRP) composite materials have been used in many industries such as aerospace and automobile because of their outstanding strength-to-weight ratio and corrosion resistance. The quality of these materials is important for safe operation. Nondestructive testing (NDT) techniques are an effective way to inspect these composites. While ultrasonic NDT has previously been used for inspection of composites, conventional ultrasonic NDT, using single element transducers, has limitations such as high attenuation and low signal-to-noise ratio (SNR). Using phased array ultrasonic testing (PAUT) techniques, signals can be generated at desired distances and angles. These capabilities provide promising results for composites where the anisotropic structure makes signal evaluation challenging. Defect detection in composites based on bulk and guided waves are studied. The capability of the PAUT and its sensitivity to flaws were evaluated by comparing the signal characteristics to the conventional method. The results show that flaw sizes as small as 0.8 mm with penetration depth up to 25 mm can be detected using PAUT, and the result signals have better characteristics than the conventional ultrasonic technique. In addition, it has been shown that guided wave generated by PAUT also has outstanding capability of flaw detection in composite materials.

**Keywords:** phased array ultrasonic; composites; signal sensitivity; defect detection; nondestructive testing (NDT)

## 1. Introduction

Carbon fiber-reinforced polymer (CFRP) and glass fiber-reinforced polymer (GFRP) composite materials are widely used in a variety of applications such as aerospace structures, wind turbine blades, the automotive industry, and mass transit [1–4]. Nondestructive testing/evaluation (NDT/E) and inspection of these materials are necessary to control the quality of the parts and inspect for anomalies in the structures to prevent catastrophic failure. Nondestructive techniques are widely used for material evaluation and flaw detection [5,6]. Ultrasonic testing is one of the most commonly

used NDT methods for various applications, where characteristics of ultrasonic signals, such as reflection and scattering of ultrasound waves, are used for material properties evaluation and flaw detection [5,7–10]. In ultrasonic testing, a piezoelectric transducer is commonly used for generation of compression or shear wave which are propagating through the inspected media. When these waves interact with media boundaries, they face reflection, transmission, and scattering from the boundaries [5]. These scattering characteristics, the speed of sound wave, and travelling time provide valuable information about the material properties and integrity. However, using conventional ultrasonic methods for composite inspection can be challenging due to the anisotropic nature of the composites structures [11–13]. Wave propagation in anisotropic composite structures is complex, and random scattering as well as high attenuation of ultrasonic waves reduce the probability of defect detection [14,15]. Several ultrasonic techniques have been used for inspection and characterization of composite materials. Castellano et. al. (2018) introduced a new experimental approach for the comparison between Quasi Static Indentation (QSI) damage and Low-Velocity Impact (LVI) damage in polymer composites starting from the results of ultrasonic goniometric immersion tests [16]. In their study, the differences and similarities between QSI and LVI damage starting from the analysis of the variations of the acoustic behavior and by using a suitable anisotropic damage model developed in the framework of the Continuum Damage Mechanics theory [16].

Phased array ultrasonic testing (PAUT) can overcome conventional ultrasonic method limitations by providing the capability of signal focusing and steering at desired angles and locations [17–19]. In PAUT, a series of ultrasonic elements in a phased array transducer can provide the option to activate each individual element in a programmed sequence [20,21]. A phased array unit includes a computer-based instrument capable of driving multielements, as well as receiving and digitizing the returning echoes based on the appropriate delay law for firing the elements. This is done by changing the time between the outgoing ultrasonic pulses of each element so that the superimposed wave front effectively steers and shapes the resultant final sound beam. This capability assists in generating the desired type of ultrasonic signal and improving the wave characteristics in comparison to the conventional single-element ultrasonic transducer. The PAUT method can also be used to generate guided waves [22–26]. Guided waves are another type of ultrasonic wave, which provide useable features for inspection of plate type structures. Guided waves can travel longer distances compared to the other types of ultrasonic waves and can cover more area of inspection, making faster inspections possible [19,27–29]. Chimenti (1997) comprehensively discussed the composite materials and their inspection and characterization using guided waves [30].

In this work, we first compare the defect detection capability and sensitivity of the PAUT signals with single element (conventional) ultrasonic (SEUT). The back wall reflection of bulk wave through the thickness of composite samples was used to study the signal characteristics of the PAUT and compare them with SEUT. The sensitivity of the signal to flaw detection was also studied using the response signal from the artificially made defects in composite parts. Next, guided wave modes were generated using the PAUT system for defect detection in sample plates. The guided waves generated using PAUT were used to show the feasibility of flaw detection on composite plates.

## 2. Materials and Sample Preparation

### 2.1. SEUT Versus PAUT Methods

GFRP plates, extracted from a wind turbine blade, were used for the experiments as shown in Figure 1a. The GFRP samples have various thicknesses of 4, 10, 12, 18, and 25 mm. In order to study the sensitivity of flaw detection in both the PAUT and SEUT methods, various sizes of holes were drilled on one side of the sample (with the largest thickness being 25 mm), as shown schematically in Figure 1b.

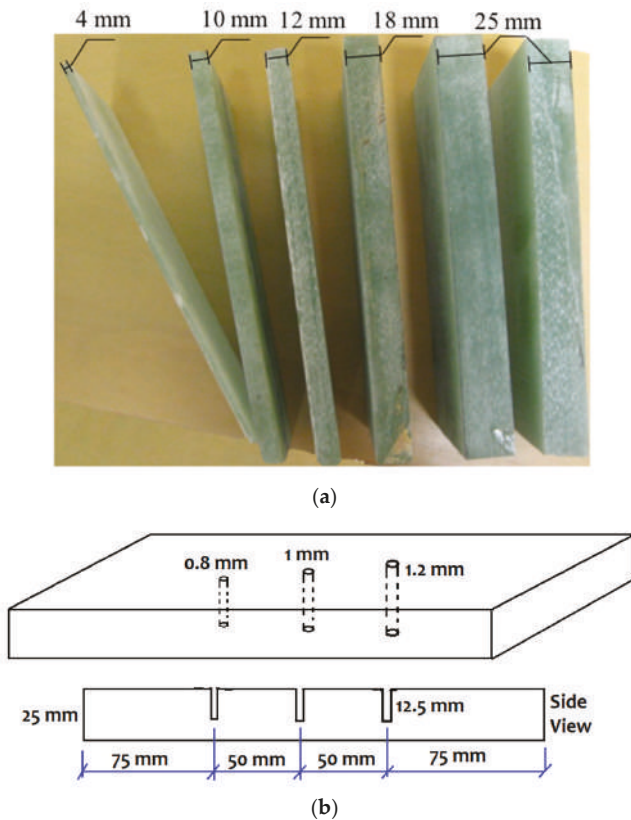


**Figure 1.** Samples used to evaluate capability and sensitivity of defect detection in single element ultrasonic (SEUT) versus phased array ultrasonic (PAUT) methods: (a) glass fiber reinforced polymer (GFRP) samples from a wind turbine blade and (b) schematic for the artificial hole locations in GFRP sample with 25mm thickness (Thk.). Sample size is 250 × 100 × 25 (L × W × Thk.) mm. Width of the sample is 100 mm and holes drilled in the middle of the width.

2.2. PAUT Guided Wave Method

Two different types of materials were used in this experiment, Aluminum (Al) and CFRP plates, as introduced in Table 1. The reason for selecting these materials for guided wave evaluation was that they were available in plate shape and desired thicknesses (in the range of 1 to 2 mm) for guided wave generation. For both Aluminum and CFRP samples, artificial defects, in the form of drilled holes, were made into the samples. Figure 2 shows a schematic for the location and depth of the artificial holes in both inspected samples.

**Table 1.** Test samples description used for the phased array ultrasonic (PAUT) guided wave method.

| Sample Name | Material  | Thickness (mm) |
|-------------|---|----------------|
| Al-1        | Aluminum 6063 (Plate)   | 2.2            |
| Al-2        | Aluminum 6063 (Plate)   | 0.635          |
| CFRP        | Unidirectional Carbon Fiber Composite (5 layers of carbon fiber fabric) | 1.0            |

### 3. Experimental Setup

#### 3.1. SEUT Versus PAUT Methods

It is important to understand how far an ultrasonic signal can travel through the composite material while the back wall reflection is still detectable. This shows the capability of signal focusing and propagation for an ultrasonic setup. The SEUT experiments were performed using three different frequencies including 0.5, 1.0, and 1.5 MHz, where the attenuation of ultrasound signals at different frequencies was evaluated. In the PAUT experiments, a 1.5 MHz, 16-element transducer was used accompanying the related normal wedge. Both SEUT and PAUT transducer and setups are shown in Figure 3.

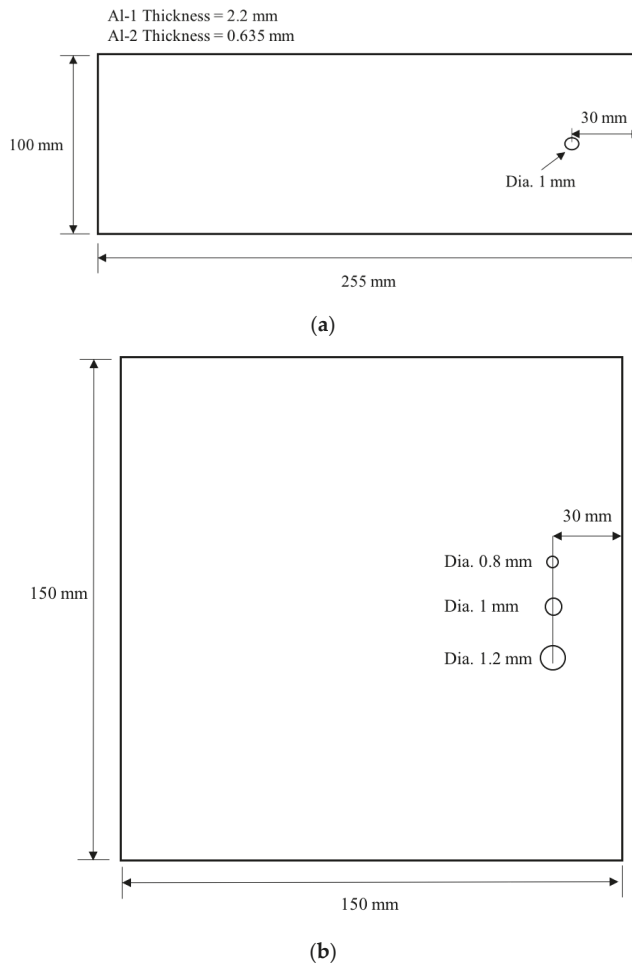


**Figure 2.** Schematic for the dimension and artificial holes locations in (a) Al-1 and Al-2 samples and (b) CFRP sample.

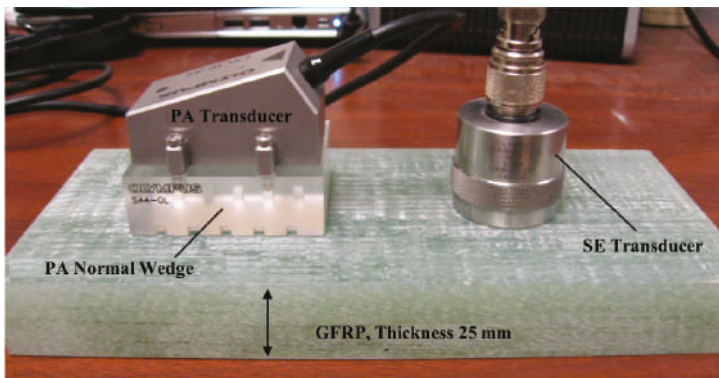


Figure 3. Experimental setup for capability and sensitivity evaluation: PAUT (left) and SEUT (right).

### 3.2. PAUT Guided Wave Method

Guided wave modes were generated on Al and CFRP plates by means of a commercially available phased array probe and wedges. The procedure of plate wave generation and parametric evaluation are described in detail in [8,18]. A 1.5 MHz phased array ultrasonic probe with 16 elements and related 60 degrees longitudinal wave wedge was used for guided wave generation and flaw detection. Figure 4 shows the setup used for inspecting the artificial defects (drilled holes) in CFRP sample. In CFRP sample, guided waves were generated in direction of the fibers.

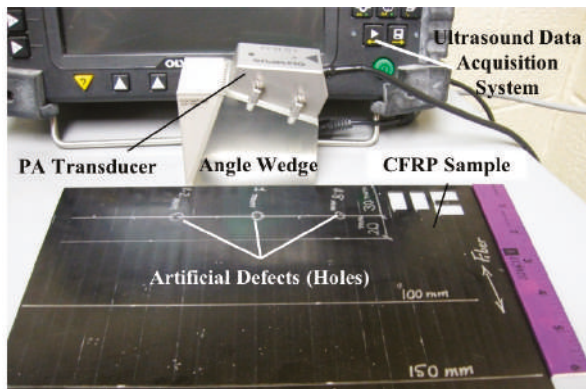


Figure 4. Experimental setup for flaw detection in CFRP sample using PAUT guided wave method.

## 4. Results and Discussions

### 4.1. SEUT Versus PAUT Methods

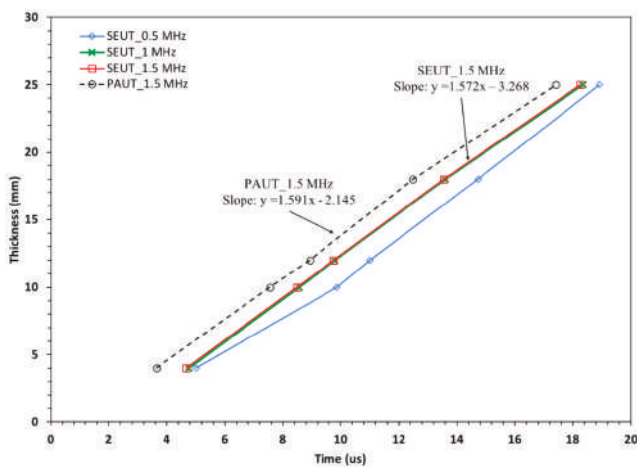
#### 4.1.1. Focusing Depth Comparison

Table 2 shows the signal characteristics in terms of signal-to-noise ratio (SNR) for SEUT and PAUT. Data in Table 2 is plotted in Figure 5 and shows the relationship between the thicknesses of the GFRP plates (i.e., wave traveling distance) and travelling time of ultrasound wave. It can be observed that the velocities in the GFRP plate can be calculated as twice the slope of the graph, which are equal to  $2 \times 1.57 = 3.15 \text{ mm}/\mu\text{s}$  for SEUT and  $2 \times 1.59 = 3.18 \text{ mm}/\mu\text{s}$  for PAUT. Figure 6 shows an example for typical signals for the back wall reflection in SEUT and PAUT methods in the 12-mm-thick composite plate. As can be seen from the results in Table 2 and considering the form of the ultrasound signal

shown in Figure 6, the features of the signals are clearer and better detectable using PAUT with lower gain values. The wave velocity is important information in determining the depth and location of the defects according to the ultrasound wave’s traveling time.

**Table 2.** Signal characteristics of back wall reflection for SEUT method with different frequencies and PAUT method.

| Frequency | Method | Sample | Thickness (mm) | Gain (dB) | Time ( $\mu$ s) | Signal-to-Noise Ratio |
|-----------|--------|--------|----------------|-----------|-----------------|-----------------------|
| 0.5 MHz   | SEUT   | GFRP   | 4              | 42        | 5.01            | 7.95                  |
|           |        |        | 10             | 55.8      | 9.87            | 3.99                  |
|           |        |        | 12             | 60.5      | 11.01           | 3.07                  |
|           |        |        | 18             | 61        | 14.73           | 2.98                  |
|           |        |        | 25             | 64.7      | 18.92           | 2.53                  |
| 1 MHz     | SEUT   | GFRP   | 4              | 18.5      | 4.76            | 5.31                  |
|           |        |        | 10             | 36        | 8.56            | 11.93                 |
|           |        |        | 12             | 39.6      | 9.80            | 11.75                 |
|           |        |        | 18             | 41.2      | 13.60           | 11.10                 |
|           |        |        | 25             | 45.9      | 18.35           | 9.57                  |
| 1.5 MHz   | SEUT   | GFRP   | 4              | 15.5      | 4.67            | 5.14                  |
|           |        |        | 10             | 37        | 8.48            | 11.75                 |
|           |        |        | 12             | 40.8      | 9.76            | 11.10                 |
|           |        |        | 18             | 43        | 13.55           | 9.51                  |
|           |        |        | 25             | 46.7      | 18.25           | 9.43                  |
| 1.5 MHz   | PAUT   | GFRP   | 4              | 13        | 3.64            | 6.10                  |
|           |        |        | 10             | 27        | 7.56            | 5.44                  |
|           |        |        | 12             | 28.5      | 8.93            | 5.81                  |
|           |        |        | 18             | 36        | 12.49           | 3.39                  |
|           |        |        | 25             | 40        | 17.41           | 3.22                  |



**Figure 5.** Back wall reflection experiment showing ultrasonic wave velocity evaluation measured by SEUT and PAUT methods.

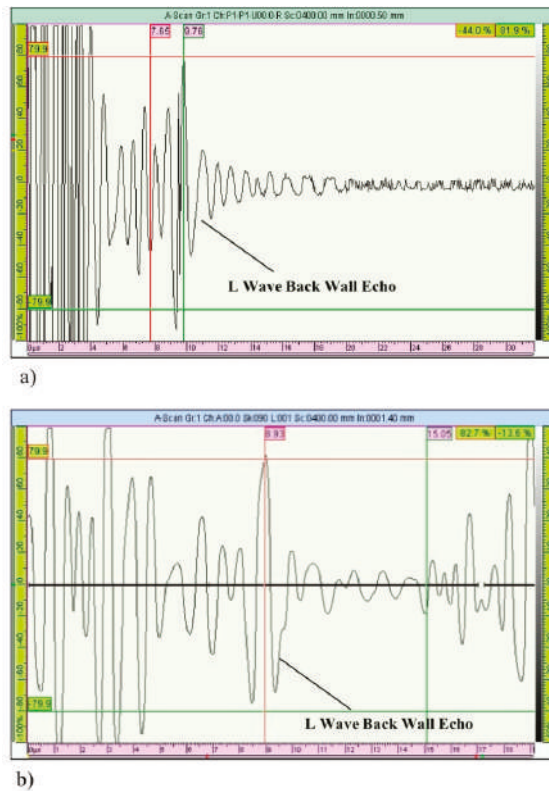


**Figure 6.** Back wall reflection signals for GFRP: (a) SEUT method and (b) PAUT method. (Freq. = 1.5 MHz, Thickness = 12 mm).

All the measured velocities are very close in value; however, the attenuation (i.e., gain values) is improved for PAUT when compared to SEUT at 1.5 MHz. On the other hand, the quantitative values in Table 2 show that SNR is, on average, two times larger for SEUT when comparing the peak of reflected signal to the background noise. However, it should be mentioned that the resolution of the peak and its location is much lower in SEUT which caused inaccuracy for detection purposes. Higher local value of SNR in SEUT can be attributed to the interference of the signals for each element in PAUT. Qualitatively, PAUT has more uniform and detectable signal with less jitter, specifically at larger thicknesses. Figure 7 shows the gain values (for different inspection frequencies) in order to reach detectable signal in different sample thicknesses. The plot shows that the SNR and signal's attenuation were improved in PAUT technique when compared to SEUT such that 7–20% less gain in value was required to have detectable signal in case of 1.5 MHz transducers.

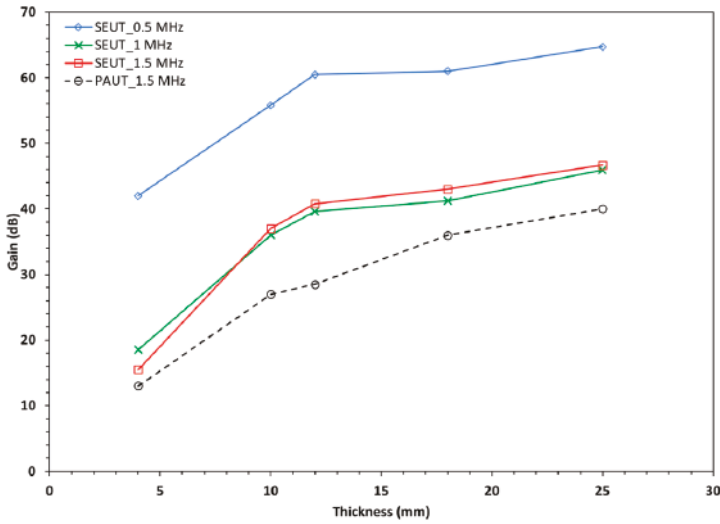


**Figure 7.** Gain (dB) value for back wall reflection detection in different sample thickness for attenuation characteristics evaluation using SEUT and PAUT techniques.

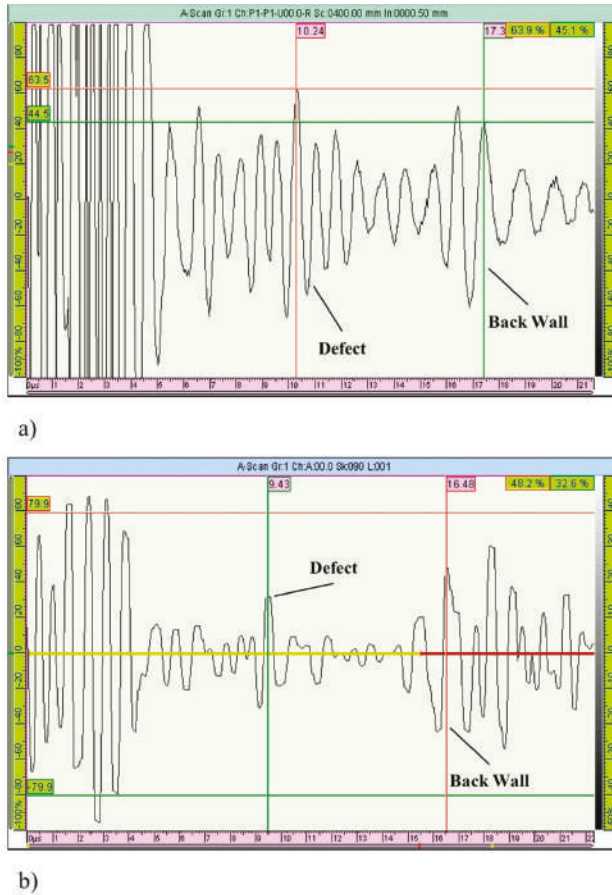
4.1.2. Sensitivity Comparison and Defect Detection

Figure 8 shows the signals associated with the defect (artificially drilled holes) reflections by SEUT and PAUT methods. The depth of the hole can be determined based on the obtained velocity values, as in Equations (1) and (2). Both SEUT and PAUT techniques provided results that are very close to what was obtained by real time x-ray imaging (i.e., 11.175 mm) for validation. It was observed that both SEUT and PAUT techniques can detect a 0.8 mm diameter hole as the minimum size and sensitivity limit; however, PAUT method provides approximately 15% higher SNR for the defect signal. We believe that in PAUT, lower SNR and better signal characteristics, such as higher focusing energy, could assist in detecting smaller-sized defect sizes, and this needs further experimental evaluation.

$$\text{Depth(SEUT)} = \frac{\text{Time} \times \text{Velocity}}{2} = \frac{7.12 \times 3.07}{2} = 10.9 \text{ mm} \tag{1}$$

$$\text{Depth(PAUT)} = \frac{\text{Time} \times \text{Velocity}}{2} = \frac{7.05 \times 3.23}{2} = 11.4 \text{ mm} \tag{2}$$

In Figure 8, PAUT has a clearer and more easily detectable reflection from the defect (reflector), as well as a better detectable back wall reflection. However, when looking at SEUT signal, due to less smoothness in signal from one transducer element, it is more difficult to identify these reflection locations. In addition, as can be seen from the data in Table 2, the gain value is a very important factor. However in some cases the SNR in SEUT looks to be higher, but it was obtained with higher gain value. This happened when a small decrease in the gain value, less than the values in Table 2, did not provide a good detectable signal.



**Figure 8.** Response signal for CFRP: (a) SEUT method and (b) PAUT method. (Freq. = 1.5 MHz, Thickness = 25 mm, Hole Diameter = 0.8 mm, Hole Depth = 12mm).

#### 4.2. PAUT Guided Wave Method

Tables 3 and 4 show the results for the signal response parameters for Al-1 and Al-2 samples. In the dispersion curve of guided wave modes in plates, the smaller values of “*fd*” (i.e., frequency x plate thickness) are more distinctive and, consequently, have a higher probability of detection [31]. In practical application specifically when the thickness of the plate structure is a fixed and known value, only the frequency of inspection can be changed. So, for thicker structures, one should use much lower frequencies, while for thinner structures, the range of possible frequencies will be wider and higher frequencies can be used to increase the resolution. The effect of “*fd*” value in response signals is presented in Tables 3 and 4. We find that, in lower “*fd*” values, the distance from which the signal from the defect is still detectable is longer. The phase velocity for the generated guided wave were calculated based on the theory and properties of the angle wedge. Based on these values, S0, A1, and S1 modes were possible for the Al-1 sample (*fd* = 3.3 MHz.mm), and A0 and S0 modes are possible for Al-2 sample (*fd* = 0.96 MHz.mm). The strongest reflection which also has the closest phase velocity value to the theory were identified as the dominate wave modes. In this case it was A1 for Al-1 sample, S0 for Al-2 sample, and S0 for CFRP sample. In Tables 3 and 4, signal parameters from the reflection of the edge of the plate close to the hole, and from the hole are presented. These signal parameters

include the arrival time and the amplitude of the signal at the edge of the plate and the defect. Figure 9 shows the change of the signal’s amplitude over the distance of the PAUT transducer from the edge for Al-1 and Al-2. For Al-1 it was noticed that the hole’s signal has larger amplitude at a longer distance compared to Al-2. This is attributed to the interference of the stationary wedge reflection signal and the signal from the hole. Figure 10 shows typical signals for the experiments in Tables 3 and 4 for Al-1 and Al-2.

Table 3. Signal parameters for flaw detection in Al-1 sample.

| Experimental Setup Parameters for PAUT Guided Wave Inspection of Al-1 Sample   |                    |           |   |                   |                           |                 |               |      |
|--|--------------------|-----------|---|-------------------|---------------------------|-----------------|---------------|------|
| Frequency (MHz)  | Thickness (mm)     | Gain (dB) | Element Qty. <sup>1</sup>                 | $fd^2$            | Element Step <sup>3</sup> |                 |               |      |
| 1.5  | 2.2                | 30        | 4   | 3.3               | 1                         |                 |               |      |
| <sup>1</sup> Number of active elements at each sequence in phased array ultrasound transducer<br><sup>2</sup> frequency × plate thickness (MHz.mm)<br><sup>3</sup> Incremental steps in terms of number of elements at each sequence |                    |           |   |                   |                           |                 |               |      |
| Defect Detection Signal Characteristics  |                    |           |   |                   |                           |                 |               |      |
| Experimental Trials #  | Hole Diameter (mm) | Signal    | Distance of Transducer from The Edge (mm) | Arrival Time (us) |                           | $D_{Time}$ (us) | Amplitude (%) |      |
|  |                    |           |   | Edge              | Hole                      |                 | Edge          | Hole |
| 1  | 1                  | Edge/Hole | 50  | 58.07             | 47.61                     | 10.5            | 53.9          | 46.6 |
| 2  |                    | Edge/Hole | 100                                       | 87.99             | 70.27                     | 17.7            | 33.1          | 24.3 |
| 3  |                    | Edge/Hole | 150                                       | 109.77            | 92.34                     | 17.4            | 10.3          | 21.1 |

Table 4. Signal parameters for flaw detection for Al-2.

| Experimental Setup Parameters for PAUT Guided Wave Inspection of Al-2 Sample   |                   |           |   |                   |                           |                 |               |      |
|--|-------------------|-----------|---|-------------------|---------------------------|-----------------|---------------|------|
| Frequency (MHz)  | Thickness (mm)    | Gain (dB) | Element Qty. <sup>1</sup>                 | $fd^2$            | Element Step <sup>3</sup> |                 |               |      |
| 1.5  | 0.635             | 30        | 4   | 0.96              | 1                         |                 |               |      |
| <sup>1</sup> Number of active elements at each sequence in phased array ultrasound transducer<br><sup>2</sup> frequency × plate thickness (MHz.mm)<br><sup>3</sup> Incremental steps in terms of number of elements at each sequence |                   |           |   |                   |                           |                 |               |      |
| Defect Detection Signal Characteristics  |                   |           |   |                   |                           |                 |               |      |
| Experimental Trial #   | Hole Diameter(mm) | Signal    | Distance of Transducer from The Edge (mm) | Arrival Time (us) |                           | $D_{Time}$ (us) | Amplitude (%) |      |
|  |                   |           |   | Edge              | Hole                      |                 | Edge          | Hole |
| 1  | 1                 | Edge/Hole | 50  | 39.19             | 28.15                     | 11.0            | 100           | 15.5 |
| 2  |                   | Edge/Hole | 100                                       | 57.78             | 46.45                     | 11.3            | 100           | 11.5 |
| 3  |                   | Edge/Hole | 175                                       | 85.08             | 74.34                     | 10.7            | 82.7          | 7.8  |
| 4  |                   | Edge/Hole | 200                                       | 94.09             | 83.05                     | 11.0            | 77.7          | 4.5  |

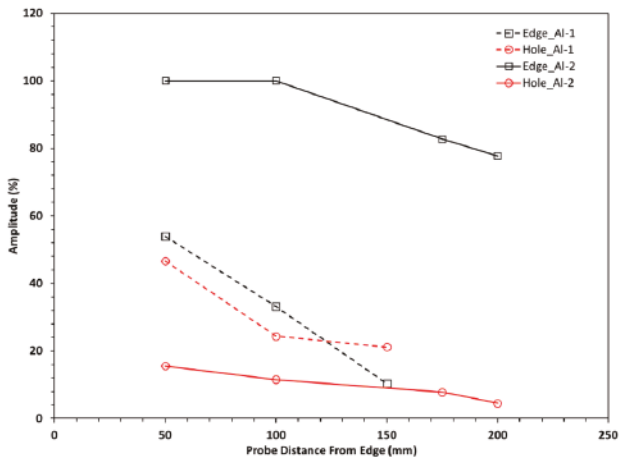


Figure 9. Change of signal amplitude over distance for Al-1 and Al-2 samples.



a)



b)

Figure 10. Typical PAUT guided wave signal of flaw detection for (a) Al-1 sample and (b) Al-2 sample.

Table 5 shows the results of PAUT guided wave signal parameters for the CFRP sample. In Table 5, the arrival time of the reflection signal from the plate edge and the defect (hole) are presented (See Figure 2 for reference). The difference between the arrival times from the plate edge and from the defect (hole) was calculated. Considering the wave velocity, which was experimentally determined in a previous work [8], the distance between the plate edge and defect (hole) was determined experimentally. Comparing the distance between the plate and the defect (hole) which was determined experimentally with the actual location (as designed = 30 mm) shows that the location of the defect (hole) can be determined using the proposed technique within an acceptable range. When the size of the defect (hole) is larger, there is a better probability of detection, and the accuracy in determining the location of the defect (hole) is higher. In addition, when there is less interference between wave modes, such as in the case of larger distances, there is higher accuracy of detection. Better accuracy at larger distances occurs because, when the travelling distance for the guided waves is short, these wave modes are not stabilized and have many overlaps and low signal-to-noise ratio which cause higher inaccuracy. Figure 11 shows a typical signal for the experimental result listed in Table 5 for CFRP. Figure 12 shows the change in signal amplitude at different defect (hole) sizes for the experiments in Table 5 for CFRP. The amplitude of the signal from the plate edge is inversely proportional to the hole diameter. However, the amplitude of the signal from the hole is directly proportional to the hole diameter. As the hole diameter increases (i.e., larger defect), a larger part of the ultrasonic energy is reflected by the defect (hole), and consequently a smaller part will hit the edge.

Table 5. Signal parameters for flaw detection for CFRP.

| Experimental Setup Parameters for PAUT Guided Wave Inspection of CFRP  |                   |           |  |                               |                           |                 |                 |
|--|-------------------|-----------|--|-------------------------------|---------------------------|-----------------|-----------------|
| Frequency (MHz)  | Thickness (mm)    | Gain (dB) | Element Qty. <sup>1</sup>                | $fd^2$                        | Element Step <sup>3</sup> |                 |                 |
| 1.5  | 1                 | 35        | 4  | 1.5                           | 1                         |                 |                 |
| <sup>1</sup> Number of active elements at each sequence in phased array ultrasound transducer<br><sup>2</sup> frequency × plate thickness (MHz.mm)<br><sup>3</sup> Incremental steps in terms of number of elements at each sequence |                   |           |  |                               |                           |                 |                 |
| Defect Detection Signal Characteristics  |                   |           |  |                               |                           |                 |                 |
| Experimental Trial #   | Hole Diameter(mm) | Signal    | Distance of Transducer from The Edge(mm) | Arrival Time (us) (Edge/Hole) |                           | $D_{Time}$ (us) | $D_{dist}$ (mm) |
|  |                   |           |  | Edge                          | Hole                      |                 |                 |
| 1  | 0.8               | Edge/Hole | 50                                       | 25.64                         | 13.81                     | 11.83           | 48.9            |
| 2  |                   | Edge/Hole | 100                                      | 35.6                          | 24.54                     | 11.06           | 45.7            |
| 3  |                   | Edge/Hole | 150                                      | 46.11                         | 37.08                     | 9.03            | 37.3            |
| 1  | 1                 | Edge/Hole | 50                                       | 26.76                         | 14.07                     | 12.69           | 52.5            |
| 2  |                   | Edge/Hole | 100                                      | 35.62                         | 26.11                     | 9.51            | 39.3            |
| 3  |                   | Edge/Hole | 150                                      | 45.97                         | 37.28                     | 8.69            | 35.9            |
| 1  | 1.2               | Edge/Hole | 50                                       | 24.52                         | 14.11                     | 10.41           | 43.0            |
| 2  |                   | Edge/Hole | 100                                      | 36.24                         | 26.89                     | 9.35            | 38.6            |
| 3  |                   | Edge/Hole | 150                                      | 46.25                         | 37.36                     | 8.89            | 36.7            |

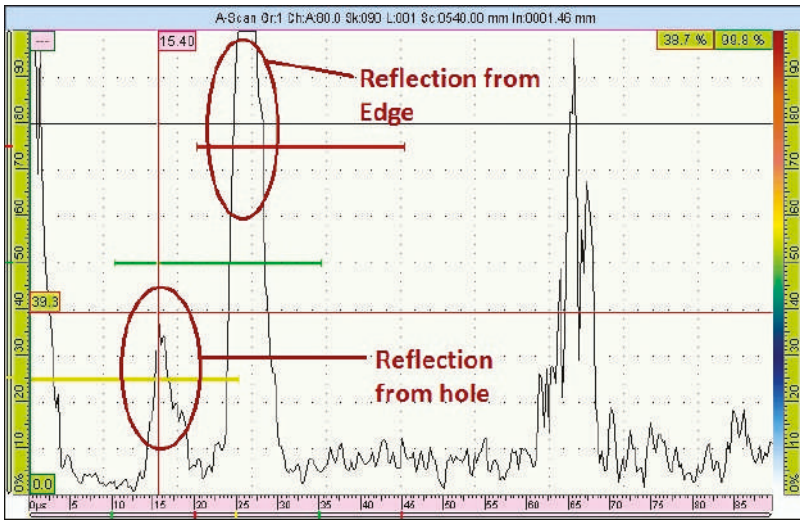


Figure 11. Typical PAUT guided wave signal of flaw detection for CFRP sample.

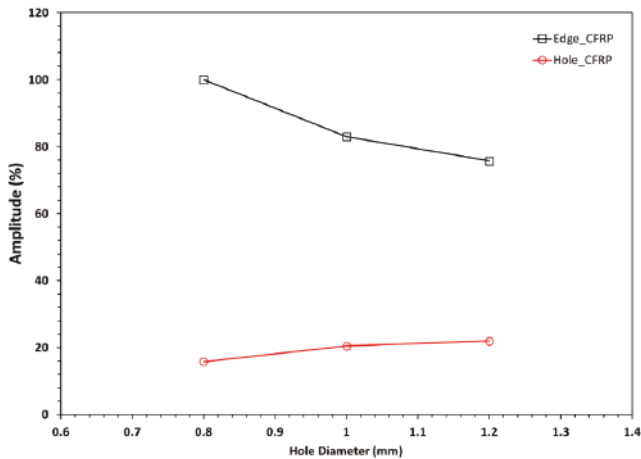


Figure 12. Change of signal amplitude over distance for CFRP samples.

### 5. Conclusions

Conventional (single-element) ultrasonic testing and phased array ultrasonic testing (PAUT) methods are evaluated for inspection of composite materials. The capability comparison tests for waves traveling through the composite materials indicate that thickness of up to 25 mm could be tested in both SEUT and PAUT methods; however, the stability of the signal parameters is higher in PAUT and detectable signal can be observed at lower gain values. The calculated velocity from the capability experimental part was 3.1 mm/μs, which is close to the estimated and expected velocities in composite plates and was used to identify the flaw’s location. From the sensitivity comparison experimental results, it can be seen that a 0.8 mm diameter hole can be detected as the minimum size by both SEUT and PAUT, but PAUT generally has a better signal regarding SNR. However, PAUT does not increase the sensitivity by a big factor, but because of lower noise and jitter and better signal characteristics it may be possible to find smaller defect sizes such as 0.7 or 0.6 mm with PAUT as well.

Guided waves can also be generated using phased array ultrasonic probes and wedges with lower frequencies. Experimental results show that the different size of flaw (0.8, 1, and 1.2 mm diameter holes) can be detected by means of generated guided waves with the PAUT method. While the determination of the exact location of the flaw is affected by the dispersion characteristics of the guided waves, PAUT is a promising technique for detecting the size and location of defects in CFRP and GFRP composite materials.

**Author Contributions:** Conceptualization, H.T. and A.A.H.; Methodology, H.T.; Formal Analysis, H.T.; Investigation, H.T. and A.A.H.; Data Curation, H.T.; Writing—Original Draft Preparation, H.T.; Writing—Review and Editing, A.A.H.; Visualization, H.T. and A.A.H.; Supervision, A.A.H.

**Funding:** Research sponsored by the U.S. Department of Energy, Office of Energy Efficiency and Renewable Energy, Advanced Manufacturing Office, under contract DE-AC05-00OR22725 with UT-Battelle, LLC.

**Acknowledgments:** A debt of gratitude is owed to OLYMPUS NDT technical support and sales team for all their contributions to provide required equipment, support, and information.

**Conflicts of Interest:** The authors declare no conflict of interests. Notice of Copyright: This manuscript has been authored by UT-Battelle, LLC under Contract No. DE-AC05-00OR22725 with the U.S. Department of Energy. The United States Government retains and the publisher, by accepting the article for publication, acknowledges that the United States Government retains a non-exclusive, paid-up, irrevocable, world-wide license to publish or reproduce the published form of this manuscript, or allow others to do so, for United States Government purposes. The Department of Energy will provide public access to these results of federally sponsored research in accordance with the DOE Public Access Plan. (<http://energy.gov/downloads/doe-public-access-plan>).

## References

1. Poudel, A.; Shrestha, S.S.; Sandhu, J.S.; Chu, T.P.; Pergantis, C.G. Comparison and Analysis of Acoustography with Other NDE Techniques for Foreign Object Inclusion Detection in Graphite Epoxy Composites. *Compos. Part B Eng.* **2015**, *78*, 86–94. [[CrossRef](#)]
2. Raišutis, R.; Jasiuniene, E.; Sliteris, R.; Vladišauskas, A. The review of non-destructive testing techniques suitable for inspection of the wind turbine blades. *Ultrasound* **2008**, *63*, 26–30.
3. Amenabar, I.; Mendikute, A.; López-Arraiza, A.; Lizaranzu, M.; Aurrekoetxea, J. Comparison and analysis of non-destructive testing techniques suitable for delamination inspection in wind turbine blades. *Compos. Part B Eng.* **2011**, *42*, 1298–1305. [[CrossRef](#)]
4. Adem, E.; Reddy, G.M.; Koricho, E.G.; Science, A.; Science, A.; Science, A.; Vehicle, C. Experimental Analysis of E-Glass/Epoxy & E-Glass/polyester Composites for Auto Body Panel. *Am. Int. J. Res. Sci. Technol. Eng. Math.* **2015**, *10*, 377–383.
5. Ensminger, D.; Bond, L.J. *Ultrasonics: Fundamentals, Technologies, and Applications*, 3rd ed.; CRC Press: Boca Raton, FL, USA, 2011.
6. Hübschen, G.; Altpeter, I.; Tschuncky, R.; Herrmann, H.-G. (Eds.) *Materials Characterization Using Nondestructive Evaluation (NDE) Methods*; Elsevier: Amsterdam, The Netherlands, 2016.
7. Taheri, H. Classification of Nondestructive Inspection Techniques with Principal Component Analysis (PCA) for Aerospace Application. In Proceedings of the ASNT 26th Research Symposium, Jacksonville, FL, USA, 13–16 March 2017; pp. 219–227.
8. Taheri, H. Utilization of Non-Destructive Testing (NDT) Methods for Composite Material Inspection (Phased array Ultrasonic). Master's Thesis, South Dakota State University, Brookings, South Dakota, 2014.
9. Wertz, J.; Homa, L.; Welter, J.; Sparkman, D.; Aldrin, J.C. Case Study of Model-Based Inversion of the Angle Beam Ultrasonic Response from Composite Impact Damage. *J. Nondestr. Eval. Diagn. Progn. Eng. Syst.* **2018**, *1*, 41001–41010. [[CrossRef](#)]
10. Taheri, H.; Delfanian, F.; Du, J. Ultrasonic phased array techniques for composite material evaluation. *J. Acoust. Soc. Am.* **2013**, *134*, 4013. [[CrossRef](#)]
11. Taheri, H.; Ladd, K.M.; Delfanian, F.; Du, J. Phased array ultrasonic technique parametric evaluation for composite materials. In *ASME International Mechanical Engineering Congress and Exposition, Proceedings (IMECE)*; American Society of Mechanical Engineers: New York, NY, USA, 2014; Volume 13, p. V013T16A028.

12. Caminero, M.A.; García-Moreno, I.; Rodríguez, G.P.; Chacón, J.M. Internal damage evaluation of composite structures using phased array ultrasonic technique: Impact damage assessment in CFRP and 3D printed reinforced composites. *Compos. Part B Eng.* **2019**, *165*, 131–142. [[CrossRef](#)]
13. Hassen, A.A.; Taheri, H.; Vaidya, U.K. Non-destructive investigation of thermoplastic reinforced composites. *Compos. Part B Eng.* **2016**, *97*, 244–254. [[CrossRef](#)]
14. Aldrin, J.C.; Wertz, J.N.; Welter, J.T.; Wallentine, S.; Lindgren, E.A.; Kramb, V.; Zainey, D. Fundamentals of angled-beam ultrasonic NDE for potential characterization of hidden regions of impact damage in composites. *AIP Conf. Proc.* **2018**, *1949*, 120005.
15. Toyama, N.; Ye, J.; Kokuyama, W.; Yashiro, S. Non-Contact Ultrasonic Inspection of Impact Damage in Composite Laminates by Visualization of Lamb wave Propagation. *Appl. Sci.* **2018**, *9*, 46. [[CrossRef](#)]
16. Castellano, A.; Fraddosio, A.; Piccioni, M.D. Quantitative analysis of QSI and LVI damage in GFRP unidirectional composite laminates by a new ultrasonic approach. *Compos. Part B Eng.* **2018**, *151*, 106–117. [[CrossRef](#)]
17. Taheri, H.; Delfanian, F.; Du, J. Acoustic Emission and Ultrasound Phased Array Technique for Composite Material Evaluation. In *ASME International Mechanical Engineering Congress and Exposition, Proceedings (IMECE): Advances in Aerodynamics*; American Society of Mechanical Engineers: New York, NY, USA, 2013; Volume 1, p. V001T01A015.
18. Bai, Z.; Chen, S.; Xiao, Q.; Jia, L.; Zhao, Y.; Zeng, Z. Compressive sensing of phased array ultrasonic signal in defect detection: Simulation study and experimental verification. *Struct. Health Monit.* **2017**, *17*, 434–449. [[CrossRef](#)]
19. Taheri, H.; Du, J.; Delfanian, F. Experimental Observation of Phased Array Guided Wave Application in Composite Materials. *Mater. Eval.* **2017**, *75*, 1308–1316.
20. Bolotina, I.; Borikov, V.; Ivanova, V.; Mertins, K.; Uchaikin, S. Application of phased antenna arrays for pipeline leak detection. *J. Pet. Sci. Eng.* **2018**, *161*, 497–505. [[CrossRef](#)]
21. Taheri, H.; Koester, L.; Bigelow, T.; Bond, L.J.; Braconnier, D.; Carcreff, E.; Dao, A.; Caulder, L.; Hassen, A.A. Fast Ultrasonic Imaging with Total Focusing Method (TFM) for Inspection of Additively Manufactured Polymer Composite Component. In *Proceedings of the 27th ASNT Research Symposium, São Paulo, Brazil, 27–29 August 2018*; pp. 212–220.
22. Drinkwater, B.W.; Wilcox, P.D. Ultrasonic arrays for non-destructive evaluation: A review. *NDT&E Int.* **2006**, *39*, 525–541.
23. Fromme, P.; Wilcox, P.D.; Lowe, M.J.S.; Cawley, P. On the development and testing of a guided ultrasonic wave array for structural integrity monitoring. *IEEE Trans. Ultrason. Ferroelectr. Freq. Control* **2006**, *53*, 777–785. [[CrossRef](#)] [[PubMed](#)]
24. Leleux, A.; Micheau, P.; Castaings, M. Long Range Detection of Defects in Composite Plates Using Lamb Waves Generated and Detected by Ultrasonic Phased Array Probes. *J. Nondestr. Eval.* **2013**, *32*, 200–214. [[CrossRef](#)]
25. Philtrou, J.H.; Rose, J.L. Guided wave phased array sensor tuning for improved defect detection and characterization. In *Proc. SPIE 9063, Nondestructive Characterization for Composite Materials, Aerospace Engineering, Civil Infrastructure, and Homeland Security*; International Society for Optics and Photonics: San Diego, CA, USA, 2014; p. 906306.
26. Wang, W.; Zhang, H.; Lynch, J.P.; Cesnik, C.E.S.; Li, H. Experimental and numerical validation of guided wave phased arrays integrated within standard data acquisition systems for structural health monitoring. *Struct. Control Health Monit.* **2018**, *25*, e2171. [[CrossRef](#)]
27. Rose, J.L. Ultrasonic guided waves in structural health monitoring. *Key Eng. Mater.* **2004**, *270*, 14–21. [[CrossRef](#)]
28. Rose, J.L. *Ultrasonic Guided Waves in Solid Media*; Ultrasonic Guided Waves in Solid Media; Cambridge University Press: Cambridge, UK, 2014; Volume 9781107048959, pp. 1–512.
29. Wilcox, P.; Lowe, M.; Cawley, P. Effect of dispersion on long-range inspection using ultrasonic guided waves. *NDT E Int.* **2001**, *34*, 1–9. [[CrossRef](#)]
30. Chimenti, D.E. Guided waves in plates and their use in materials characterization. *Appl. Mech. Rev.* **1997**, *50*, 247–284. [[CrossRef](#)]

31. Rose, J.L. Successes and Challenges in Ultrasonic Guided Waves for NDT and SHM. In Proceedings of the National Seminar & Exhibition on Non-Destructive Evaluation, Pune, India, 4–6 December 2009.



© 2019 by the authors. Licensee MDPI, Basel, Switzerland. This article is an open access article distributed under the terms and conditions of the Creative Commons Attribution (CC BY) license (<http://creativecommons.org/licenses/by/4.0/>).

Article

# Experimental Study of Defect Localization in a Cross-Ply Fiber Reinforced Composite with Diffuse Ultrasonic Waves

Qi Zhu <sup>1,\*</sup>, Yuxuan Ding <sup>1</sup>, Dawei Tu <sup>1</sup>, Haiyan Zhang <sup>2</sup> and Yue Peng <sup>3,\*</sup>

<sup>1</sup> School of Mechatronic & Automation Engineering, Shanghai University, Shanghai 200444, China; dyx2201@163.com (Y.D.); tdw@shu.edu.cn (D.T.)

<sup>2</sup> School of Communication and Information Engineering, Shanghai University, Shanghai 200444, China; hyzh@shu.edu.cn

<sup>3</sup> Logistics Engineering College, Shanghai Maritime University, Shanghai 201305, China

\* Correspondence: Q\_ZHU@shu.edu.cn (Q.Z.); yuepeng@shmtu.edu.cn (Y.P.); Tel.: +86-13166013707 (Q.Z.)

Received: 8 May 2019; Accepted: 3 June 2019; Published: 6 June 2019

**Abstract:** Diffuse wave inspection benefits from multiple scattering and is suitable for the nondestructive testing of complex structures with high sensitivity. This paper aims to localize the defect in a cross-ply carbon fiber reinforced polymer composite with the diffuse wave field experimentally based on the Locadiff technique. Firstly, the wave diffusivity and dissipation parameters are determined from the diffuse waveforms. Great dissipation is found for this composite plate due to its strong viscoelasticity, which makes the amplitude attenuate fast in a short propagation distance. The signal-to-noise ratios degrade significantly at off-axis directions so that only measurements along the X and Y axes are chosen. Secondly, the decorrelation coefficients are determined using the stretching technique. The decorrelation coefficients decrease initially due to the interaction between the wave fields and the defect and subsequently increase due to the low signal-to-noise ratio at the later time. Based on these data, a sensitivity time domain is chosen to center at  $t = 50 \mu\text{s}$ . Together with the defect sensitivity kernel calculated under constant diffusion property assumption, the defect is localized at [270 mm, 265 mm] compared to [300 mm, 280 mm] in the final reference state. This method is promising for early damage detection in fiber reinforced composite structures.

**Keywords:** diffuse ultrasonic waves; cross-ply fiber reinforced composite; defect localization

## 1. Introduction

Fiber reinforced polymer composites are becoming increasingly important in modern industries due to their high specific strength-weight ratio, anti-corrosion properties, and recyclability. They are manufactured using different processes such as resin transfer molding, extrusion, and automated tape placement, according to different property requirements. Recently, additive manufacturing, combined with various reinforcement control methods (e.g., standing-wave field [1], magnetic field [2], rotational deposition [3]), has come to be considered a cost-efficient method for composite design and manufacturing. During these processes, defects such as voids, cracks, and delaminations may be introduced into the part and lead to structure failure in service.

Defect localization and characterization are critical in modern lightweight structures made of fiber reinforced composites. The early detection of these defects is beneficial to the structural integrity and maintenance. Different methods have been exploited in recent years, including pulse-thermography [4], ultrasonic [5], X ray, acoustic emission [6,7], and electric resistance variation [8,9]. Among all these methods, ultrasonic testing is considered to be promising for in-situ or online inspection. Localization sensitivity can be improved through a higher ultrasonic frequency, but with regards heterogeneous

materials such as concretes, biology tissues, and fiber reinforced composites, wave propagation becomes more complicated with increasing frequency. A full understanding of such process and proper signal processing methods is required to overcome or even benefit from scattering and attenuation phenomena.

The complex internal fiber distribution results in multiple scattering in the fiber reinforced composite. In such mediums, the whole waveform can be separated into the direct (ballistic, the first arrival) wave part and the diffuse wave part [10]. The direct wave is often strongly attenuated and only exists for a short distance that corresponds to the transport mean free path [11]. Subsequently, the energy of the direct waves rapidly converts into late-arriving diffuse waves [12]. The conventional ultrasonic inspection methods tend to lower the frequency to prevent the difficulties brought by attenuation and scattering. They often rely on the information from the direct wave part including the C scan method [13] and the Lamb wave inspection method [5]. The former has been widely accepted in aerospace industry to check defect existence in composite structures with considerable capital cost, and the latter is suitable for thin plate structures and can improve inspection efficiency. Nevertheless, careful interpretation of different propagation modes and boundary reflections/refractions are required [14]. By contrast, the diffuse wave is repeatable and independent of the direct wave path [15], and it can also be applied to structure inspection. Being treated as ambient noise [16] for a long time, the diffuse wave is found to contain valuable information, especially in seismology and civil engineering. Weaver and Lobkis [17] showed that the cross-correlation of two diffuse wave fields from the same excitation is equal to the direct response of one transducer to an impulse applied to the other. More recently, there has been a growing interest in using Green's function recovery technique to study the temperature effect on subsurface velocity variation in the lunar environment [18], to improve the near-surface ultrasonic array imaging resolution [19], etc. By comparing diffuse waves before and after external perturbations, time-lapse monitoring such as stress change [20], temperature variation [21], and progressive damage [22] can be achieved locally from only one fixed transmitter-receiver pair. Meanwhile, cross-correlation techniques with different stability and computational costs [16] have been developed under various names (e.g., cross-spectral moving-window technique (CSMWT), doublet method, stretching method, coda wave interferometry (CWI)) in different research communities. In 2002, Snieder et al. [23] showed that, together with the sensitivity kernel, the CWI technique can be expanded to have a full-field velocity perturbation. Similarly, Rossetto et al. [24] introduced an innovative technique called Locadiff for weak change inspection including emerging defects. Prior knowledge of the materials or exact wave propagation distance is not necessary with this method, which could be important for anisotropic structures [25]. Locadiff has been applied successfully for crack localization in pre-cracked concrete specimens under four point bending [12] with a spatial resolution of a few centimeters. The correlation/decorrelation coefficients are influenced by crack- and deformation-induced geometry changes. On-site detection of three dimensional multiple pre-existing cracks is also realizable for an aeronautical wind tunnel [26]. Combing the Locadiff and CWI techniques [23] together, both the microstructure and velocity variation fields can be obtained to better understand the mechanical behavior of natural rock samples [27].

Because of its great potential for structural health monitoring and nondestructive evaluation in complex structures, diffuse wave inspection has been investigated for fiber reinforced composites as well. Zhu et al. [28] have used coda waves to determine the internal stress in a polymer composite. Livings et al. [29] have explored the sensitivity of diffuse wave correlation coefficients, amplitude spectrum, and phase spectrum under different fatigue cycles for unidirectional carbon fiber reinforced polymer composites (I90/45/-45/90<sub>6</sub>)<sub>s</sub>). Waveform variation is not only caused by the fatigue cycle number, but also by the gain change, couplant type, excitation source type, frequency, etc. Although diffuse wave analysis can detect fatigue induced micro-cracks theoretically, precautions should be taken for all these experimental factors. Patra et al. [30] have applied a modified stretching technique to evaluate the progressive damage state of woven carbon fiber composites online under high-cycle-low-load fatigue loading. The precursor damage index (PDI), which is defined as the cumulative sum of the stretch parameters, can indicate the local formation of micro-scale defects. The

sudden slope change of the PDI represents the stress state change from concentration to relaxation during defect generation. Recently, Pascal et al. [31] applied coda wave interferometry to monitor micro crack propagation in a polypropylene sulfide based carbon fiber composite with a layering sequence of  $[0^\circ/90^\circ, -45^\circ/45^\circ, 0^\circ/90^\circ, -45^\circ/45^\circ]_s$  during a four point bending test. The relative velocity evolution can be derived from waveform correlations, which indicates the damage state.

To date, few attempts have been made to investigate defect localization in fiber reinforced composites with diffuse wave inspection. The present work aims to understand this procedure experimentally for a single defect localization in a cross-ply fiber reinforced structure. We will first review the Locadiff technique based on diffuse wave field. Then, the experiment results will be presented and analyzed.

## 2. Theoretical background

During diffuse wave propagation in a non-homogeneous material, the energy  $I(S, R, t)$  of a diffuse wave in a defined frequency for a source  $I_0$  can be described by the diffusion equation [32]:

$$\frac{\partial I(S, R, t)}{\partial t} - D\Delta I(S, R, t) + kI(S, R, t) = I_0, \tag{1}$$

where  $D$  is the wave diffusivity,  $k$  is the dissipation parameter,  $t$  is the time,  $I(S, R, t)$  is the energy propagated from a source  $S$  to a receiver  $R$ . Equation (1) describes the spatio-temporal variation of the diffuse wave field. A more accurate description can be obtained from the radiative transfer equation [33].

Supposing the waveforms  $\varphi_A(S, R, t)$  and  $\varphi_B(S, R, t)$  can be obtained before and after a defect appearance during experiments, they are related with the energy through Equation (2) [24,34]:

$$\langle \varphi_A(S, R, t)\varphi_B(S, R, t) \rangle = I(S, R, t) - \frac{c\sigma}{2} \int_0^t I(S, x, u)I(x, R, t-u)du, \tag{2}$$

in which  $c$  is the wave velocity,  $\sigma$  is the scattering cross-section, and  $x$  is the defect location. It can be normalized into Equation (3):

$$\frac{\langle \varphi_A(S, R, t)\varphi_B(S, R, t) \rangle}{\sqrt{\langle \varphi_A^2(S, R, t) \rangle \langle \varphi_B^2(S, R, t) \rangle}} = CC(S, R, x, t) = 1 - DC(S, R, x, t) = 1 - \frac{c\sigma}{2} \frac{\int_0^t I(S, x, u)I(x, R, t-u)du}{I(S, R, t)}, \tag{3}$$

in which  $CC(S, R, x, t)$  is the correlation coefficient and  $DC(S, R, x, t)$  is the decorrelation coefficient. They all depend on the time and the positions of the source, the receiver, and the defect location.  $DC(S, R, x, t) = 0$  when no defect presents ( $\sigma = 0$ ) and  $DC(S, R, x, t) = 1$  when the two waveforms are absolutely different (e.g., with large cracks). The decorrelation coefficient is related to the defect sensitivity kernel function  $K(S, R, x, t)$  using Equations (4) and (5) [35]:

$$DC(S, R, x, t) = \frac{c\sigma}{2} K(S, R, x, t), \tag{4}$$

in which

$$K(S, R, x, t) = \frac{\int_0^t I(S, x, u)I(x, R, t-u)du}{I(S, R, t)} \tag{5}$$

Equation (5) does not have an analytical form in general and should be calculated numerically [33].

Once  $DC(S, R, x, t)$  and  $K(S, R, x, t)$  are obtained, the defect location can be predicted from different inversion algorithms, e.g., the linear least square inversion method [35] and the Monte Carlo Markov chain method [36]. Here a classical grid search method is used to find the most likely defect position using the cost function below:

$$e(x) = \sum_{S,R} \frac{DC(S, R, x, t)^2}{\epsilon^2} - \frac{(\sum_{S,R} DC(S, R, x, t)K(S, R, x, t))^2}{\epsilon^2 \sum_{S,R} K(S, R, x, t)^2}, \tag{6}$$

The probability density of the defect appearance at  $x$  is defined in Equation (7):

$$p(x) = \frac{1}{C} \exp\left(-\frac{e(x)}{2\epsilon^2}\right), \tag{7}$$

where  $\varepsilon$  is a fluctuation parameter for the measured decorrelations and  $C$  is a normalization constant.

### 3. Experiments

A  $[0^\circ/90^\circ]_{12}$  carbon fiber reinforced epoxy composite laminate made using a hot press process with unidirectional prepregs (Toray) is studied here; the experimental set-up is shown in Figure 1a. The plate is 510 mm  $\times$  510 mm  $\times$  3 mm in dimension. Since the thickness is small compared to the length and width dimensions, we will treat the plate as a two-dimensional model based on Equation (1). Due to the high attenuation of ultrasonic waves in the composite plate (4.3 dB/cm at 5 MHz [37]), the pitch-catch configuration is chosen and the gain is 17 dB. The high-pass filter is 1 MHz, while the low-pass filter is 10 MHz. The longitudinal transducer (A551S 5 MHz, Olympus, Inc., Tokyo, Japan) is excited using a pulsed source from a signal generator (Shantou Goworld Display Co., Ltd., Shantou, China). The waveform is recorded using a same type longitudinal transducer through an oscilloscope (TBS1202B, Tektronix, Inc., Beaverton, OR, USA) connected to a personal computer. The ultrasonic sensors are fixed to the plate by 3D printed fixtures with springs inside to apply constant forces on the sensors. A high viscosity couplant can provide good wave transmission and a traditional honey is applied. The defect is simulated using a circular piezoelectric medium attached to the composite plate surface [38]. Signals are amplified and averaged over 10 acquisitions for each source-receiver pair to minimize noises such as the rapid changes of capacitances between conductors due to flexing, twisting, or transient impacts on cables. Furthermore, since an important signal variation has been observed with a minor sensor movement, the defect is attached and detached repeatedly while keeping each source (S)-receiver ( $R_n$ ,  $n = 1-4$ ) pair fixed during signal recording (Figure 1b).

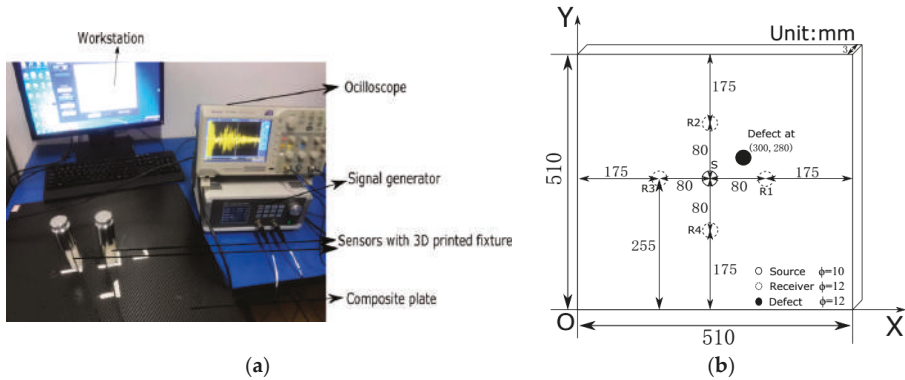


Figure 1. (a) Experimental set-up and (b) measurement scheme.

A typical waveform from S- $R_1$  is presented in Figure 2. No first arrival time variation can be observed using an amplitude threshold picker [39]. The wave diffusivity and the dissipation parameter can be decided from the waveform envelope through the Hilbert transform based on Equation (1) that  $D = 100 \text{ m}^2/\text{s}$  and  $k = 3 \times 10^5 / \text{s}$ . The dissipation parameter  $k$  is an indication of viscoelasticity, which describes the exponential decay at late times. It is much larger than that of concrete with 5500/s [26]. These values fit well with waveforms in  $0^\circ$  and  $90^\circ$  directions. In contrast, the waveforms from off-axis directions ( $30^\circ$  and  $60^\circ$ ) have poor signal-to-noise ratios, as shown in Figure 3. It can be difficult for the diffusion property to be decided in those directions, which makes measurement with an arbitrary sensor location unreliable. Only the measurements along the X and Y axes are chosen here, and a constant diffusion property is assumed during the defect sensitivity kernel calculation under the measurement scheme in Figure 1b. The first arrival time is about 10  $\mu\text{s}$  and gives a group velocity of 8000 m/s along the X and Y axes. In fact, the directivity of the group velocity [40] does not interfere with the defect localization procedure according to Equation (6). The transport mean free

path  $L^* = 2D/c \approx 0.025$  m is less than the transmitter-receiver pair distance 0.08 m, which ensures the ultrasonic wave is multiple scattered. The wave diffusivity is a characteristic of the microstructure which relates to the arrival time of the maximum energy density and decreases with frequency. A large variation of  $D$  has been found for concrete, from  $10 \text{ m}^2/\text{s}$  [32] to  $70 \text{ m}^2/\text{s}$  [26], because of its internal structure variation and frequency sensitivity to the diffuse wave. This can be expected as well for fiber reinforced composites. Quiviger et al. found that  $D$  varies from 17 to  $10 \text{ m}^2/\text{s}$ , while the crack size increases from 1cm to 5.5 cm [32]. However, the defect generated here is weak enough that  $D$  remains unchanged. This mimics an early stage surface crack initiation.

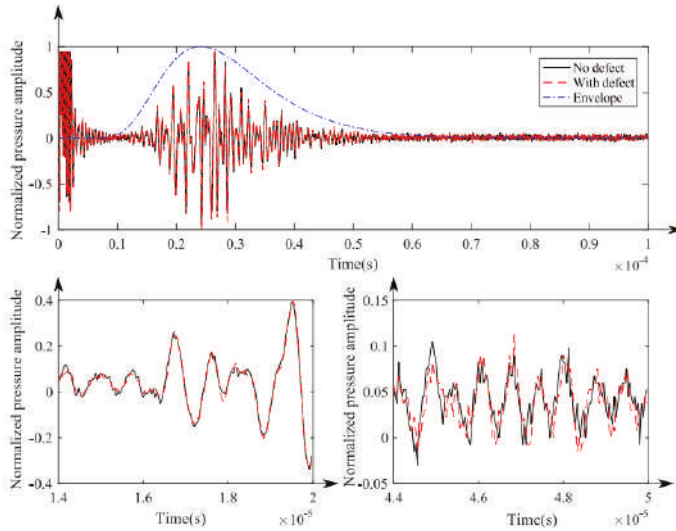


Figure 2. Representative waveforms from the S-R1 pair.

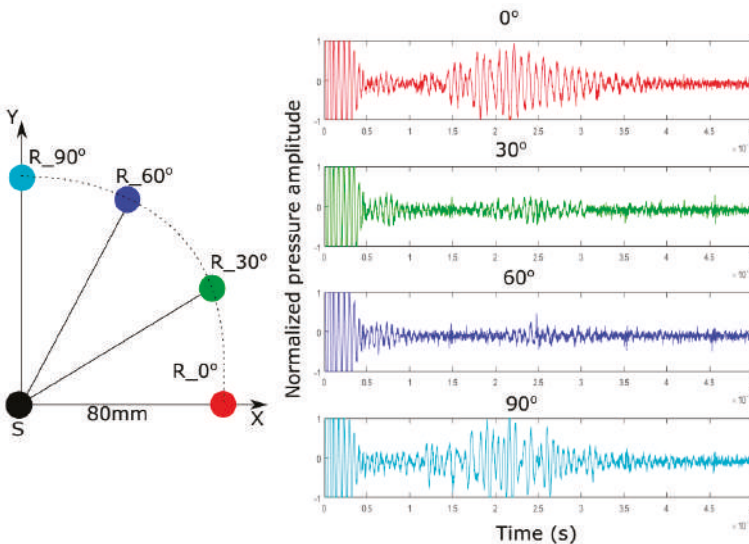


Figure 3. Waveforms from different directions at  $0^\circ$ ,  $30^\circ$ ,  $60^\circ$ , and  $90^\circ$ .

### 4. Results and Discussion

#### 4.1. Decorrelation Coefficient and Defect Sensitive Window

According to Equation (3), the correlation and decorrelation coefficients can be determined from the waveforms with and without a defect. The stretching method demonstrates great stability to external noise and is applied here [16]. The decorrelation coefficients can be calculated according to Equation (8):

$$DC(\varepsilon) = 1 - CC(\varepsilon) = 1 - \frac{\int_{t_1}^{t_2} h_k[t(1 - \varepsilon)]h_0[t]dt}{\sqrt{\int_{t_1}^{t_2} h_k^2[t(1 - \varepsilon)]dt \int_{t_1}^{t_2} h_0^2[t]dt}}, \tag{8}$$

in which the window length  $T = t_2 - t_1$  is set to 10  $\mu\text{s}$  and the beginning of the time window  $t_1$  is shifted sequentially with a time step of 5  $\mu\text{s}$  each time. The stretching factor  $\varepsilon$  is chosen to vary from  $-0.015$  to  $0.015$ , from which the decorrelation coefficient is decided when reaching the minimum (Figure 4). The total results for all decorrelation coefficients varied with time are shown in Figure 5. They all increase with time as a growing interaction between the diffuse wave field and the defect takes place. The maximum coefficients are found when  $t_1 = 45 \mu\text{s}$ , which is chosen for the defect localization study. S-R1 and S-R2 are more sensitive to the defect compared to that of S-R3 and S-R4 due to their different positions relative to the defect. After  $t_1 = 45 \mu\text{s}$ , the decorrelation coefficients decrease because of the reflection part interference and signal attenuation.

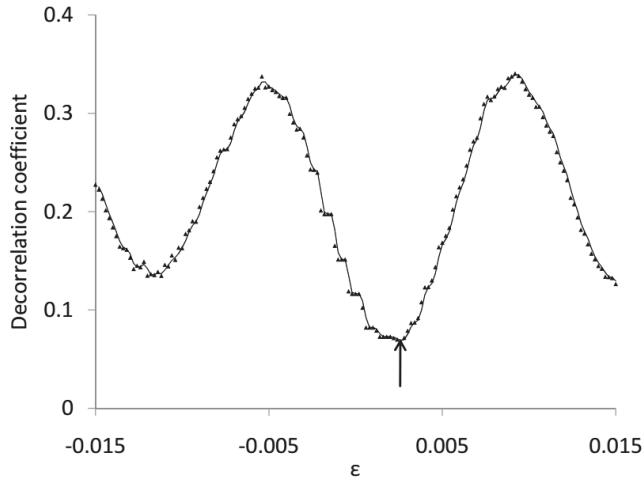


**Figure 4.** Decorrelation coefficient calculation example for the waveforms presented in Figure 2 when  $t_1 = 45 \mu\text{s}$  (decorrelation coefficient = 0.0679 when  $\varepsilon = 0.0026$ ).

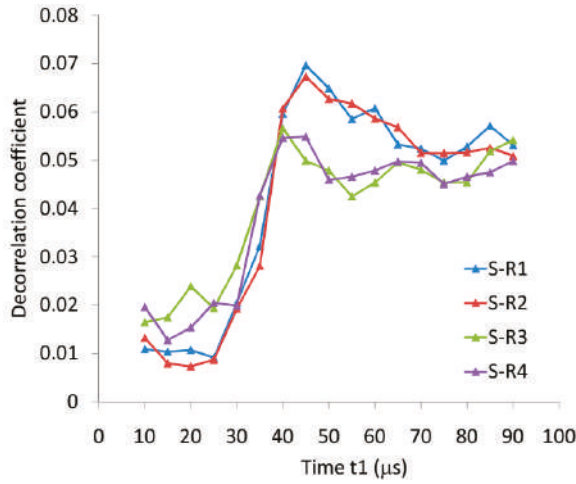


Figure 5. Decorrelation coefficients varied according to time.

4.2. Kernel Function

The defect sensitivity kernel represents the probability of a wave sent from location S to pass at location x and then to arrive at location R after period of time t [11]. Considering the source images due to the four straight boundaries of the plate, the detection diameter  $Z_{detection}$  is 260 mm when  $t = 45 \mu\text{s}$ , as shown in Figure 6 based on Equation (5). The diffuse wave field is mostly sensitive to the defect in this range. In fact, the diffusion model simplifies the energy distribution and neglects the diffuse field-defect interaction after  $t = 65 \mu\text{s}$ , as previously shown in Figure 2. All the pressure amplitudes are equal to zero in that period. The whole space is then discretized into  $300 \times 300$  elements for the possible location of the defect, and a further mesh refinement gives no more localization resolution improvement.

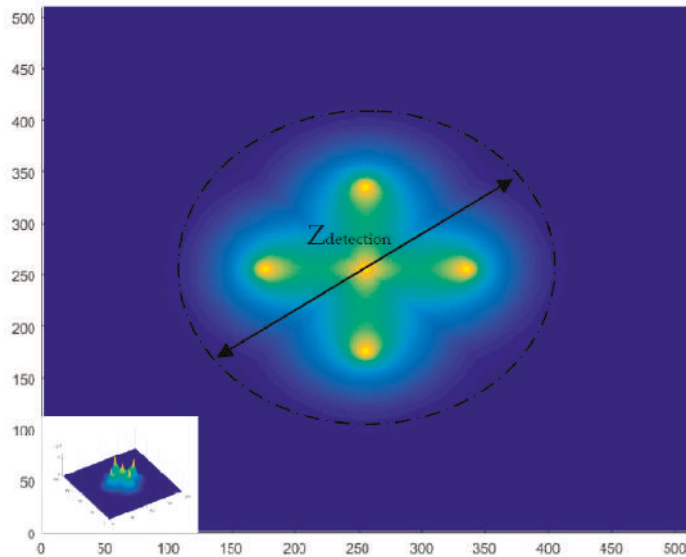


Figure 6. Sensitivity kernels and detection zone.

4.3. Defect Localization and Error Discussion

Once the decorrelation coefficients and kernel function have been calculated in the defined time domain, the localization is found to be in [270 mm, 265 mm] based on Equations (4)–(7), as shown in Figure 7. A further comparison is made among different time windows in Figure 8. The localization error varies from 13.5% to 6.7%. It decreases initially due to the increasing interaction between the diffuse wave and the defect. The direct reflection wave is estimated to arrive at the defect position at  $t_{reflection} = \frac{255+(255-80)}{8000} = 53 \mu s$ . Subsequently, the localization error increases because of the lowering sensitivity of the waveform to the defect shown in Figure 5, which may be caused by the reflection and attenuation. Although they suffer a lot from attenuation, which limits the inspection domain, a meaningful signal can still be extracted.

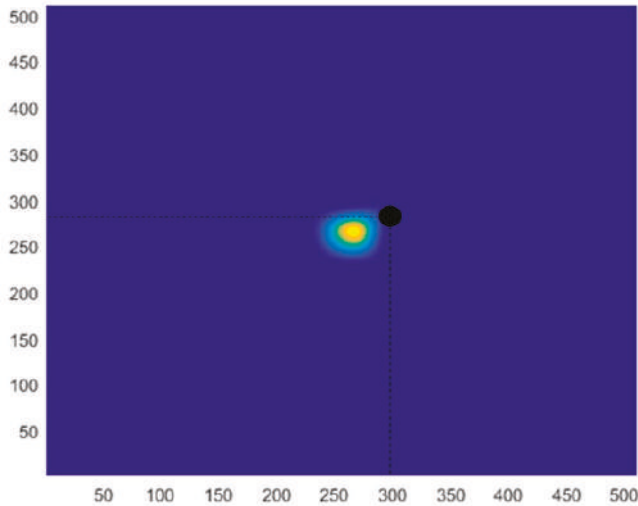


Figure 7. Localization image when  $t = 45 \mu s$ .

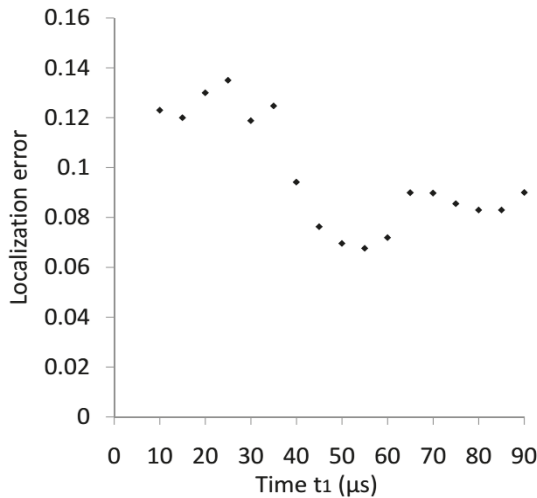


Figure 8. Localization error varied with time window.

In addition to the severe signal-to-noise ratio degradation due to viscoelasticity, the moderate defect localization deviation mainly comes from two aspects. Theoretically, wave diffusivity and dissipation parameters are assumed constant in the kernel calculation model, which varies according to the directional angles. This approximation contributes to the error in the kernel calculation and grid search procedure in Equation (6). Experimentally, the signal obtained from each pair is the averaged information from the sensor's field of view. Localization sensitivity may be lost to some extent so that error is introduced as well. The sensor diameter and distribution could be optimized in the future between the direction sensitivity and inspection efficiency in order to obtain high defect localization precision.

## 5. Conclusions

Fiber reinforced polymer composites can possess complex structures from macroscopic to microscopic scales, which makes their quality assurance difficult. Diffuse wave inspection relies on the multiple scattering process containing rich structure information. It gives a new insight into high frequency ultrasonic inspection for such viscoelastic, inhomogeneous, and anisotropic structures. The diffuse wave field is attenuated fast, while the decorrelation coefficient decreases first with increasing sensitivity to the defect and increases later because of signal-to-noise ratio degradation. Wave diffusivity is assumed constant under the measurement scheme only along the X and Y axes. The most defect sensitive time window is decided in the range of 45–55  $\mu$ s. Limited by the sensor diameter and waveform attenuation, the defect is found to locate at [270 mm, 265 mm] compared to [300 mm, 280 mm] in the intact state in the given window. This method is promising for early crack detection in various advanced composites in three dimensions. Since the diffuse wave is the statistical summation of random walk ray-paths [23], more experimental studies are expected for different fiber structures. Further investigation of how to distinguish signals from noises in diffuse waves is expected in viscoelastic media, which could be critical for defect localization.

**Author Contributions:** Data curation, Y.D.; formal analysis, D.T.; investigation, H.Z.; writing—original draft, Q.Z.; writing—review and editing, Y.P.

**Funding:** The work in this paper is supported by the Shanghai Sailing Program [No.18YF1408400] and the National Natural Science Foundation of China (Grant Nos.116742124, 11874255, 61673252).

**Conflicts of Interest:** The authors declare no conflicts of interest.

## References

1. Llewellyn-Jones, T.M.; Drinkwater, B.W.; Trask, R.S. 3D printed composites with ultrasonically arranged complex microstructure. *Smart Mater. Struct.* **2016**, *25*, 02LT01. [[CrossRef](#)]
2. Erb, R.M.; Libanori, R.; Rothfuchs, N.; Studart, A.R. Composites reinforced in three dimensions by using low magnetic fields. *Science* **2012**, *335*, 199–204. [[CrossRef](#)] [[PubMed](#)]
3. Raney, J.R.; Compton, B.G.; Mueller, J.; Ober, T.J.; Shea, K.; Lewis, J.A. Rotational 3D printing of damage-tolerant composites with programmable mechanics. *PNAS* **2018**, *115*, 1198–1203. [[CrossRef](#)] [[PubMed](#)]
4. Lascoup, B.; Perez, L.; Autrique, L. Defect localization based on modulated photothermal local approach. *Compos. Part B Eng.* **2014**, *65*, 109–116. [[CrossRef](#)]
5. Yang, B.; Xuan, F.Z.; Chen, S.; Zhou, S.; Gao, Y.; Xiao, B. Damage localization and identification in WGF/epoxy composite laminates by using Lamb waves: Experiment and simulation. *Compos. Struct.* **2017**, *165*, 138–147. [[CrossRef](#)]
6. Pearson, M.R.; Eaton, M.; Featherston, C.; Pullin, R.; Holford, K. Improved acoustic emission source location during fatigue and impact events in metallic and composite structures. *Struct. Heal. Monit.* **2017**, *16*, 382–399. [[CrossRef](#)]
7. Kalteremidou, K.-A.; Murray, B.; Tsangouri, E.; Aggelis, D.; Van Hemelrijck, D.; Pyl, L. Multiaxial damage characterization of carbon/epoxy angle-ply laminates under static tension by combining in situ microscopy with acoustic emission. *Appl. Sci.* **2018**, *8*, 2021. [[CrossRef](#)]

8. Niccolini, G.; Borla, O.; Accornero, F.; Lacidogna, G.; Carpinteri, A. Scaling in damage by electrical resistance measurements: An application to the terracotta statues of the Sacred Mountain of Varallo Renaissance Complex (Italy). *Rend. Lincei* **2015**, *26*, 203–209. [[CrossRef](#)]
9. Chen, B.; Liu, J. Damage in carbon fiber-reinforced concrete, monitored by both electrical resistance measurement and acoustic emission analysis. *Constr. Build. Mater.* **2008**, *22*, 2196–2201. [[CrossRef](#)]
10. Snieder, R. Time-reversal invariance and the relation between wave chaos and classical chaos. In *Imaging of Complex Media with Acoustic and Seismic Waves*; Flink, M., Kuperman, W.A., Montagner, J.-P., Tourin, A., Eds.; Springer: Berlin, Germany, 2002; pp. 1–16.
11. Xie, F.; Larose, E.; Moreau, L.; Zhang, Y.; Planes, T. Characterizing extended changes in multiple scattering media using coda wave decorrelation: Numerical simulations scattering media. *Waves Random Complex Media* **2018**, *5030*, 1–14. [[CrossRef](#)]
12. Larose, E.; Obermann, A.; Digulescu, A.; Planès, T.; Chaix, J.-F.; Mazerolle, F.; Moreau, G. Locating and characterizing a crack in concrete with diffuse ultrasound: A four-point bending test. *J. Acoust. Soc. Am.* **2015**, *138*, 232–241. [[CrossRef](#)] [[PubMed](#)]
13. Biswal, P.; Reddy, B.N.; Srinivasa, M.B.P. Manufacturing aspects of fabrication of composite reference standard for NDT ultrasonic inspection. In Proceedings of the AeroNDT, Bangalore, India, 3–5 November 2016.
14. Hennings, B.; Lammering, R. Material modeling for the simulation of quasi-continuous mode conversion during Lamb wave propagation in CFRP-layers. *Compos. Struct.* **2016**, *151*, 142–148. [[CrossRef](#)]
15. Aki, K.; Chouet, B. Origin of coda waves: Source, attenuation, and scattering. *J. Geophys. Res.* **1975**, *80*, 3322–3342. [[CrossRef](#)]
16. Hadziioannou, C.; Larose, E.; Coutant, O.; Roux, P.; Campillo, M. Stability of monitoring weak changes in multiply scattering media with ambient noise correlation: Laboratory experiments. *J. Acoust. Soc. Am.* **2009**, *125*, 3688–3695. [[CrossRef](#)] [[PubMed](#)]
17. Lobkis, O.I.; Weaver, R.L. On the emergence of the Green's function in the correlations of a diffuse field. *Ultrasonics* **2001**, *110*, 3011–3017. [[CrossRef](#)]
18. Sens-Schonfelder, C.; Larose, E. Lunar noise correlation, imaging and monitoring. *Earthq. Sci.* **2010**, *23*, 519–530. [[CrossRef](#)]
19. Potter, J.N.; Wilcox, P.D.; Croxford, A.J. Diffuse field full matrix capture for near surface ultrasonic imaging. *Ultrasonics* **2018**, *82*, 44–48. [[CrossRef](#)] [[PubMed](#)]
20. Stahler, S.C.; Sens-Schonfelder, C.; Niederleithinger, E. Monitoring stress changes in a concrete bridge with coda wave interferometry. *J. Acoust. Soc. Am.* **2011**, *129*, 1945–1952. [[CrossRef](#)]
21. Zhang, Y.; Abraham, O.; Tournat, V.; Le Duff, A.; Lascoup, B.; Loukili, A.; Grondin, F.; Durand, O. Validation of a thermal bias control technique for Coda Wave Interferometry (CWI). *Ultrasonics* **2013**, *53*, 658–664. [[CrossRef](#)]
22. Shokouhi, P. Stress- and damage-induced changes in coda wave velocities in concrete. In Proceedings of the AIP Conference Proceedings, Denver, CO, USA, 15–20 July 2012.
23. Snieder, R. The Theory of Coda Wave Interferometry. *Pure Appl. Geophys.* **2006**, *163*, 455–473. [[CrossRef](#)]
24. Rossetto, V.; Margerin, L.; Planes, T.; Larose, E. Locating a weak change using diffuse waves: Theoretical approach and inversion procedure. *J. Appl. Phys.* **2011**, *109*, 034903. [[CrossRef](#)]
25. Kundu, T.; Yang, X.; Nakatani, H.; Takeda, N. A two-step hybrid technique for accurately localizing acoustic source in anisotropic structures without knowing their material properties. *Ultrasonics* **2015**, *56*, 271–278. [[CrossRef](#)] [[PubMed](#)]
26. Zhang, Y.; Larose, E.; Moreau, L.; d'Ozouville, G. Three-dimensional in-situ imaging of cracks in concrete using diffuse ultrasound. *Struct. Heal. Monit.* **2018**, *17*, 279–284. [[CrossRef](#)]
27. Xie, F.; Ren, Y.; Zhou, Y.; Larose, E.; Baillet, L. Monitoring local changes in granite rock under biaxial test: A spatiotemporal imaging application with diffuse waves. *J. Geophys. Res. Solid Earth* **2018**, *123*, 2214–2227. [[CrossRef](#)]
28. Zhu, Q.; Binetruy, C.; Burtin, C. Internal stress determination in a polymer composite by Coda wave interferometry. In Proceedings of the IOP Conference Series: Materials Science and Engineering, Hangzhou, China, 20–23 May 2016.
29. Livings, R.; Dayal, V.; Barnard, D. Feasibility of detecting fatigue damage in composites with Coda waves. In Proceedings of the AIP Conference Proceedings, Boise, ID, USA, 20–25 July 2014.

30. Patra, S.; Banerjee, S. Material state awareness for composites part I: Precursor damage analysis using ultrasonic guided coda wave interferometry (CWI). *Materials* **2017**, *10*, 1436. [[CrossRef](#)] [[PubMed](#)]
31. Pomarède, P.; Chehami, L.; Declercq, N.F.; Meraghni, F.; Dong, J.; Locquet, A.; Citrin, D.S. Application of ultrasonic Coda wave interferometry for micro-cracks monitoring in woven fabric composites. *J. Nondestruct. Eval.* **2019**, *38*, 26. [[CrossRef](#)]
32. Quiviger, A.; Payan, C.; Chaix, J.; Garnier, V.; Salin, J. Characterizing extended changes in multiple scattering media using coda wave decorrelation. *NDT E Int.* **2012**, *45*, 128–132. [[CrossRef](#)]
33. Kanu, C.; Snieder, R. Numerical computation of the sensitivity kernel for monitoring weak changes with multiply scattered acoustic waves. *Geophys. J. Int.* **2015**, *203*, 1923–1936. [[CrossRef](#)]
34. Planeès, T.; Larose, E.; Rossetto, V.; Margerin, L. LOCADIFF: Locating a weak change with diffuse ultrasound. In Proceedings of the AIP Conference Proceedings, Denver, CO, USA, 15–20 July 2012.
35. Planès, T.; Larose, E.; Rossetto, V.; Margerin, L. Imaging multiple local changes in heterogeneous media with diffuse waves. *J. Acoust. Soc. Am.* **2015**, *137*, 660–667. [[CrossRef](#)] [[PubMed](#)]
36. Xie, F.; Moreau, L.; Zhang, Y.; Larose, E. A Bayesian approach for high resolution imaging of small changes in multiple scattering media. *Ultrasonics* **2016**, *64*, 106–114. [[CrossRef](#)] [[PubMed](#)]
37. Williams, J.H.; Nayeb-Hashemi, H.; Lee, S.S. Ultrasonic attenuation and velocity in AS/3501-6 graphite fiber composite. *J. Nondestruct. Eval.* **1980**, *1*, 137–148. [[CrossRef](#)]
38. Chehami, L.; Moulin, E.; De Rosny, J.; Prada, C.; Assaad, J.; Benmeddour, F. Experimental study of passive defect detection and localization in thin plates from noise correlation. *Phys. Procedia* **2015**, *70*, 322–325. [[CrossRef](#)]
39. Carpinteri, A.; Xu, J.; Lacidogna, G.; Manuello, A. Reliable onset time determination and source location of acoustic emissions in concrete structures. *Cem. Concr. Compos.* **2012**, *34*, 529–537. [[CrossRef](#)]
40. Mei, H.; Haider, M.F.; Joseph, R.; Migot, A.; Giurgiutiu, V. Recent advances in piezoelectric wafer active sensors for structural health monitoring applications. *Sensors* **2019**, *19*, 383. [[CrossRef](#)] [[PubMed](#)]



© 2019 by the authors. Licensee MDPI, Basel, Switzerland. This article is an open access article distributed under the terms and conditions of the Creative Commons Attribution (CC BY) license (<http://creativecommons.org/licenses/by/4.0/>).

Article

# Assessment of Residual Elastic Properties of a Damaged Composite Plate with Combined Damage Index and Finite Element Methods

Carlo Boursier Niutta \*, Andrea Tridello, Raffaele Ciardiello, Giovanni Belingardi and Davide Salvatore Paolino

Department of Mechanical and Aerospace Engineering, Politecnico di Torino, 10129 Turin, Italy; andrea.tridello@polito.it (A.T.); raffaele.ciardiello@polito.it (R.C.); giovanni.belingardi@polito.it (G.B.); davide.paolino@polito.it (D.S.P.)

\* Correspondence: carlo.boursier@polito.it

Received: 29 May 2019; Accepted: 21 June 2019; Published: 25 June 2019

**Abstract:** In structural component applications the use of composite materials is increasing thanks to their optimal mechanical characteristics. However, the complexity of the damage evolution in composite materials significantly limits their widespread diffusion. Non-destructive tests are thus becoming ever more important. The detecting Damage Index ( $DI_d$ ) technique has been recently brought in the realm of the non-destructive characterization tests for components made of composite material. In contrast to other techniques, this methodology allows to quantitatively assess local residual properties. In this paper, the  $DI_d$  technique is adopted in combination with the finite element method. The mechanical response of two composite plates (an 8-layer twill fabric carbon/epoxy) subjected to four-point bending test is firstly used to tune a finite element model of the laminate. Then, an undamaged laminate of the same composite material is progressively damaged through repeated four-point bending tests. Local residual elastic properties are mapped on the plate through the  $DI_d$  technique. A continuous polynomial curve has been considered to account for the variation of the elastic modulus in the finite element model. The resulting force-displacement curve of the numerical analysis is compared to experimental data of damaged plate, resulting in very good agreement. The combination of the experimental activity and the numerical finite element analysis points out the accuracy of the  $DI_d$  methodology in assessing local residual elastic properties of composite materials.

**Keywords:** non-destructive tests; damage assessment; residual properties; Finite Element Method; Damage Index

## 1. Introduction

Composite materials are increasingly adopted in structural–mechanical applications thanks to their optimal characteristics in terms of light weight, mechanical strength and stiffness, corrosion resistance, energy absorption capacity, and noise attenuation. However, many factors limit their widespread diffusion, such as the high cost of raw materials or requirements for high production volumes. Among the others, the complexity of the damage evolution plays a key role in their limitation, especially for structural component applications. Several interacting failure modes are typical of composite materials and a progressive and rapid decrement of the mechanical properties can be observed [1].

In this regard, methodologies for assessing damage level and predicting the residual structural strength of composite materials are becoming increasingly important. Many techniques have been developed for non-destructively assessing the structural health state of composite components [2]. Non-destructive tests (NDTs) are commonly adopted for quality assessment of a manufacturing process

or for damage evaluation in structures during service. Most of the techniques intend to provide information on internal damages, in terms of size, shape, location, and orientation. Microscopy (based on atomic force, optic system, and scanning and transmission electron) [3], X-ray micro-CT (micro-computed tomography) [3,4], and infrared thermography [3,5] are among the most used for composite applications. However, the qualitative information provided by these techniques can be exploited by designers with difficulty. Further, methods based on ultrasounds and vibrational analysis are usually adopted for globally analyzing the dynamic response of a structure [6]. In particular, the use of the Impulse Excitation Technique (IET), which is regulated by ASTM Standards for metallic materials [7,8], has been recently extended to composite specimens [9]. However, local damages and defects are still revealed with difficulty in real-world structures since the presence of anomalies is mitigated by the global response of the system. Therefore, as pointed out in [10], current methodologies do not allow a direct evaluation of the local residual properties.

In this paper, the detecting Damage Index ( $DI_d$ ) technique was adopted for assessing the local residual elastic properties of a composite laminate. This methodology was brought in the realm of the non-destructive characterization for components made of composite material by Belingardi et al. in [11–15]. The  $DI_d$  technique consists of two sets of experimental tests: a preliminary characterization activity which is performed to identify the correlation between residual elastic properties of the material and the  $DI_d$  parameter and the proper non-destructive test to estimate the local residual elastic properties of the investigated component from the  $DI_d$ . In [15], the methodology was demonstrated to properly predict residual elastic properties of a series of laminate plates damaged through impacts at different energy levels. Tensile tests on specimens cut from laminate plates allowed validation of results predicted with the  $DI_d$ . Here, the finite element method was adopted to validate elastic properties assessed with the  $DI_d$ . The combination of non-destructive tests and finite element method is typical in damage assessment, particularly in vibration-based techniques [16]. Various approaches are available to numerically model multi-layered composite materials and their multiple failure modes [17,18]. In particular, the use of cohesive elements disposed between layers of shells currently represents one of the most adopted solutions [19–21]. Thanks to their specific formulation, cohesive elements allow to simulate damages due to delamination without significantly affecting computational cost.

In this paper, the  $DI_d$  technique is thus used in combination with the finite element method. An 8 layers twill fabric carbon/epoxy composite laminate is firstly damaged through repeated four-point bending tests. Then, the  $DI_d$  technique is adopted to map the residual elastic properties on the damaged plate. The variation of the Young's modulus is accounted in the finite element model of the laminate subjected to bending test through a continuous polynomial curve. The resulting experimental and numerical force-displacement curves are then compared to validate the proposed methodology. The combination of the experimental activity and the numerical finite element analysis points out the accuracy and the effectiveness of the  $DI_d$  methodology in predicting the local residual elastic properties of damaged composite components.

## 2. Materials and Methods

In this section, investigated materials are firstly detailed. Then experimental and numerical methods are presented.

### 2.1. Materials

Experimental tests are performed on a structural composite laminate specifically developed for automotive application. The composite material is the same adopted by Tridello et al. in their investigations [15] and previously in [9]. It consists of a matrix made of epoxy resin reinforced by eight layers of twill woven carbon fabric. The first layer is a 380 gsm fabric with 0.45 mm thickness and an 800 gsm fabric with 0.88 mm thickness is used in the remaining seven layers. The stacking sequence is  $[0/90]_8$ . In the numerical analysis, the laminate is modeled as symmetric, with 8 layers of thickness 0.88 mm, oriented according to the stacking sequence. A total thickness of 7.04 mm is

thus obtained. Even though the first layer is different from the other seven, this difference can be neglected when considering the global mechanical behavior of the laminate. The measured elastic properties (Young’s modulus, shear modulus, and Poisson’s ratio) are reported in Table 1, as assessed in [9]. Given the symmetry of the woven fabric, the mechanical properties and the Poisson’s ratios in the in-plane direction 1 and 2 are the same (i.e.  $E_1 = E_2, \nu_{12} = \nu_{21}$ ).

Table 1. Material properties.

| Property   | Value                            |
|--|----------------------------------|
| Density  | $1.45 \cdot 10^3 \text{ g/cm}^3$ |
| Young’s modulus in longitudinal and transverse direction ( $E_1 = E_2$ ) | 54 GPa                           |
| Shear modulus ( $G_{12}$ )   | 3.5 GPa                          |
| Poisson’s ratio ( $\nu_{12} = \nu_{21}$ )                                | 0.08                             |

2.2. Experimental Tests

Four-point bending tests are performed on two different composite plates until complete failure occurs. The elastic field of the composite plates is thus identified. The tests are performed on a servohydraulic testing machine (Instron 8801). In agreement with the recommendations of ASTM standard D6272 for four-point bending test of reinforced plastics [22], the load span is one third of the support span. As shown in Figure 1, the loading noses are 50 mm distant. The support noses are consequently placed at a distance of 150 mm. Figure 1a shows the experimental setup. The resulting experimental curves of force with respect to displacement are exploited to tune a finite element model of the laminate subjected to four-point bending test, which is shown in Figure 1b.

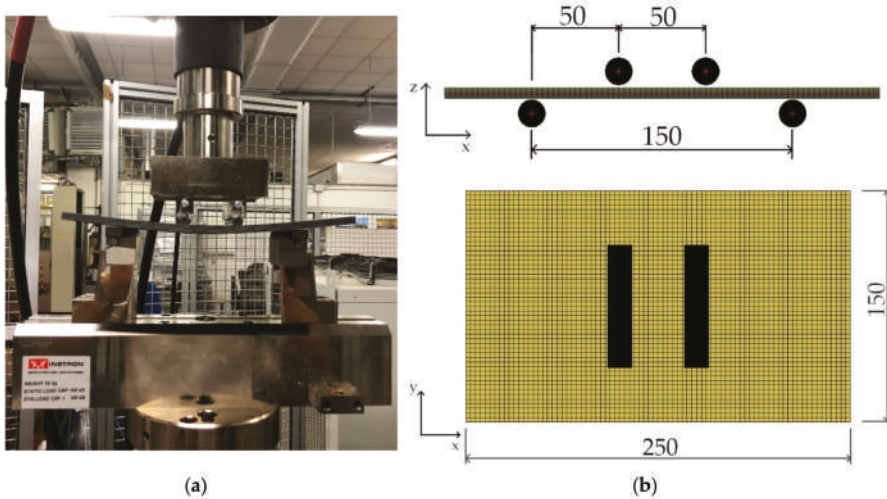


Figure 1. Four-point bending test: (a) experimental setup; (b) numerical model.

The same experimental setup is adopted to progressively damage an undamaged composite plate. The plate is loaded until incipient failure occurs and then unloaded. The repeated four-point bending tests progressively reduce plate stiffness. A significant damage level is thus induced.

In order to assess the residual Young’s modulus of the damaged plate, the detecting Damage Index ( $DI_d$ ) technique is adopted. The  $DI_d$  methodology consists of two sets of experimental tests. Firstly, a preliminary characterization activity is performed, which allows to identify the correlation between residual elastic properties and the  $DI_d$  parameter. Then, the investigated component undergoes the non-destructive test in order to estimate the local residual elastic properties from the  $DI_d$ .

In particular, the methodology is based on two sets of impact tests: the first intends to damage the material at increasing impact energy levels and allows to evaluate the so-called threshold energy  $\epsilon_{th}$ . The threshold energy is defined as the impact energy at which the reduction of local elastic properties is less than 5%. An impact at the threshold energy can be considered as non-destructive for the material. The second set of impacts is performed at the threshold energy and allows to evaluate the residual elastic properties.

In this work, the first series of impacts were performed on a set of plates made of the same composite fabric. The impact tests were carried out using a free-fall drop dart testing machine (CEAST 9350 FRACTOVIS PLUS). Clamping boundary conditions were realized through a mechanical clamping system which applies an almost uniform pressure on the clamped area. A circular unclamped region of diameter 76 mm was considered for the tests, in agreement with the recommendations of ASTM standard D5628 [23]. The impact energy was defined by varying the impactor mass for a given impact velocity. The impact velocity, which was controlled by the drop height of the dart, was measured in each test with an optoelectronic device. A piezoelectric load cell, mounted in proximity of the tip of the impact dart, acquired the force signal at a sample rate of 1 MHz.

The second series of impacts, which are carried out at the threshold energy, is performed on the plate previously damaged with the repeated four-point bending tests. In particular, damaged plate is impacted along the middle line. Moving along the longitudinal direction of the plate (x direction of Figure 1), the impacts are located in correspondence of the external noses, in the regions where bending moment is linearly increasing, in correspondence of the internal noses and finally in the middle of the load span. Seven impacts are applied in total to the plate, as shown in Figure 2. The corresponding residual Young's modulus is calculated from the  $DI_d$  parameter, which is defined as

$$DI_d = \frac{\epsilon_a}{\epsilon_{th}} \cdot \frac{s_{MAX}}{s_{QS}}$$

where  $\epsilon_a$  is the absorbed energy,  $\epsilon_{th}$  the threshold energy,  $s_{MAX}$  the maximum displacement and  $s_{QS}$  the displacement obtained in quasi static perforation test. The  $s_{MAX}$  and  $\epsilon_a$  values are computed through numerical integrations of the load signal acquired during the impact test.

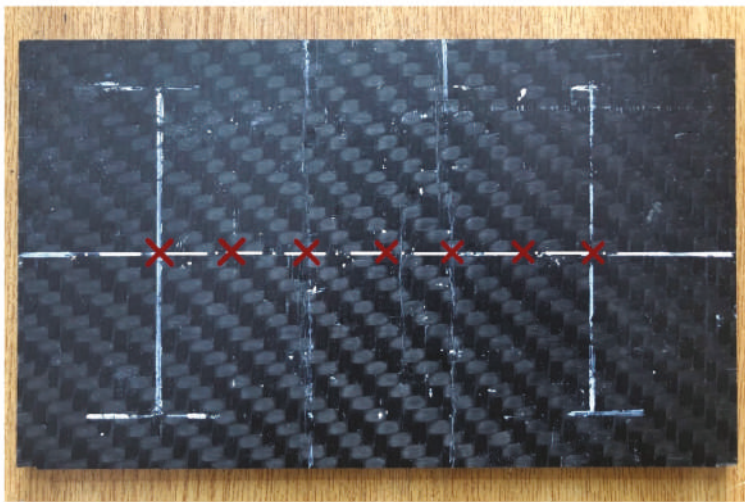


Figure 2. Location of impacts for  $DI_d$  analysis.

### 2.3. Numerical Model

A structural–mechanical model of the four-point bending test was simulated using the commercial software LS-DYNA. The 8 layers of the woven fabric composite were modeled with Belytschko-Tsai 4-node shell elements, with one integration point through the thickness. For each layer of the composite, a layer of shell elements was considered. Solid elements of cohesive material were placed between the shell layers, in order to represent the resin among layers. Solid elements of cohesive consider a specific formulation of LS-DYNA, which allows the transfer of moments to the shells. In particular, nodes of solid elements coincide with those of the shells. The material card \*MAT\_LAMINATED\_COMPOSITE\_FABRIC, which is specific for fabric composite, was adopted for the composite layers. This material model assumes a slightly modified version of Hashin criteria for failure [18]. However, in this paper, the focus is on the elastic field, and parameters related to the post-failure behavior of the material will not be addressed. The cohesive material model \*MAT\_COHESIVE\_TH, with properties of the resin, was assigned to the cohesive elements. Finally, the span noses were modeled as rigid cylinder walls. The upper cylinders, shown in Figure 1b, move downwards with a prescribed motion law. The upper and lower cylinders were placed at the initial distance of 1 mm from the laminate in order to avoid penetrations and numerical instabilities. Contact between laminate and cylinders was based on a penalty formulation with a penalty factor which adaptively guarantees the numerical stability [24]. This formulation accounts for thickness offsets of shells.

The accuracy of the numerical model was firstly verified with respect to the four point-bending tests of the two composite plates. Then, the same numerical model was used in comparison with the experimental results of the progressively damaged plate. In this case, the structural–mechanical model had to account for the variation of Young’s modulus on the plate, as pointed out through the  $DI_d$  technique.

The residual elastic properties of the damaged plate are mapped through the  $DI_d$  technique. The Young’s modulus varies along the x-direction according to the location of measurement, with the damage mostly located in correspondence of internal rolls. It seems reasonable to assume that the Young’s modulus varies continuously along the longitudinal direction. Here, a polynomial curve is considered for each region included between two consecutive measure locations.

For each polynomial curve, the two Young’s moduli at the extremities,  $E_k$  and  $E_{k+1}$ , with k the considered location, are known.

In addition, the two derivatives at the extremities can be estimated. In order to evaluate the derivatives, the difference quotient for each region has been calculated as

$$\frac{\Delta E_k}{\Delta x_k} = \frac{E_k - E_{k-1}}{x_k - x_{k-1}} \tag{1}$$

in accordance with its definition.

The difference quotient is a measure of the average rate of change of the function, here the Young’s modulus, over the interval  $\Delta x_k$ . By considering two consecutive difference quotients,  $\frac{\Delta E_k}{\Delta x_k}$  and  $\frac{\Delta E_{k+1}}{\Delta x_{k+1}}$ , the derivative at the k-th location has been estimated as follows:

1. when the product  $\frac{\Delta E_k}{\Delta x_k} \cdot \frac{\Delta E_{k+1}}{\Delta x_{k+1}}$  returns a negative value, the derivate at the k-th location is assumed equal to zero. This can be justified by considering that a change in the sign of the difference quotient implies a change in the derivative of the function, as well;
2. when the sign of the product  $\frac{\Delta E_k}{\Delta x_k} \cdot \frac{\Delta E_{k+1}}{\Delta x_{k+1}}$  is positive, the derivate at the k-th location is assumed equal to average value  $\frac{\frac{\Delta E_k}{\Delta x_k} + \frac{\Delta E_{k+1}}{\Delta x_{k+1}}}{2}$ ;
3. the derivatives at the extremities,  $k = 1$  and  $k = 7$ , are assumed equal to zero.

As the two Young's moduli and the derivatives are known at the extremities, a third-order polynomial curve can be constructed for each interval included between two consecutive impact locations. This approach guarantees the continuity of the Young's modulus with respect to the x-coordinate.

In the structural–mechanical model, this variation was accounted by longitudinally dividing the layers of shells into parts. Each part consisted of one row of shell elements and is identified by its x-coordinate. In particular, each part could be longitudinally localized in correspondence of the middle of the element size. In this work, a mesh of 3 mm was adopted. According to the location of the part in the x direction, the corresponding third-order polynomial curve could be identified. The Young's modulus was consequently calculated. A material card was defined for each part with the corresponding elastic properties.

### 3. Results

In this Section, the experimental and numerical results are presented. In Section 3.1, experimental and numerical data related to the four-point bending tests are compared. In Section 3.2, results of the progressive damaging of the composite plate through the repeated four-point bending tests are shown. Residual elastic properties are thus estimated through the  $DI_d$  methodology. The Young's modulus is mapped with respect to the longitudinal coordinate and the third-order polynomial curves were constructed as previously described. Finally, in Section 3.3, the proposed approach is validated by comparing the experimental results of the progressively damaged plate with the numerical model which accounts for the residual properties.

#### 3.1. Four-Point Bending Test: Experimental Results and Numerical Model Tuning

Results of the four-point bending tests are here presented. Two undamaged composite plates have been tested until almost complete failure occurred. In particular, the upper layers, which are subjected to compressive loads, showed the most significant failures. Intralaminar cracks propagate in correspondence of the inner span noses. The numerical model is analyzed only in the elastic field and it results in good agreement with the experimental data, as shown in Figure 3. Displacement of the numerical analysis has been evaluated on the rigid cylinders. However, as described in Section 2.2, the rigid wall cylinders are initially distanced from the composite laminate. Consequently, the initial path of the force-displacement curve is characterized by the growing contact between laminate and cylinders, which is not significant for the purpose. The numerical force-displacement curve has been thus shifted leftwards and results of the numerical analysis are reported from 1 mm of displacement.

Figure 4 shows a magnification of the cracks, obtained through an optical microscope. The complete failure can be appreciated for the upper four layers.

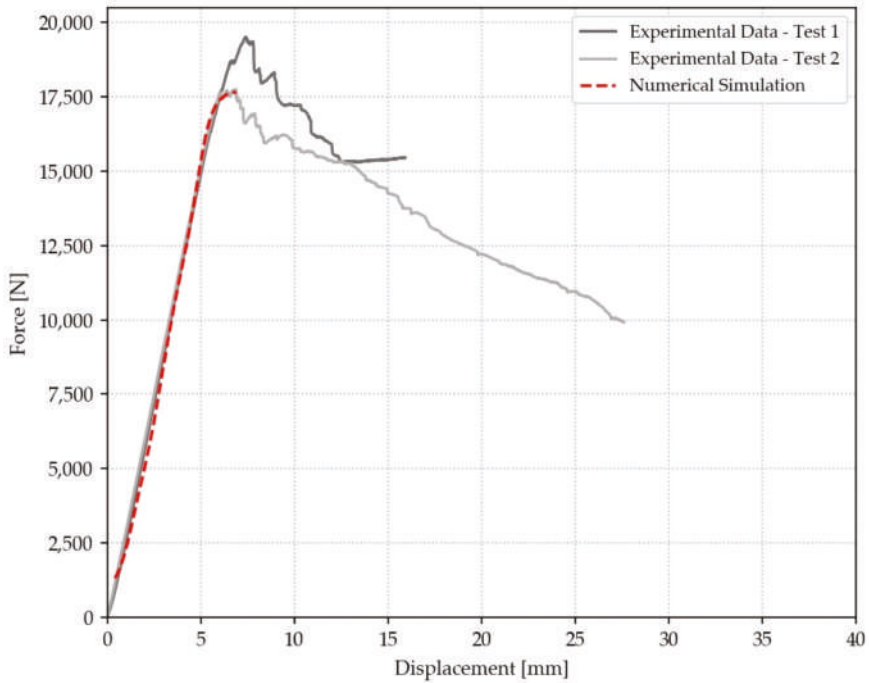


Figure 3. Experimental and numerical results of the four-point bending tests.

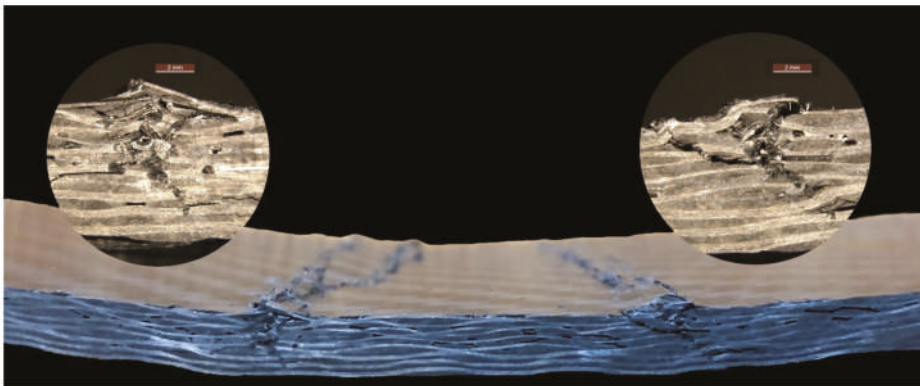


Figure 4. Magnification of intralaminar cracks: failure of the upper four layers.

### 3.2. Progressive Damaging and Assessment of Residual Elastic Properties through the $DI_d$ Technique

An undamaged composite is subjected to repeated four-point bending tests. Load is increased until incipient failure occurs and then decreased. Achieved failure is not complete, as the load-carrying capacity of the composite laminate is still significant. In total, five repetitions are performed, as shown in Figure 5, where the resulting force-displacement curves are numbered as Test n.1, Test n.2, Test n.3, Test n.4, and Test n.5. As the damage increases, the plate stiffness progressively decreases. Loading and unloading cycles are performed until the residual stiffness of the composite plate is about 40% of the original value. This is shown with the Test n.6 (damaged specimen curve), which is performed only in the elastic field. A significant damage level is thus induced through the five tests.

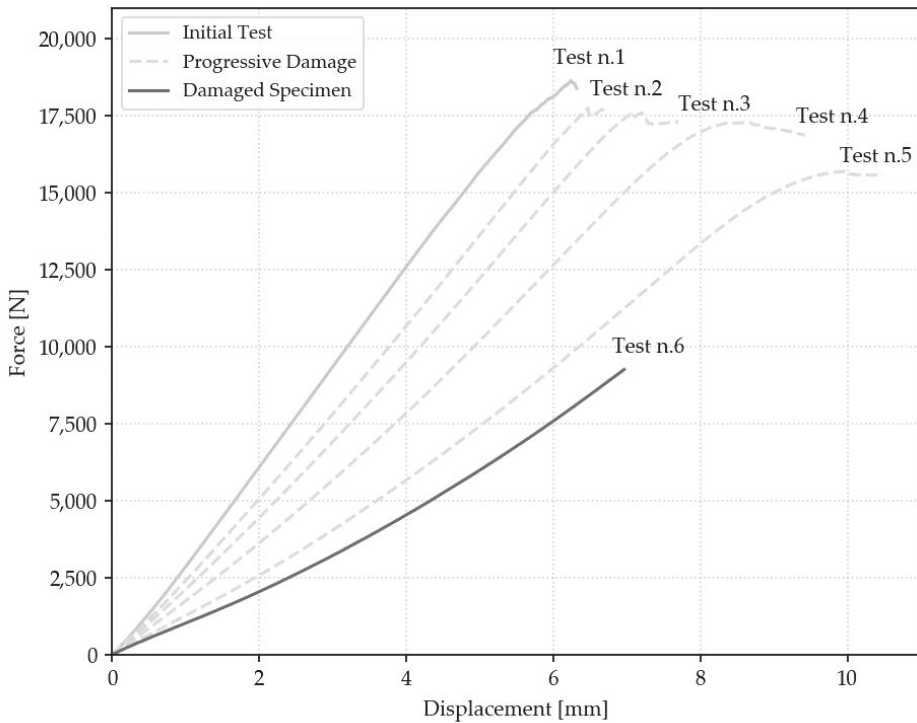


Figure 5. Progressive damaging of composite plate through four-point bending tests.

The  $DI_d$  technique is then adopted to estimate the residual elastic properties. Preliminary characterization tests allowed to evaluate the threshold energy  $\varepsilon_{th}$ , which is in this case equal to 5 J. Details of the preliminary tests are not discussed here. A complete description of the procedure can be found in [15].

Figure 6 shows the resulting correlation between the residual elastic properties of the analyzed composite and the  $DI_d$  parameter. The dotted line is thus adopted to evaluate the residual elastic properties in the progressively damaged plate. Cross markers correspond to the preliminary characterization tests.

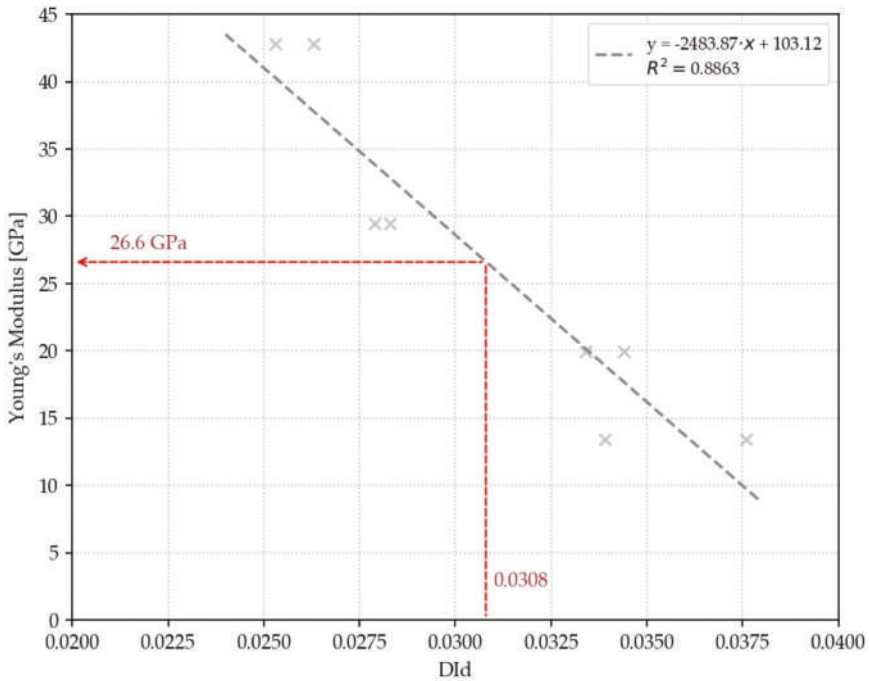


Figure 6. Residual Young's modulus evaluation with  $DI_d$ .

As reported in Figure 2, the elastic properties have been estimated at seven locations along the middle line of the composite plate. Table 2 reports the measured  $DI_d$  values and the corresponding Young's moduli, as well as the locations in x direction of the impacts.

Table 2. Residual Young's moduli and corresponding  $DI_d$  values at specific locations.

| X-Coordinate [mm] | $DI_d$ | $E_{res}$ [GPa] |
|-------------------|--------|-----------------|
| 50                | 0.0283 | 32.8            |
| 75                | 0.0297 | 29.5            |
| 100               | 0.036  | 13.7            |
| 125               | 0.0308 | 26.6            |
| 150               | 0.036  | 13.7            |
| 175               | 0.0297 | 29.5            |
| 200               | 0.0283 | 32.8            |

In correspondence of the external noses, whereas the bending moment is null in the four-point bending test and no damage should be present, the elastic modulus is equal to 32.8 GPa, which is significantly different from the original value of 54 GPa. This can be justified by taking into account that the circular unclamped region considered for the  $DI_d$  test has a diameter of 76 mm. Consequently, elastic properties are assessed as an average of the unclamped region.

Further, as clamping boundary conditions have to be realized all around the laminate, the diameter of 76 mm limits the region where the residual properties can be measured through the  $DI_d$ . Moving outwards from the external noses, only few measurements of the residual properties can be realized and results would be affected by the damaged portion of the plate. On the basis of these considerations, we can assume that, at a distance of 38 mm from the external noses (half of the diameter), the damaged

portion of the plate would not affect an ideal measurement through the  $DI_d$ . The Young's modulus is thus here considered equal to the original value of 54 GPa.

From the seven measurements of the Young's modulus and considering the two assumed external values, eight third-order polynomial curves can be constructed, according to the approach described in Section 2.2. As a consequence, a continuous variation of the Young's modulus with respect to the x-coordinate is obtained. This result is shown in Figure 7, where measured Young's moduli are marked with red squares and assumed values with black thin diamonds. The continuous curve is adopted in the numerical model to account for the variation of the Young's modulus. Layers of shells have been longitudinally divided into parts, which are represented with different colors in Figure 8. The continuous curve allows to evaluate the Young's modulus in correspondence of the x-coordinate of each part. A material card has been defined for each part with the corresponding elastic properties. Cross markers of Figure 7 represent the Young's moduli assigned to each material card.

Moving outwards from the external noses, the elastic modulus increases from 32.8 to 54 GPa and then is assumed constant. It should be noted that, as the bending moment is here null, the mechanical behavior of the numerical model will not be affected by the value of the elastic modulus estimated for this region.

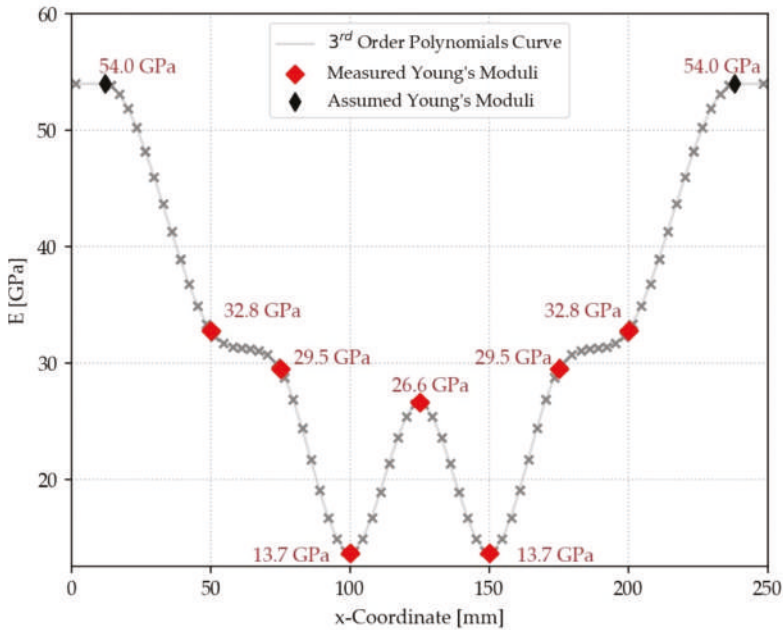
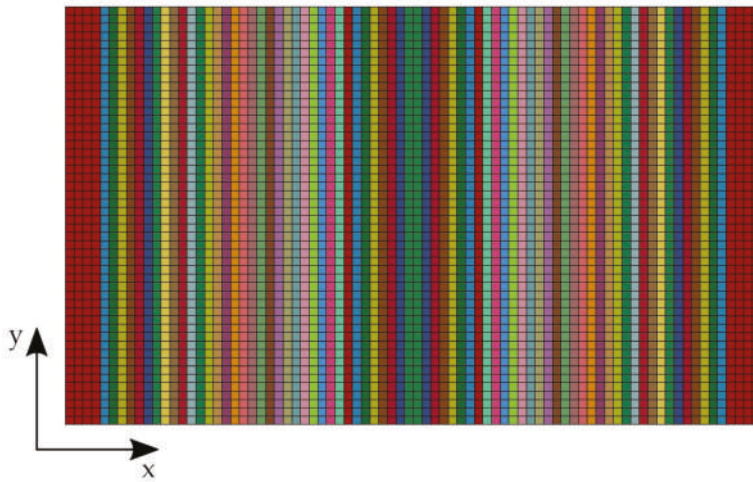


Figure 7. Variation of residual Young's modulus with respect to the x-coordinate.



**Figure 8.** Top view of the finite element model of the composite laminate: longitudinal division of layers.

### 3.3. Validation: Comparison of Experimental and Numerical Results

The model of the composite plate with variable elastic modulus is adopted for simulating the four-point bending test. Results of the numerical force-displacement curve are then compared to those obtained with the progressively damaged plate. As shown in Figure 9, experimental and numerical results are in very good agreement, with limited discrepancies in slope. Results of numerical analysis are once again reported from 1 mm of displacement. The numerical displacement is measured on the rigid cylinders and these are initially distanced from the composite laminate, in order to avoid penetrations and numerical instabilities. Consequently, the initial path of the numerical force-displacement curve concerns the contact between laminate and cylinders and is not significant for the purpose.

Experimental response shows an increasing stiffness as the plate is bent. This hardening effect can be explained by taking into account that the considered material fails under compressive loads, as shown in Figure 4. The four-point bending tests are repeated until incipient failures occur. Consequently, cracks propagate in the upper layers subjected to compressive loads. When testing the composite plate, these cracks are progressively closed under compression. This allows to sustain loads in the failed layers and an increasing stiffness is thus obtained. The hardening effect can be also appreciated in the force-displacement curves with progressive damage of Figure 5 (dotted lines).

The limited discrepancy between experimental and numerical results highlights the accuracy of the  $DI_d$  technique in mapping the residual elastic properties of the damaged plate. Further, this result validates the proposed approach which accounts for the variable elastic modulus with a continuous polynomial curve in the finite element model.

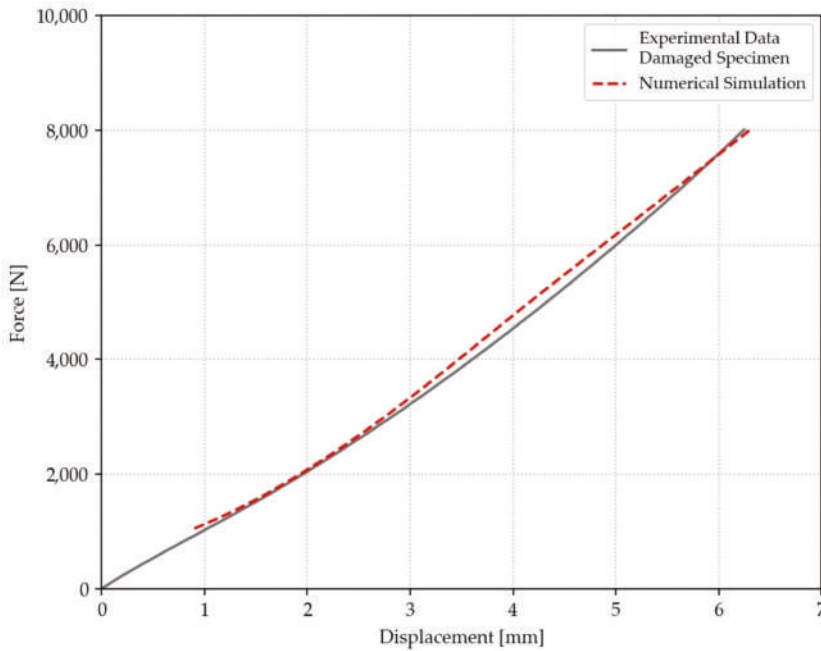


Figure 9. Comparison of experimental and numerical results of damaged specimen.

#### 4. Conclusions

The use of the  $DI_d$  technique in combination with the finite element method was presented. A four-point bending test was performed on an 8 layers twill fabric composite laminate until complete failure occurred. Experimental results were used to set up a finite element model of the composite plate subjected to bending test.

Then, repeated four-point bending tests allowed to progressively damage an undamaged plate of the same composite material. The  $DI_d$  technique was adopted to map the residual elastic properties on the damaged plate. Seven locations have been considered along the middle line of the composite laminate. In particular, damage was mainly localized in correspondence of the inner noses. Further, it has been found that elastic properties were assessed as an average of the circular unclamped region considered for the  $DI_d$  test, whose diameter is 76 mm. The diameter of the analyzed region may thus be reduced in order to achieve very local assessments.

A continuous polynomial curve was then considered to account for the variable elastic modulus in the finite element model. The resulting force-displacement curve of the numerical analysis was in very good agreement with experimental data of damaged plate.

Therefore, the  $DI_d$  methodology allows to locally assess the residual elastic properties of damaged composite materials. By mapping the elastic properties on the component and considering the assessed values in a finite element model, a precise description of the mechanical behavior of the composite plate is obtained.

Consequently, thanks to the proposed methodology, the health state of a damaged component can be quantitatively evaluated and decisions on its maintenance can be made by defining limits on the acceptable damage level.

**Author Contributions:** Conceptualization, G.B. and D.P.; Data curation, C.N. and A.T.; Funding acquisition, C.N., A.T. and R.C.; Investigation, C.N., A.T. and R.C.; Methodology, G.B. and D.P.; Project administration, G.B. and D.P.; Software, C.N.; Supervision, G.B. and D.P.; Validation, C.N. and A.T.; Visualization, C.N.; Writing—original draft, C.N.; Writing—review and editing, A.T., R.C., G.B. and D.P.

**Funding:** This research received no external funding.

**Conflicts of Interest:** The authors declare no conflict of interest.

## References

1. Heslehurst, R.B. *Defects and Damage in Composite Materials and Structures*; CRC Press: Boca Raton, FL, USA, 2017.
2. Ibrahim, M.E. Nondestructive testing and structural health monitoring of marine composite structures. In *Marine Applications of Advanced Fibre-Reinforced Composites*; Woodhead Publishing: Cambridge, UK, 2016; pp. 147–183.
3. Hubschen, G.; Altpeter, I.; Tschuncky, R.; Herrmann, H. *Materials Characterization Using Nondestructive Evaluation (NDE) Methods*; Woodhead Publishing: Cambridge, UK, 2016.
4. Katunin, A.; Danczak, M.; Kostka, P. Automated identification and classification of internal defect in composite structures using computed tomography and 3D wavelet analysis. *Arch. Civ. Mech. Eng.* **2015**, *15*, 436–448. [[CrossRef](#)]
5. Junyan, L.; Liqiang, L.; Yang, W. Experimental study on active infrared thermography as a NDI tool for carbon-carbon composites. *Compos. Part B Eng.* **2013**, *45*, 47–138. [[CrossRef](#)]
6. Tam, J.H.; Ong, Z.C.; Ismail, Z.; Ang, B.C.; Khoo, S.Y. Identification of material properties of composites materials using nondestructive vibrational evaluation approaches: A review. *Mech. Adv. Mater. Struct.* **2017**, *24*, 971–986. [[CrossRef](#)]
7. ASTM. *E1876-15 Standard Test Method for Dynamic Young's Modulus, Shear Modulus, and Poisson's Ratio by Impulse Excitation of Vibration*; ASTM International: West Conshohocken, PA, USA, 2015.
8. ASTM. *C1259-15 Standard Test Method for Dynamic Young's Modulus, Shear Modulus, and Poisson's Ratio for Advanced Ceramics by Impulse Excitation of Vibration*; ASTM International: West Conshohocken, PA, USA, 2015.
9. Paolino, D.S.; Geng, H.; Scattina, A.; Tridello, A.; Cavatorta, M.P.; Belingardi, G. Damaged composites laminates: Assessment of residual Young's modulus through the Impulse Excitation Technique. *Compos. Part B Eng.* **2017**, *128*, 76–82. [[CrossRef](#)]
10. Garnier, C.; Pastor, M.L.; Eyma, F.; Lorrain, B. The detection of aeronautical defects in situ on composite structures using Non-Destructive Testing. *Compos. Struct.* **2011**, *93*, 36–1328. [[CrossRef](#)]
11. Belingardi, G.; Cavatorta, M.P.; Paolino, D.S. A new damage index to monitor the range of the penetration process in thick laminates. *Compos. Sci. Technol.* **2008**, *68*, 2646–2652. [[CrossRef](#)]
12. Belingardi, G.; Cavatorta, M.P.; Paolino, D.S. Repeated impact response of hand layup and vacuum infusion thick glass reinforced laminates. *Int. J. Impact Eng.* **2008**, *35*, 609–619. [[CrossRef](#)]
13. Belingardi, G.; Cavatorta, M.P.; Paolino, D.S. On the rate of growth and extent of the steady damage accumulation phase in repeated impact tests. *Compos. Sci. Technol.* **2009**, *69*, 1693–1698. [[CrossRef](#)]
14. Belingardi, G.; Cavatorta, M.P.; Paolino, D.S. Single and repeated impact tests on fiber composite laminates: Damage index vs. residual flexural properties. In Proceedings of the 17th International Conference for Composite Materials, Edinburgh, UK, 27–31 July 2009.
15. Tridello, A.; D'Andrea, A.; Paolino, D.S.; Belingardi, G. A novel methodology for the assessment of the residual elastic properties in damaged composite components. *Compos. Struct.* **2017**, *161*, 435–440. [[CrossRef](#)]
16. Yam, L.H.; Wei, Z.; Cheng, L. Nondestructive detection of internal delamination by vibration-based method for composite plates. *J. Compos. Mater.* **2004**, *38*, 98–2183. [[CrossRef](#)]
17. LSTC. LS-DYNA Keyword Manual Volume I. 2019.
18. LSTC. LS-DYNA Keyword Manual Volume II. 2019.
19. Muflahi, S.A.; Mohamed, G.; Hallett, S.R. Investigation of delamination modeling capabilities for thin composite structures in LS-DYNA. In Proceedings of the 13th International LS-DYNA Users Conference, Detroit, MI, USA, 8–10 June 2014.

20. Williams, K.V.; Vaziri, R.; Floyd, A.M.; Poursatip, A. Simulation of damage progression in laminated composite plates using LS-DYNA. In Proceedings of the 5th International LS-DYNA Users Conference, Southfield, Dearborn, MI, USA, 9–11 April 1998.
21. Moncayo, E.D.; Wagner, H.; Dreschler, K. Benchmarks for composite delamination using LS-DYNA 971: Low velocity impact. In Proceedings of the German LS-DYNA Forum, Frankenthal, Germany, 11–12 October 2007.
22. ASTM. D6272–17. *Standard Test Method for Flexural Properties of Unreinforced and Reinforced Plastics and Electrical Insulating Materials by Four-Point Bending*; ASTM International: West Conshohocken, PA, USA, 2017.
23. ASTM. D5628-10. *Standard Test Method for Impact Resistance of Flat, Rigid Plastic Specimens by Means of a Falling Dart (Tup or Falling Mass)*; ASTM International: West Conshohocken, PA, USA, 2010.
24. LSTC. LS-DYNA Theory Manual. 2019.



© 2019 by the authors. Licensee MDPI, Basel, Switzerland. This article is an open access article distributed under the terms and conditions of the Creative Commons Attribution (CC BY) license (<http://creativecommons.org/licenses/by/4.0/>).

Review

# A Review of Non-Destructive Damage Detection Methods for Steel Wire Ropes

Ping Zhou <sup>1</sup>, Gongbo Zhou <sup>1,\*</sup>, Zhencai Zhu <sup>1</sup>, Zhenzhi He <sup>2</sup>, Xin Ding <sup>1</sup> and Chaoquan Tang <sup>1</sup>

<sup>1</sup> Jiangsu Key Laboratory of Mine Mechanical and Electrical Equipment, School of Mechatronic Engineering, China University of Mining and Technology, Xuzhou 221116, China

<sup>2</sup> School of Mechanical and Electrical Engineering, Jiangsu Normal University, Xuzhou 221116, China

\* Correspondence: gzbzhou@cumt.edu.cn; Tel.: +86-182-0520-7100

Received: 22 May 2019; Accepted: 5 July 2019; Published: 9 July 2019

**Abstract:** As an important load-bearing component, steel wire ropes (WRs) are widely used in complex systems such as mine hoists, cranes, ropeways, elevators, oil rigs, and cable-stayed bridges. Non-destructive damage detection for WRs is an important way to assess damage states to guarantee WR's reliability and safety. With intelligent sensors, signal processing, and pattern recognition technology developing rapidly, this field has made great progress. However, there is a lack of a systematic review on technologies or methods introduced and employed, as well as research summaries and prospects in recent years. In order to bridge this gap, and to promote the development of non-destructive detection technology for WRs, we present an overview of non-destructive damage detection research of WRs and discuss the core issues on this topic in this paper. First, the WRs' damage type is introduced, and its causes are explained. Then, we summarize several main non-destructive detection methods for WRs, including electromagnetic detection method, optical detection method, ultrasonic guided wave detection method, and acoustic emission detection method. Finally, a prospect is put forward. Based on the review of papers, we provide insight about the future of the non-destructive damage detection methods for steel WRs to a certain extent.

**Keywords:** non-destructive damage detection; steel wire ropes; review; electromagnetic detection; optical detection; ultrasonic guided wave

## 1. Introduction

Steel wire rope was invented in 1834. It has many advantages, such as high tensile strength, stable and reliable operation, and a strong capacity for dynamic load and overload. It is widely used in lifting, transportation, and traction equipment/systems. The main equipment/systems include mine hoists, ropeways, cranes, oil rigs, elevators, and cable-stayed bridges [1–4]. During the service of steel wire ropes (WRs), defects and damages like wire breakage, wear, rust, fatigue, strand breakage, and even sudden breaking will inevitably occur due to various reasons. Therefore, academia and industry have been trying to explore various methods to detect damages of WRs to guarantee its reliability and safety [5].

However, due to the complexity of WR structure, the diversity of working environment, and the limitation of detection methods, non-destructive detection of WRs has become an old and difficult problem [5]. The development of related technologies is slow, and it is difficult to achieve efficient and reliable industrial application. At present, manual inspection under low-speed operation (visual inspection combined with manual touch) is still the main method in most cases, and the electromagnetic detectors are used in a few cases, which cause problems such as missed detection, false detection, and failure to detect in time, resulting in frequent occurrence of faults and accidents [6]. Taking the mining industry as an example, on 29 December 2010, a wire rope at a resort in Maine broke and more than 200 people in the cable car were trapped in the air and 9 people were injured; On 9 March 2017,

a wire rope of a multi-rope friction mine hoist of the Mining Company of Heilongjiang Longmei Group suddenly broke during the lifting process causing a cage fall (cable fire aggravates wire rope breakage). As a result, 17 people trapped in the cage were killed. Therefore, it is of great significance to study reliable and efficient non-destructive detection methods for WRs.

There are many methods for WRs damage detection [7], including electromagnetic detection, optical detection, ultrasonic guided wave detection, acoustic emission detection, ray detection, eddy current detection, and vibration detection. The most important methods are electromagnetic detection and optical detection (machine vision method). In particular, the instruments based on electromagnetic detection have been gradually applied in the market. Although the optical detection method can intuitively grasp the surface morphology characteristics of WRs, it is seldom used because of the influence of algorithm performance and the inability to detect internal defects. In addition, other methods are still in the theoretical and laboratory stage for many reasons. Non-destructive detection of WRs is an important research field, and there are some literature reports on various methods. However, there is still a lack of a reasonable and systematic summary to illustrate the current research situation and point out the possible research directions in the future.

Based on this, we first summarize the research status of each important detection method and analyze its shortcomings, then we summarize the existing methods and put forward the prospects. To our best knowledge, this article will make up for the lack of literature review in the field of non-destructive detection of WRs, which can bridge this gap and promote the development of non-destructive detection technology of WRs. The contributions of this paper can be summarized as follows: (1) The literatures in the field of non-destructive testing of wire rope are summarized in detail, including electromagnetic detection method, optical detection method, ultrasonic guided wave method, and acoustic emission method. (2) Shortcomings of these methods are pointed out, and comparisons are made among them. (3) Each important detection method is prospected in combination with the current technological situation, which is expected to promote the development of this direction.

The work is arranged as follows: In Section 2 the WRs damage type is introduced and its causes are explained. In Section 3 several main WRs non-destructive detection methods are reviewed. Their main disadvantages are summarized in Section 4. The prospect is presented in Section 5.

## 2. Damage Types of Wire Ropes

Steel wire ropes will be damaged in various forms when used, which will reduce the strength of the WRs and pose a potential threat to the system safety. Various damage conditions and distribution have different effects on the strength reduction of WRs, and the whole WR is often scrapped due to a certain section of the WR. Therefore, the study of various damages of WRs will be beneficial to the correct evaluation of its state [8,9]. The damage types of WRs include wire breakage, wear, deformation, rust, and fatigue. Among them, fatigue has a variety of representations, such as internal and external cracks, internal and external wire breakages, and slack. The common types are shown in Figure 1.

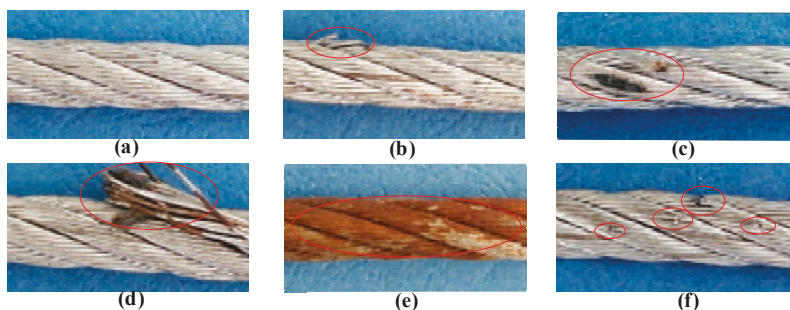


**Figure 1.** Sample pictures of wire rope damage. (a) Health; (b) wire breakage; (c) wear; (d) deformation (broken strand); (e) rust; and (f) fatigue (fatigue breaking).

In practice, the above damage types will interact with each other, such as rust will aggravate the wear process, wear will promote wire breakage, fatigue will promote the generation or aggravate the evolution of wire breakage and wear, and the comprehensive impact of wear, wire breakage, fatigue, and rust will promote broken strands and aggravate the scrap of wire rope. When minor faults evolve to a certain extent or suffer sudden impact load, strand breakage will occur, which will obviously affect the life of WR. Because of the different working conditions and environment, the development speed and degree of damages are also different. In current standards, the residual strength is generally obtained by finding the defects of WR in service to infer the strength loss, then, whether the WR is scrapped is judged according to the safety factor of WR and the rules of use [9].

The description of different damage types of WRs is shown in Table 1.

**Table 1.** Types and description of wire rope (WR) damage.

| Types         | Description  |
|---------------|--|
| Wire breakage | Fatigue breakage and wear breakage are the main causes of wire breakage. Wire breakage will reduce the WR strength and increase the potential safety hazards of WRs.                 |
| Wear          | Wear is one of the most common phenomena of WR, which usually evolves from normal wear to failure wear. The wire wear will reduce the tension it can bear.                           |
| Rust          | Rust is a fault phenomenon of WRs caused by the chemical and electrochemical action of surrounding medium, which has a significant impact on the life of WRs.                        |
| Deformation   | Impact on the WR causes damages (including flattening, strand relaxation, kinking, bending, and strand breakage) to the original structure, which accelerates the scrap.             |
| Fatigue       | After repeated bending for a certain number of times or repeated stretching and twisting, fatigue occurs, which leads to changes in the internal and external performance of the WR. |

In general, in the WR damage detection and diagnosis practice, according to the characteristics of WR damages, the WR damages can be divided into two categories [10]: local flaw damage type (LF) and loss of metallic cross-sectional area type (LMA). LF type refers to the damage locally generated in the WR, mainly including internal and external breakage, corrosion pit, and deep wear of steel wire, characterized by a sudden decrease in the metallic cross-sectional area of the WR; LMA type refers to the slow reduction of the effective metallic cross-sectional area in the long range along the axial direction of the WR, which mainly includes wear, long-distance rust, and rope diameter reduction.

### 3. Non-Destructive Detection Method for Steel Wire Ropes

The following is a literature review of electromagnetic detection, optical detection, ultrasonic guided wave, acoustic emission detection method, and other detection methods.

#### 3.1. Electromagnetic Detection Method

Electromagnetic detection is one of the oldest methods in non-destructive testing field and has been applied earliest to WRs detection. In this detection method, there are two different excitation modes including coil excitation and permanent magnet excitation, and the commonly used sensor types are the Hall sensor and the induction coil.

The detection principle diagram is shown in Figure 2, the main principle is: after the WR is excited by coil or permanent magnet, the surface and internal damages will change the magnetic flux in the WR. Then the signal is detected by the induction coil or integrated sensor (e.g., Hall sensor and magnetoresistance sensor), and the type or degree of damages can be obtained to a certain extent through further processing and analysis of the signal [8–10]. Figure 2a is the main magnetic flux detection method based on coil excitation, which adopts the coaxial magnetization method, namely, taking the measured wire rope as the core, and the wire rope segment between the two coils is magnetized by the coil with current. Figure 2b is the main magnetic flux detection method based on permanent magnet excitation, in which the method of inter-pole magnetization is adopted, taking the wire rope as a component of the magnetic circuit, and the induction coil is used to detect the change of magnetic flux inside the wire rope caused by damage. Figure 2c is a method of return magnetic flux detection based on permanent magnet excitation, whose excitation mode is the same as Figure 2b, but the Hall sensor is used to detect the flux density in the magnetic circuit formed by excitation device, air gap and wire rope. Figure 2d is leakage magnetic flux detection method based on permanent magnet excitation, whose excitation mode is the same as Figure 2b,c, however, the difference is that the sensor is used to collect the leakage magnetic field information caused by the damage.

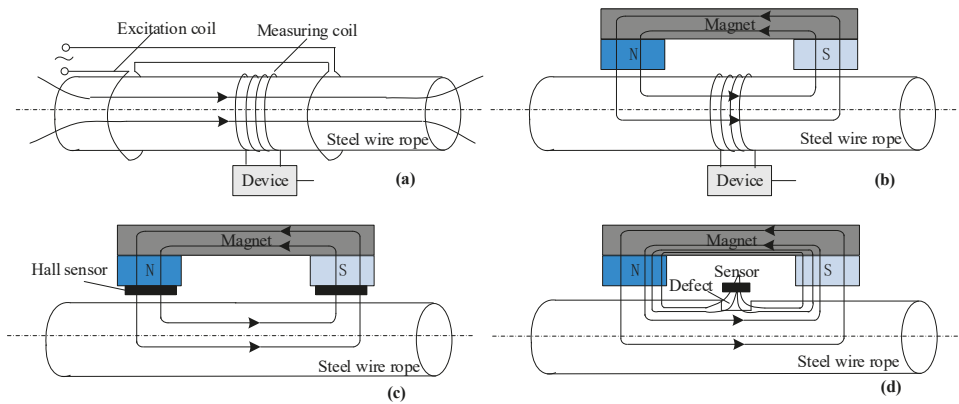


**Figure 2.** Electromagnetic non-destructive detection principle of steel wire rope. (a) Main magnetic flux detection method based on coil excitation; (b) main magnetic flux detection method based on permanent magnet excitation; (c) return magnetic flux detection method based on permanent magnet excitation; and (d) leakage magnetic flux detection method based on permanent magnet excitation.

In 1906, South Africa developed the first non-destructive testing device for WRs based on electromagnetic principle. Over the past 100 years, electromagnetic detection technology has made great progress [11]. The research of electromagnetic detection technology mainly includes: the mechanism of electromagnetic detection signal under the influence of defect parameters (defect width, depth, number of broken wires, etc.) or the theoretical model of the relationship among them; the magnetization

method and device of WRs; the electromagnetic signal detection means such as the coil sensor, Hall sensor, and magnetoresistance sensor. It is noted that the signal processing and recognition methods are accompanied with the above three aspects. Following is a literature review of the above three aspects.

### 3.1.1. Mechanism and Model

For electromagnetic detection mechanism and theoretical model, many studies have been carried out by researchers at home and abroad.

For instance, Norouzi et al. [12] used the finite element analysis method to optimize the pole shoe length, and the optimized results help make the magnetic flux distribution in the measured parts as uniform as possible, which was more conducive to magnetic leakage detection. In [13], Zhao et al. performed finite element analysis for the magnetic flux leakage (MFL) distribution of WR typical defects based on strong magnetic detection method and obtained the relationship between MLF signal and detection distance, damage depth, damage axle width and internal wire breakage. In [14], Lenard et al. paid attention to oil and gas pipelines, and analyzed the influence of line pressure, bending and residual stresses on MFL signal in MFL detection process through experiment and finite element simulation. To study the effects of probes and probe lift-off on the defect leakage magnetic field, Krzywosz [15] and Kalwa et al. [16] respectively carried out research and proposed that the smaller the lift-off value of magnetic sensitive probes, the better.

In order to apply the magnetic dipole to the three-dimensional magnetic field modeling of MFL, Dutta et al. [17] first presented a three-dimensional (3D) magnetic leakage model of ferromagnetic materials surface fracture based on magnetic charge theory. Based on [17], an improved 3D MFL model for numerical analysis is proposed by Trevino et al. [18], which can be used to detect surface fracture of ferromagnetic materials under saturated magnetization. To further explain the formation principle of MFL, Sun et al. [19] explained the mechanism of MFL in engineering from the perspective of magnetic refraction, and found that the signal component in defect detection was different from that in traditional MFL analysis, which was produced by protruding defects. Considering the effect of tensile stress on the strength of the MLF of a steel WR defect, Gao et al. [20] loaded a variable force onto reproduced samples of typical defective WRs relying on an inspection platform. The experimental results showed that the peak-to-peak values of the MFL signal from all defective WRs increased with tensile stress, in an approximately linear relationship.

### 3.1.2. Magnetization Method

The magnetizer is an important component of WR non-destructive detection system. Its excitation structure and mode will produce different magnetization effects [21]. The commonly-used magnetization methods mainly include the coil electromagnetic magnetization method and permanent magnetization method.

Thus far, Kang et al. [22] analyzed the different WR magnetization effect of different magnetization methods by finite element method and obtained the optimum size of feed-through magnetizer. In [23], the equipment was operated according to the principle of strong magnetic detection, which realized magnetization saturation by magnetizing the wires with a pre-magnetic head. Jomdecha et al. [24] improved the traditional current excitation device, so that the excitation intensity of the device can be controlled by adjusting the excitation power supply and the coil. Wang et al. [25] designed an excitation device that can restrain the fluctuation of lift-off distance and can improve the structure of the detection device. Song et al. [26] studied whether AC magnetization in U-yoke would cause eddy current disturbance field. The results showed that the axial component of MFL of crack was independent of excitation frequency and intensity.

In the practical application, for thin WR in strong electromagnetic interference environment, Yan et al. [27] proposed an electromagnetic non-destructive testing method. In this method, a simplified magnetic circuit was proposed to excite WR, and the defect detection of thin WR in electromagnetic

interference environment was realized. A new WR tester was established based on MLF principle in [28], and each arc segment subtends an angle of 22.5 degrees at the center by cutting two rings of NdFeB along axial direction into 32 equal arc segments, which were then parallelly magnetized in magnetizer. To detect WR damage in coal mine, Sun et al. [29] proposed an opening electric magnetizer through the magnetic control for a C-like electric loop-coil, which has an opening structure capable of directly encompassing and centering the endless object in it. The magnetizer can solve problems, i.e., installation inconvenience and on-line detection difficulty in the non-destructive testing of coal mine wire rope fixed at both ends.

### 3.1.3. Detection Sensor

#### (1) Coil sensor

Coil sensor is widely used because of its low cost and ease of use. In recent years, its application in WRs non-destructive detection is still further studied.

For example, Liu et al. [30] assessed the surface and internal flaws using a new type of sensor to measure the biased pulse magnetic response in a large-diameter steel stay cable. Two parallel connected flexible flat coils fed with a biased pulse current were deployed by the sensor as the electromagnet for cable magnetization. Yan et al. [31] put forward a kind of iron core as coil winding skeleton for the wire rope non-destructive testing relying on the theoretical analysis and 3D transient magnetic field simulation. The experiment results proved that the signal to noise ratio of coil with the iron core proposed in this paper increased almost six times, making it easier for defect analysis. Aiming at detecting the change of surface leakage magnetic field, Fedorko et al. [32] designed a pair of induction coils of different sizes and analyzed the static magnetic field distribution based on finite element simulation. Sun et al. [33] designed a new MLF sensor based on open magnetizing method. Experimental comparisons between the open and yoke probes for on-line automated monitoring were conducted, which confirmed the characters of smaller magnetic interaction force, less wear, and damage in this method were in contrast to the traditional on-line automated structural health monitoring technology.

#### (2) Integrated sensor

Through using integrated sensors to detect MLF of the WR surface, the circumferential and axial locations of defects can be founded, so as to analyze whether the defects belong to centralized or decentralized wire breakage, and to make a further accurate judgment on the damage of WRs [11].

In the work of [34–38], the Hall sensors were used. Xu et al. [34] designed a sensor module based on Hall sensor to test the leakage magnetic field of stay cables online and compared three different filtering algorithms to obtain the leakage magnetic field of artificial damage inside the cable. Wang et al. [35] proposed a new method to detect magnetic excitation in WRs by combining the structural models for dynamic magnetic field balancing and magnetic focusing. A Hall-element array and the magnetic focusing technique were used to reduce the interference produced by the interactions between the environmental magnetic fields and the wire rope strand. A MLF method is adopted by Kim et al. [36] for the detection of local damage when inspecting WRs, and a multi-channel MFL sensor head was fabricated by adapting to the wire rope with a Hall sensor array and magnetic yokes, the accuracy and reliability were evaluated based on the comparison of the repeatedly estimated damage size and the actual damage size. Tian et al. [37] designed an optimal model for magnetic excitation to develop a non-destructive sensor using a Hall-effect sensor for coal mine hoist wire ropes. Then, a new detection method called the permanent magnet co-directional excitation flux-weakening method was put forward in [38]. The emulation and experimental results revealed that the defect detection sensor proposed in the paper can improve the magnetic signal from the defect by six to eight times.

In addition, the magnetoresistance sensors were used in the work of [39,40]. Singh et al. [39] proposed giant magnetoresistive-based MLF technique for condition monitoring of 64 mm-diameter steel track rope which can be used to transport coal. Two saddle coils were used to magnetize the rope

in this technique, and a giant magnetoresistive sensor was able to detect the tangential component of leakage magnetic flux from flaws. In addition, the technique can detect 2 mm-deep flaws with good signal-to-noise ratio and solve the flaw whose interval is more than 3.2 mm. Tunnel magnetoresistive (TMR) devices was first employed to form a circular MLF sensor by Liu [40], aiming to detect slight WR flaw. Two versions of this tailor-made circular TMR-based sensor array were put forward to inspect WRs with the diameters of 14 mm and 40 mm, respectively.

### 3.2. Optical Detection Method

Optical detection method is an efficient non-destructive detection method, which has been developed in the field of WR surface damage detection. It can intuitively grasp the damage situation of WR surface. At the same time, with the development of WR oil pollution removal method/device [41], the influence of oil pollution gradually decreases.

The principle of optical detection method is shown in Figure 3, which generally includes two parts: image acquisition and damage diagnosis. The image acquisition generally uses high-speed camera to collect the surface image of WRs, and the damage diagnosis includes image preprocessing and pattern recognition. WR damage detection based on pattern recognition is a potential research direction. Specifically, the hardware and software of the image acquisition system are configured according to the actual situation; the collected images are first processed by pretreatment method like cutting or filtering. Then, feature extraction methods (such as local binary pattern and gray level co-occurrence matrix) are used to extract features, and next dimensionality reduction is carried out on the established feature datasets. Finally, machine learning classifiers (such as support vector machines, artificial neural networks, etc.) are used for training and testing to obtain robust classifiers for state recognition of unknown images [42].

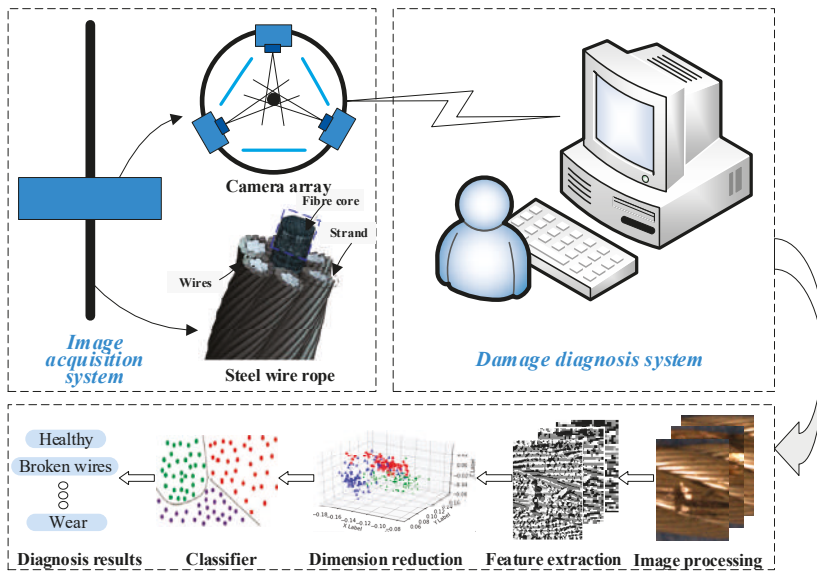


Figure 3. Optical detection principle for steel wire rope.

Based on camera and offline processing algorithm, Vallan et al. [43] established a measurement system which measured the change of rope length according to the characteristics of rope twist to detect the damage of rope. For elevator rope, Yaman et al. [44] proposed a fault monitoring method based on image processing and autocorrelation analysis, which realized the defect detection of steel

rope to a certain extent. In [45], Sun et al. realized the identification and segmentation of WRs boundaries through image processing and clustering methods. Platzer et al. [46] proposed using Hidden Markov field model to locate the defects of WR, the results demonstrated that the detection performance of this method is better than that of the previous time invariant system classification method. Then, they compared the performance of different texture features in the detection of WR surface defects in [47]. For the defects of WR, the histogram of oriented gradient feature was the best, followed by the local binary patterns feature. In the work of [48,49], Wacker et al. established a probabilistic appearance model as a representation of normal surface changes combined with the structure and appearance of the WR and realized the detection of WR abnormal surface. For surface defects of thin metallic wires, an automatic optical detection technique was presented by Sanchez-Brea et al. in [50]. This technique was based on the intensity variations on the scattered cone generated when the wire is illuminated with a beam at oblique incidence.

### 3.3. Ultrasound Guided Wave Method

Ultrasonic guided waves method (UGW) is one of the promising methods for investigation of non-homogeneities for the internal structure of WRs [51]. The measurement schematic diagram is illustrated in Figure 4, which is consisted of the computer, the ultrasonic measurement system, the preamplifier, the transmitter, and the receiver, detailed principles are available for reference [52]. The wave is launched on WRs and propagates along the strand of WRs. Acoustic reflection occurs when the sound wave passes through the damage. After collecting and analyzing the echo at the receiving end, the damage inside and outside the WR can be obtained [53].

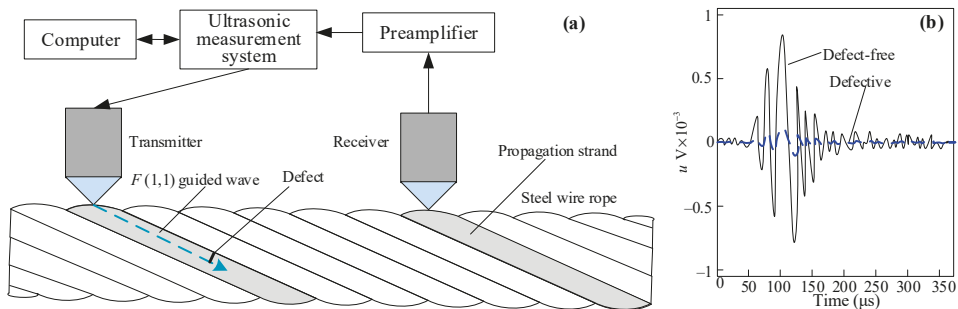


**Figure 4.** Non-destructive testing principle of steel wire rope by ultrasonic guided wave method [52]. (a) Detection system schematic diagram; (b) sketch map for waveforms of defect-free and defective signal.

For purpose of the generation and reception of ultrasonic longitudinal guided waves in seven-wire steel strands in a pitch catch arrangement, Liu et al. [53] optimized the magnetostrictive transducers configuration for both transmitter and receiver. Consequently, magnetostrictive transducers with an optimized configuration, including permanent magnet distribution and multilayer coil connection, could be efficiently used for the inspection of seven-wire steel strands by using UGW in a pitch catch arrangement. In [54], Treysse et al. studied the transmission characteristics of elastic guided wave in multi-stranded WR. The dispersion curve of spiral WR was obtained by semi-analytical finite element method and signal energy calculation, and the optimum excitation and receiving position of ultrasonic guided wave was calculated. Vanniamparambil et al. combined UGW, acoustic emission technology and digital image correlation, and fused the features obtained by the three technologies to achieve non-destructive testing [55]. Xu et al. [56] studied the effect of different frequencies of UGW on the detection rate of steel WR defects. It was found that the higher frequency of guided waves in the steel WR lead to the faster energy attenuation, and the receiving length of elastic waves increased with the frequency. The propagation characteristics of various UGW between strands and

cores of WR and their effects on the penetration depth of WR were studied in [57] by Raisutis et al. In the work of [58], the efficiency of employing the magnetostriction of ferromagnetic materials were studied relying on the UGW method for WRs damage inspection, and the location and severity of damages were approximately identified and characterized using the short-time Fourier transform and wavelet analysis.

### 3.4. Acoustic Emission Detection Method

Acoustic emission (AE) refers to the transient elastic wave phenomena produced by the rapid release of energy in the local area of the material under the influence of the outside world [59]. Acoustic emission sensors can convert transient elastic waves into electrical signals based on piezoelectric effect. The change of internal damage can be inferred from the analysis of electrical signals [60]. The AE testing system is shown in Figure 5a (in practical application, specific device structure and detection method should be designed according to specific detection objects) [61]. The testing principle are as follows: the two ends of the WR specimen are installed on the tensile test bench, and two clamps are clamped in the middle of the WR to help install two acoustic emission sensors. The loading parameters of the test bench are controlled by a load controller. Acoustic emission equipment is used to collect and analyze the collected data in the process of loading to obtain the occurrence and location of defects on the WR. The waveform of broken wire is shown in Figure 5b. AE technology can qualitatively identify the broken wire signal, which has the characteristics of high amplitude and high absolute energy [62]. However, because this method can only be used in the static load part, the signal-to-noise ratio is low, the cost of the instrument is high, and it is difficult to measure dynamically, it is still in the laboratory stage at present, and is difficult to be effectively used in engineering.

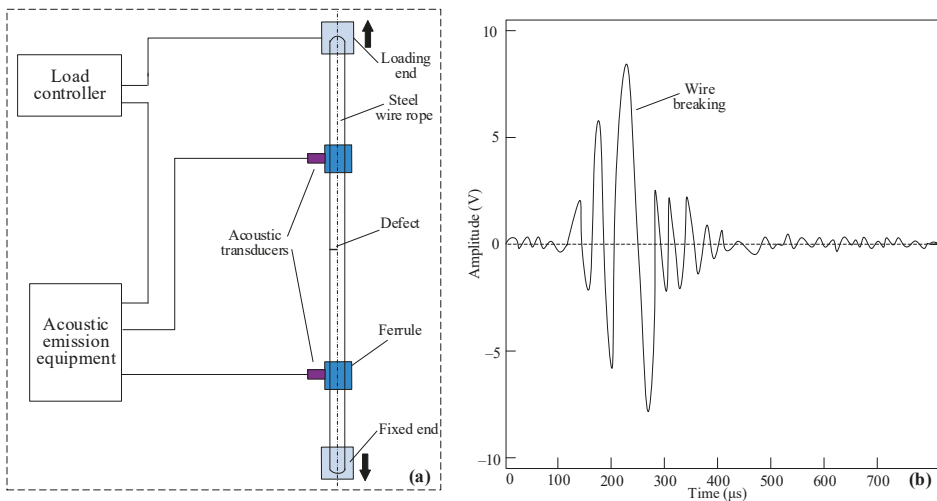


**Figure 5.** Acoustic emission detection for steel wire rope [61]. (a) Detection system schematic diagram; (b) sketch map for waveform of defects and wire breaking signal.

The research of relevant experimental methods and principles is active. The most systematic research on detecting broken wire of WR by AE technology was carried out by Casey et al. [63–67] in the 1980s. Based on a large number of experiments, they put forward an analysis method of amplitude distribution, that is, using the amplitude of AE signal to judge wire breakage. Due to the limitation of instrument level at that time, the result was not very ideal. Casey et al. [68] summarized the research of AE technology in the defect monitoring of WR at first, pointed out that the most important

application of AE technology in the WR monitoring is the detection and location of broken wires, and discussed in detail the influence of the WR structure, the size and the number of broken wires on the AE monitoring results. Subsequently, with the development of technology, this method has been further studied. AE technology was adopted to quantitatively detect wire breakage in WR by Shao et al. [69]. The appropriate timing parameters were determined by waveform analysis, and the broken wire event was characterized as a single AE impact signal, which realized the quantitative expression of broken wire. For the problem of that inter wire fretting in ropes could cause excessive low amplitude noise, a new method based on modern signal processing techniques proposed by Ding et al. [70] could be applied to solve it. Drummond et al. [61] monitored the fatigue process of wire ropes by AE and established the relationship between the AE signal characteristics and wire breaks. Bai et al. [62] used AE technique to monitor the tensile testing process for two kinds of elevator wire ropes, and in this work AE signals from wire breaks were obtained and analyzed by AE parameters and waveforms. In the work of [71], Li et al. proposed an innovative monitoring method that used waveguides to draw out the steel wires at the end of the cable, which can effectively capture the AE signal produced by defects/wire breaking and accurately locate the transverse position of the wire breaking of the cable. Li et al. [72] developed a damage assessment and warning method for stay cables based on the AE technique and fractal theory. In this work, the fatigue test of composite cable was conducted, the fractal dimension of AE signal was analyzed, the damage index according to the fractal dimension was established.

### 3.5. Other Detection Methods

Only a few literature reports involve other non-destructive detection methods of WRs, such as eddy current detection [73,74] and ray detection [75,76], and are in the laboratory stage for many reasons. The detection principles are depicted in Figure 6. Figure 6a represents the eddy current method and Figure 6b explains the ray method.

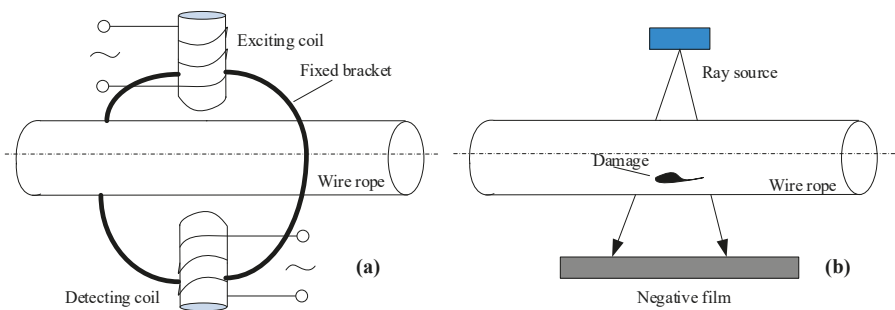


**Figure 6.** The other detection method principles. (a) Eddy current method [74]; (b) ray method [75].

Eddy current non-destructive testing technology takes eddy current effect produced by metal conductor in alternating magnetic field as its working principle. It has the advantages of high sensitivity, fast detection speed, non-contact, etc. [73]. Using low frequency transmission eddy current testing method, Cao et al. [73] designed an adjustable annular eddy current testing device with symmetrical probe arrangement along the radial direction to perform the quantitative detection analysis of WR breakage defects. Meanwhile, Cao et al. [74] developed an experimental eddy current sensor and computer measuring system to obtain characteristic data for rope samples made in laboratory. The characteristic data are identified by the RBF network, and the identification results show the proposed evaluation method is feasible.

When non-destructive testing of WR is carried out by ray method, the damage situation inside and outside of the WR can be clearly presented on the negative film because of the different absorption ability of radiation rays between the surface/internal defect and non-defect of the WR [75,76]. For this reason,

Zhang et al. [75] proposed a new WR detection system based on X-ray digital imaging technology, and introduced the X-ray digital imaging technology, system structure and working principle. A detection system of bridge cables using gamma ray is proposed by Peng et al. [76]. The exposure time and sensitivity of steel cables in gamma ray detection were studied. Meanwhile, the comparison between the ray detection method and the electromagnetic detection method was performed. The actual measurement demonstrated that the research results can improve the safety of WR and ensure the bridge safety assessment.

#### 4. Existing Shortcomings

In summary, we find that each non-destructive detection method of WRs has its own advantages, but there are still many shortcomings [9,77,78], as shown in Table 2.

**Table 2.** Comparison of several wire rope detection methods.

| Methods                                 | Measurement Principle  | Presentation Way             | Advantages   | Main Disadvantages   |
|---|--|------------------------------|--|--|
| Artificial visual method                | Inspect the WR surface at a slow speed                                     | Direct analysis and judgment | Simple and direct judgment of surface damage                             | Time-consuming, and the result is affected by oil pollution and man-made factors   |
| Electromagnetic detection method [7–40] | Measure leakage magnetic flux  | Graph line                   | Qualitative determination of wire breakage, rust, wear and other defects | Difficult to make quantitative measurement and distinguish defects exist at the same time  |
|   | Measure main magnetic flux   | Graph line                   | Measure the change of WR metal cross section area                        | Not suitable for detecting broken wire, especially when the fracture is not obvious  |
| Optical detection method [42–50]        | Detect WR surface using camera   | Image                        | Intuitive, and high accuracy of detection                                | Influenced by environmental factors, data size and machine learning algorithm performance  |
| Ultrasound guided wave method [51–58]   | Ultrasound propagates in the medium  | Echogram                     | Detect wire breakage, long distance of single detection                  | Weak anti-noise ability, cannot reflect the condition of WR in detail  |
| Acoustic emission method [61–72]        | Measure the ultrasound emitted by the structural change of steel wire rope | Sound transmission analysis  | Detect wire breakage and deformation                                     | Can only be used in the static load part, has low signal-to-noise ratio, high instrument cost and is difficult to measure dynamically. |
| Eddy current method [73,74]             | Eddy current effect  | Graph line                   | Detect wire breakage and rust  | Skin effect affects wire breakage detection, and the signal-to-noise ratio is low  |
| Ray method [75,76]                      | Radiation vertical to the rope with strong X-ray/gamma-ray                 | Image                        | Determine wire breakage  | Instruments and radiation protection devices are expensive and cannot be continuously measured for long exposure periods               |

In view of the problems existing in electromagnetic detection, optical detection, ultrasonic guided wave method, acoustic emission method, and other detection methods, the following are specified in detail:

- (1) In the field of WR electromagnetic detection, the existing theory and technology have developed in depth. However, according to the current research situation, the problems in the electromagnetic non-destructive detection of WR mainly include the influence of different WR structures on the detection signal, the quantitative analysis of LF type defects, the formulation of testing standards, and the relationship between LMA, LF defects and the strength of WRs (details can be found in reference [78]). Only by solving the quantitative detection of LF type defects and the relationship between defects and the strength of WRs, can the service life of WRs be truly and accurately predicted by non-destructive testing.
- (2) In the field of WR optical detection, the existing research has a small amount of data, namely no big data sets, and the algorithm is with shallow structure. It has some problems such as limited

excavation ability, low computational efficiency and poor robustness. It is difficult to carry out high-speed detection, high efficiency and reliable identification, therefore can not be directly applied to real-time state health monitoring of WR. By introducing the deep learning [79–82] method into the WRs damage detection/monitoring, it is expected to achieve real-time, reliable and accurate damage identification and location, thus realizing the detection and monitoring of WR surface damage [83].

- (3) The ultrasonic guided wave method, acoustic emission method and other detection methods are still in the stage of theoretical research and laboratory, and there is still a certain distance away from practical application, due to the limitation of technical level and the method itself. UGW and AE method are difficult to be used in actual dynamic detection, and the signal-to-noise ratio needs to be further improved; Eddy current method is less studied and affected by skin effect. Its reliability needs further study; Ray Method's development prospects are relatively limited compared with other methods because of the expensive instruments and the potential impact of radiation on the human body. Only by further deepening theoretical and experimental research and solving more of the above difficult problems can we promote the progress of these detection methods.

## 5. Summaries and Prospects

To promote the development of non-destructive detection method for WRs, we present an overview of non-destructive damage detection methods for WRs in this paper. Some summaries are listed as follows:

- (1) The types of WR damages and their causes were introduced in detail, including wire breakage, wear, rust, deformation, and fatigue. They are divided into two types: local flaw and loss of metallic cross-sectional area.
- (2) The development status of several important detection methods including electromagnetic detection, optical detection, ultrasonic guided wave method, acoustic emission detection, eddy current detection, and ray detection was reviewed, and their advantages and disadvantages were compared and summarized. On the whole, electromagnetic detection method has gradually been applied in practice. Optical method has shown great potential for application, while other methods are still in the laboratory stage.

In addition, some research trends and potential future research directions are given as follows:

- (1) Electromagnetic detection method: the influence of WR structure on electromagnetic signal is expected to be studied; to solve the quantitative detection of LF type defect, the relationship between LF type defect and electromagnetic signal characteristics should be further investigated; the relationship between defect and WR strength should be further determined through a large number of experimental studies, so as to achieve real and accurate prediction of WR service life; and relevant standards should be further improved and developed combining the research results with the practical experience.
- (2) Optical detection method: methods to reduce or eliminate the influence of oil and light on the surface of WRs should be further designed; deep learning method is expected to be introduced because of its strong data mining ability, and more efficient, accurate, and robust algorithm than the traditional machine learning should be designed; to make the designed algorithm more robust, a big data set of WR surface defects with different WR types and different sizes (diameter, wire number) is expected to be established to cover all sample space.
- (3) Other detection methods: theoretical and experimental research, especially ultrasonic guided wave method, acoustic emission method, eddy current detection method and ray detection method, should be further deepened, and the intrinsic relationship between detection methods and the respective parameters of WR is expected to be explored; at the same time, relevant detection equipment should be designed and optimized to promote the development of related technologies.

- (4) Comprehensive application: a promising avenue for research is to combine various methods to characterize and detect damages from multiple dimensions. For example, the combination of electromagnetic method and optical method can not only grasp the size of effective cross-sectional area of WRs, the types of internal and external damages in real time, but also intuitively master its surface morphology characteristics, so as to provide more valuable parameters for the WR health evaluation.

Although there are many issues and challenges, as new technologies/methods and algorithms are introduced, it is believed that this field will have a more and more prospective future and one day it will be possible to truly realize efficient and accurate non-destructive detection of WRs.

We believe that this review has synthesized individual pieces of information on non-destructive damage detection of steel WRs and has provided a comprehensive reference for these readers who are interested in this research field.

**Author Contributions:** Conceptualization, P.Z. and G.Z.; Formal analysis, P.Z., G.Z., Z.Z., and Z.H.; Funding acquisition, G.Z. and P.Z.; Investigation, P.Z., Z.Z., X.D., C.T., and Z.H.; Supervision, G.Z., Z.Z., C.T., and Z.H.; Writing—original draft, P.Z.

**Funding:** This work was supported by the National Key Research and Development Program of China (grant number 2016YFC0600905), by the Postgraduate Research & Practice Innovation Program of Jiangsu Province (grant number KYCX19\_2140) and Postgraduate Research & Practice Innovation Program of China University of Mining and Technology (grant number KYCX19\_2140), by the Jiangsu Provincial Outstanding Youth Fund of China (grant number BK20180033), by the National Natural Science Foundation of China (grant number 51575513), and by the Project Funded of the Priority Academic Program Development of Jiangsu Higher Education Institutions (PAPD).

**Acknowledgments:** Thanks for the journal editors for their kind invitation to present this feature article. We wish to thank the authors of all references for their outstanding contributions in this field. At the same time, the authors would like to thank all reviewers and editors for their constructive comments.

**Conflicts of Interest:** The authors declare no conflict of interest.

## References

1. Mouradi, H.; Barkany, A.E.; Biyaali, A.E. Steel wire ropes failure analysis: Experimental study. *Eng. Fail. Anal.* **2018**, *91*, 234–242. [[CrossRef](#)]
2. Henao, H.; Fatemi, S.M.J.R.; Capolino, G.A.; Sieg-Zieba, S. Wire rope fault detection in a hoisting winch system by motor torque and current signature analysis. *IEEE Trans. Ind. Electron.* **2011**, *58*, 1727–1736. [[CrossRef](#)]
3. Peng, Y.X.; Chang, X.D.; Sun, S.S.; Zhu, Z.C.; Gong, X.S.; Zou, S.Y.; Xu, W.X.; Mi, Z.T. The friction and wear properties of steel wire rope sliding against itself under impact load. *Wear* **2018**, *400*, 194–206. [[CrossRef](#)]
4. Krešák, J.; Peterka, P.; Kropuch, S.; Novák, L. Measurement of tight in steel ropes by a mean of thermovision. *Measurement* **2014**, *50*, 93–98. [[CrossRef](#)]
5. Yuan, F.; Hu, B.L.; Zhou, Z.J. An analysis on the research status quo and prospects of defect detection methods of wire ropes. *Mach. Des. Manuf.* **2010**, *2*, 260–262. [[CrossRef](#)]
6. Čereška, A.; Zavadskas, E.K.; Bucinskas, V.; Podvezko, V.; Sutinyas, E. Analysis of steel wire rope diagnostic data applying multi-criteria methods. *Appl. Sci.* **2018**, *8*, 260. [[CrossRef](#)]
7. Zhang, J.W.; Tan, X.J.; Zheng, P.B. Non-destructive detection of wire rope discontinuities from residual magnetic field images using the hilbert-huang transform and compressed sensing. *Sensors* **2017**, *17*, 608. [[CrossRef](#)] [[PubMed](#)]
8. Tan, J.W. *Principle and Technology of Steel Wire Rope Safety Detection*; Science Press: Beijing, China, 2009.
9. Yang, S.Z.; Kang, Y.H.; Chen, H.G.; Yuan, J.M. *Electromagnetic Nondestructive Testing of Wire Ropes*; Machinery Industry Press: Beijing, China, 2017.
10. Gu, W.; Chu, J.X. A transducer made up of fluxgate sensors for testing wire rope defects. *IEEE Trans. Instrum. Meas.* **2002**, *51*, 120–124. [[CrossRef](#)]
11. Tan, X.J. Research on Non-Destructive Testing of Ferromagnetic Components with Weak Magnetic Imaging; In a Case of Wire Rope. Master's Thesis, Henan University of Science and Technology, Henan, China, 2018.

12. Norouzi, E.; Ravanbod, H. Optimization of the flux distribution in magnetic flux leakage testing. *Mater. Eval.* **2010**, *3*, 360–364. [[CrossRef](#)]
13. Zhao, M.; Zhang, D.L. Magnetic flux leakage of typical defect of wire rope based on FE simulation. *Nondestruct. Test.* **2009**, *31*, 177–180.
14. Lenard, S.; Atherton, D.L. Calculation of the effects of anisotropy on magnetic flux leakage detector signals. *IEEE Trans. Magn.* **1996**, *32*, 1905–1909. [[CrossRef](#)]
15. Krzywosz, K. Comparison of electromagnetic techniques for nondestructive inspection of ferromagnetic tubing. *Mater. Eval.* **1990**, *48*, 42–45.
16. Kalwa, E.; Piekarski, K. Design of inductive sensors for magnetic testing of steel ropes. *NDT E Int.* **1991**, *24*, 328. [[CrossRef](#)]
17. Dutta, S.M.; Ghorbel, F.H.; Stanley, R.K. Simulation and analysis of 3-D magnetic flux leakage. *IEEE Trans. Magn.* **2009**, *45*, 1966–1972. [[CrossRef](#)]
18. Trevino, D.A.G.; Dutta, S.M.; Ghorbel, F.H.; Karkoub, M. An improved dipole model of 3-D magnetic flux leakage. *IEEE Trans. Magn.* **2016**, *52*, 1–7. [[CrossRef](#)]
19. Sun, Y.H.; Kang, Y.H. Magnetic mechanisms of magnetic flux leakage nondestructive testing. *Appl. Phys. Lett.* **2013**, *103*, 184104. [[CrossRef](#)]
20. Gao, G.H.; Lian, M.J.; Xu, Y.G.; Qin, Y.N.; Gao, L. The effect of variable tensile stress on the MFL signal response of defective wire ropes. *INSIGHT* **2016**, *58*, 135–141. [[CrossRef](#)]
21. Coramik, M.; Ege, Y. Discontinuity inspection in pipelines: A comparison review. *Measurement* **2017**, *111*, 359–373. [[CrossRef](#)]
22. Kang, Y.H.; Li, Z.J.; Yang, Y.; Qiu, C. Mini-micro sensor and device for wire rope MFL testing. *Nondestruct. Test.* **2014**, *36*, 11–15.
23. Wang, H.Y.; Hua, G.; Tian, J. Research on detection device for broken wires of coal mine-hoist cable. *J. Chin. Univ. Mini. Technol.* **2007**, *17*, 376–381. [[CrossRef](#)]
24. Jomdecha, C.; Prateepasen, A. Design of modified electromagnetic main-flux for steel wire rope inspection. *NDT E Int.* **2009**, *42*, 77–83. [[CrossRef](#)]
25. Wang, H.Y.; Xu, Z.; Hua, G.; Tian, J.; Zhou, B.B.; Lu, Y.H.; Chen, F.J. Key technique of a detection sensor for coal mine wire ropes. *Min. Sci. Technol.* **2009**, *19*, 170–175. [[CrossRef](#)]
26. Song, K.; Chen, C.; Kang, Y.H.; Li, J.J.; Ren, J.L. Mechanism study of AC-MFL method using U-shape inducer. *Chin. J. Sci. Instrum.* **2012**, *33*, 1980–1985. [[CrossRef](#)]
27. Yan, X.L.; Zhang, D.L.; Pan, S.M.; Zhao, E.C.; Gao, W. Online nondestructive testing for fine steel wire rope in electromagnetic interference environment. *NDT E Int.* **2017**, *92*. [[CrossRef](#)]
28. Kaur, A.; Gupta, A.; Aggarwal, H.; Arora, K.; Garg, N.; Sharma, M.; Sharma, S.; Aggarwal, N.; Sapra, G.; Goswamy, J.K. Non-destructive evaluation and development of a new wire rope tester using parallelly magnetized NdFeB magnet segments. *J. Nondestruct. Eval.* **2018**, *37*, 61. [[CrossRef](#)]
29. Sun, Y.H.; Wu, J.B.; Feng, B.; Kang, Y.H. An opening electric-mfl detector for the ndt of in-service mine hoist wire. *IEEE Sens. J.* **2014**, *14*, 2042–2047. [[CrossRef](#)]
30. Liu, X.C.; Xiao, J.W.; Wu, B.; He, C.F. A novel sensor to measure the biased pulse magnetic response in steel stay cable for the detection of surface and internal flaws. *Sens. Actuators A Phys.* **2018**, *269*, 218–226. [[CrossRef](#)]
31. Yan, X.L.; Zhang, D.L.; Zhao, F. Improve the signal to noise ratio and installation convenience of the inductive coil for wire rope nondestructive testing. *NDT E Int.* **2017**, *92*, 221–227. [[CrossRef](#)]
32. Fedorko, G.; Molnár, V.; Ferková, Ž.; Peterka, P.; Krešák, J.; Tomašková, M. Possibilities of failure analysis for steel cord conveyor belts using knowledge obtained from non-destructive testing of steel ropes. *Eng. Fail. Anal.* **2016**, *67*, 33–45. [[CrossRef](#)]
33. Sun, Y.H.; Liu, S.W.; Li, R.; Ye, Z.J.; Kang, Y.H.; Chen, S.B. A new magnetic flux leakage sensor based on open magnetizing method and its on-line automated structural health monitoring methodology. *Struct. Health Monit.* **2015**, *14*, 583–603. [[CrossRef](#)]
34. Xu, F.Y.; Wang, X.S.; Wu, H.T. Inspection method of cable-stayed bridge using magnetic flux leakage detection: Principle, sensor design, and signal processing. *J. Mech. Sci. Technol.* **2012**, *26*, 661–669. [[CrossRef](#)]
35. Wang, H.T.; Tian, J.; Meng, G.Y. A sensor model for defect detection in mine hoisting wire ropes based on magnetic focusing. *INSIGHT* **2017**, *59*, 143–148. [[CrossRef](#)]

36. Kim, J.W.; Park, S. Magnetic flux leakage sensing and artificial neural network pattern recognition-based automated damage detection and quantification for wire rope non-destructive evaluation. *Sensors* **2018**, *18*, 109. [[CrossRef](#)]
37. Tian, J.; Wang, H.Y. Research on magnetic excitation model of magnetic flux leakage for coal mine hoisting wire rope. *Adv. Mech. Eng.* **2015**, *7*, 1–11. [[CrossRef](#)]
38. Zhou, J.Y.; Tian, J.; Wang, H.Y.; Li, Y.M.; Wu, M. Numerical simulation of magnetic excitation based on a permanent magnet co-directions array sensor. *INSIGHT* **2018**, *60*, 568–574. [[CrossRef](#)]
39. Singh, W.S.; Rao, B.P.C.; Mukhopadhyay, C.K.; Jayakumar, T. GMR-based magnetic flux leakage technique for condition monitoring of steel track rope. *INSIGHT* **2011**, *53*, 377–381. [[CrossRef](#)]
40. Liu, X.C.; Wang, Y.J.; Wu, B.; Gao, Z.; He, C.F. Design of tunnel magneto-resistive-based circular MFL sensor array for the detection of flaws in steel wire rope. *J. Sens.* **2016**, *2016*. [[CrossRef](#)]
41. Lu, T.; Zhang, L.H. *Wire Rope Inspector*; China University of Mining and Technology Press: Xuzhou, China, 2007; pp. 74–78.
42. Zhou, P.; Zhou, G.B.; He, Z.Z.; Tang, C.Q.; Zhu, Z.C.; Li, W. A novel texture-based damage detection method for wire ropes. *Measurement* **2019**. under review.
43. Vallan, A.; Molinari, F. A vision-based technique for lay length measurement of metallic wire ropes. *IEEE Trans. Instrum. Meas.* **2009**, *58*, 1756–1762. [[CrossRef](#)]
44. Yaman, O.; Karakose, M. Auto-correlation based elevator rope monitoring and fault detection approach with image processing. In Proceedings of the 2017 International Artificial Intelligence and Data Processing Symposium (IDAP), Malatya, Turkey, 16–17 September 2017.
45. Sun, H.X.; Zhang, Y.H.; Luo, F.L. Texture segmentation and boundary recognition of wire rope images in complicated background. *Acta Photonica Sinica* **2010**, *39*, 1666–1671. [[CrossRef](#)]
46. Platzer, E.S.; Nägele, J.; Wehking, K.H.; Denzler, J. HMM-based defect localization in wire ropes—a new approach to unusual subsequence recognition. Pattern Recognition. In Proceedings of the Dagm Symposium, Jena, Germany, 9–11 September 2009; pp. 442–451.
47. Platzer, E.S.; Wehking, K.H.; Denzler, J. On the suitability of different features for anomaly detection in wire ropes. In Proceedings of the International Conference on Computer Vision, Imaging and Computer Graphics, Lisboa, Portugal, 5–8 February 2009; pp. 296–308.
48. Wacker, E.S.; Denzler, J. Enhanced anomaly detection in wire ropes by combining structure and appearance. *Pattern Recognit. Lett.* **2013**, *34*, 942–953. [[CrossRef](#)]
49. Wacker, E.S.; Denzler, J. An analysis-by-synthesis approach to rope condition monitoring. In Proceedings of the International Symposium on Visual Computing, Las Vegas, NV, USA, 29 November–1 December 2010; pp. 459–468.
50. Sanchez-Brea, L.M.; Siegmann, P.; Rebollo, M.A.; Bernabeu, E. Optical technique for the automatic detection and measurement of surface defects on thin metallic wires. *Appl. Opt.* **2000**, *39*, 539–545. [[CrossRef](#)] [[PubMed](#)]
51. Laguerre, L.; Treysède, F. Non-destructive evaluation of seven-wire strands using ultrasonic guided waves. *Eur. J. Environ. Civil Eng.* **2011**, *15*, 487–500. [[CrossRef](#)]
52. Raisutis, R.; Kazys, R.; Mazeika, L.; Zukauskas, E.; Samaitis, V.; Jankauskas, A. Ultrasonic guided wave-based testing technique for inspection of multi-wire rope structures. *NDT E Int.* **2014**, *62*, 40–49. [[CrossRef](#)]
53. Liu, Z.H.; Zhao, J.C.; Wu, B.; Zhang, Y.N.; He, C.F. Configuration optimization of magnetostrictive transducers for longitudinal guided waves inspection in seven-wire steel strands. *NDT E Int.* **2010**, *43*, 484–492. [[CrossRef](#)]
54. Treysède, F.; Laguerre, L. Investigation of elastic modes propagating in multi-wire helical waveguides. *J. Sound Vib.* **2010**, *329*, 1702–1716. [[CrossRef](#)]
55. Vanniamparambil, P.A.; Khan, F.; Hazeli, K.; Cuadra, J.; Schwartz, E.; Kontsos, A.; Bartoli, I. Novel optico-acoustic nondestructive testing for wire break detection in cables. *Struct. Control Health Monit.* **2013**, 1319–1350. [[CrossRef](#)]
56. Xu, J.; Wu, X.J.; Sun, P.F. Detecting broken-wire flaws at multiple locations in the same wire of prestressing strands using guided waves. *Ultrasonics* **2013**, *53*, 150–156. [[CrossRef](#)]
57. Raisutis, R.; Kazys, R.; Mazeika, L.; Samaitis, V.; Zukauskas, E. Propagation of ultrasonic guided waves in composite multi-wire ropes. *Materials* **2016**, *9*, 451. [[CrossRef](#)]
58. Tse, P.W.; Rostami, J. Advanced signal processing methods applied to guided waves for wire rope defect detection. In *AIP Conference Proceedings*; AIP Publishing: College Park, MD, USA, 2016; Volume 1706, p. 030006.
59. Li, H.; Wang, W.T.; Zhou, W.S. Fatigue damage monitoring and evolution for basalt fiber reinforced polymer materials. *Smart Struct. Syst.* **2014**, *14*, 307–325. [[CrossRef](#)]

60. Hoon, S.; Gyuhae, P.; Jeannette, R.W.; Nathan, P.L.; Charles, R.F. Wavelet-based active sensing for delamination detection in composite structures. *Smart Mater. Struct.* **2003**, *13*, 153. [[CrossRef](#)]
61. Drummond, G.; Watson, J.F.; Acarnley, P.P. Acoustic emission from wire ropes during proof load and fatigue testing. *NDT E Int.* **2007**, *40*, 94–101. [[CrossRef](#)]
62. Bai, W.; Chai, M.; Li, L.; Li, Y.; Duan, Q. Acoustic emission from elevator wire ropes during tensile testing. In *Advances in Acoustic Emission Technology: Proceedings of the World Conference on Acoustic Emission-2013*; Springer: New York, NY, USA, 2013; pp. 217–224.
63. Casey, N.F.; Taylor, J.L. Acoustic emission of steel wire ropes. *Wire Ind.* **1984**, *51*, 79–82.
64. Casey, N.F.; Taylor, J.L. Evaluation of wire ropes by AE techniques. *Brit. J. Non. Destruct. Test.* **1985**, *27*, 351–356.
65. Casey, N.F.; Wedlake, D.; Taylor, J.L.; Holford, K.M. Acoustic detection of wire rope failure. *Wire Ind.* **1985**, *52*, 307–309.
66. Casey, N.F.; Taylor, J.L.; Holford, K.M. Wire break detection during tensile fatigue testing of 40 mm wire rope. *Brit. J. Non. Destruct. Test.* **1985**, *30*, 338–341.
67. Casey, N.F.; White, H.; Taylor, J.L. Frequency analysis of the signals generated by the failure of constituent wires of a wire rope. *NDT E Int.* **1989**, *56*, 583–586. [[CrossRef](#)]
68. Casey, N.F.; Laura, P.A.A. A review of the acoustic-emission monitoring of wire rope. *Ocean Eng.* **1997**, *24*, 935–947. [[CrossRef](#)]
69. Shao, Y.B.; Yu, D.; Wang, S.; Zhu, Z.M.; Yin, W.Q. Quantitative method to detect wire break in wire rope by acoustic emission techniques. *J. Northeast. Univ. Nat. Sci.* **1999**, *20*, 130–132.
70. Ding, Y.; Reuben, R.L.; Steel, J.A. A new method for waveform analysis for estimating AE wave arrival times using wavelet decomposition. *NDT E Int.* **2004**, *37*, 279–290. [[CrossRef](#)]
71. Li, S.; Wu, Y.; Shi, H. A novel acoustic emission monitoring method of cross-section precise localization of defects and wire breaking of parallel wire bundle. *Struct. Control Health Monit.* **2019**, *26*, e2334. [[CrossRef](#)]
72. Li, H.; Huang, Y.; Chen, W.L.; Ma, M.L.; Tao, D.W.; Ou, J.P. Estimation and warning of fatigue damage of FRP stay cables based on acoustic emission techniques and fractal theory. *Comput. Aided Civil Infrastruct. Eng.* **2011**, *26*, 500–512. [[CrossRef](#)]
73. Cao, Q.S.; Liu, D.; Zhou, J.H.; Zhou, J.M. Non-destructive and quantitative detection method for broken wire rope. *Chin. J. Sci. Instrum.* **2011**, *32*, 787–794. [[CrossRef](#)]
74. Cao, Q.S.; Liu, D.; He, Y.H.; Zhou, J.H.; Codrington, J. Nondestructive and quantitative evaluation of wire rope based on radial basis function neural network using eddy current inspection. *NDT E Int.* **2012**, *46*, 7–13. [[CrossRef](#)]
75. Zhang, Y.C.; Xu, G.Y.; Cui, J. System used to detect steel wire rope based on X-ray digital imaging technology. *Image Technol.* **2008**, *2*, 33–39.
76. Peng, P.C.; Wang, C.Y. Use of gamma rays in the inspection of steel wire ropes in suspension bridges. *NDT E Int.* **2015**, *75*, 80–86. [[CrossRef](#)]
77. Cao, Y.N.; Zhang, D.L.; Xu, D.G. The state-of-art of quantitative nondestructive testing of wire ropes. *Nondestruct. Test.* **2005**, *27*, 91–95.
78. Wu, P.; Hua, H.Y. Discussion on the existing problems of steel wire rope nondestructive testing. *Nondestruct. Test.* **2017**, *39*, 65–68. [[CrossRef](#)]
79. Zhou, P.; Zhou, G.B.; Zhu, Z.C.; Tang, C.Q.; He, Z.Z.; Li, W.; Jiang, F. Health monitoring for balancing tail ropes of a hoisting system using a convolutional neural network. *Appl. Sci.* **2018**, *8*, 1346. [[CrossRef](#)]
80. Guo, X.J.; Chen, L.; Shen, C.Q. Hierarchical adaptive deep convolution neural network and its application to bearing fault diagnosis. *Measurement* **2016**, *93*, 490–502. [[CrossRef](#)]
81. Zhao, R.; Yan, R.Q.; Chen, Z.H.; Mao, K.Z.; Wang, P.; Gao, X. Deep learning and its applications to machine health monitoring. *Mech. Syst. Signal Process.* **2019**, *115*, 213–237. [[CrossRef](#)]
82. Guo, X.J.; Shen, C.Q.; Chen, L. Deep fault recognizer: An integrated model to denoise and extract features for fault diagnosis in rotating machinery. *Appl. Sci.* **2017**, *7*, 41. [[CrossRef](#)]
83. Zhou, P.; Zhou, G.B.; He, Z.Z.; Zhu, Z.C.; Tang, C.Q.; Li, W. A novel deep learning-based damage monitoring and diagnosis method for wire ropes. *Mech. Syst. Signal Process.* **2019**. under review.



Article

# Lock-In Thermography and Ultrasonic Testing of Impacted Basalt Fibers Reinforced Thermoplastic Matrix Composites

Simone Boccardi <sup>1,2</sup>, Natalino Daniele Boffa <sup>1</sup>, Giovanni Maria Carlomagno <sup>1</sup>,  
Giuseppe Del Core <sup>2</sup>, Carosena Meola <sup>1,\*</sup>, Ernesto Monaco <sup>1</sup>, Pietro Russo <sup>3</sup> and Giorgio Simeoli <sup>3</sup>

<sup>1</sup> Department of Industrial Engineering—Aerospace Division, University of Naples Federico II,  
Via Claudio, 21, 80125 Napoli, Italy

<sup>2</sup> Department of Science and Technology, University of Naples Parthenope, Centro Direzionale, Isola C4,  
80143 Napoli, Italy

<sup>3</sup> Institute for Polymers, Composites and Biomaterials, National Council of Research,  
80078 (NA) Pozzuoli, Italy

\* Correspondence: carmeola@unina.it

Received: 27 June 2019; Accepted: 25 July 2019; Published: 26 July 2019

**Featured Application:** The term “new material” may raise enthusiasm as well as skepticism at the same time. The acceptance of new material is generally linked to its characteristics with respect to the commonly used materials such as better performance, the solution to an open question, non- or less-polluting, cheaper, easy to handle, etc. Of course, these characteristics must be certified; therefore, the production should be accompanied by effective testing techniques and procedures. The scope of this work is to contribute to assessing the effectiveness of non-destructive testing through the examination of both lock-in thermography and ultrasonic testing techniques applied to basalt-based composites.

**Abstract:** Basalt fibers are receiving increasing consideration because they seem to be adequate as reinforcement of composites and to comply with the environmental safeguard rules. However, many factors affect the performance of composite material, demanding specific testing; one may be performance assessment under impact tests. The attention of the present work is focused on the detection of impact damage in basalt-based composites with two non-destructive testing techniques: lock-in thermography (LT) and ultrasonic testing (UT). Two different types of materials are considered which both include basalt fibers as reinforcement but two different matrices: Polyamide and polypropylene. Polypropylene is used either pure or modified with the addition of a coupling agent; the latter improves the fiber/matrix interface strength, giving in practice, a material of different characteristics. Specimens are first subjected to low-velocity impact tests and then non-destructively examined with the two above mentioned techniques. The obtained results are analyzed and compared to highlight the advantages and limitations of the two techniques to detect impact damage in basalt-based composites. Both techniques seem effective for the inspection of polyamide/basalt composite; in particular, there is a general agreement between results. Conversely, UT seems not suitable for the inspection of polypropylene/basalt composites because of their superficial porosity, while lock-in thermography is effective also for this type of composite material.

**Keywords:** basalt fibers; polyamide; polypropylene; composites; impact damage; lock-in thermography; ultrasonic testing

## 1. Introduction

The development of new materials is an increasingly topical issue of great interest to both the academic and the industrial communities. This is because of many reasons. Amongst them, the performance of a product depends mostly on the material which it is made of, and a demand for materials of superior characteristics. Another important question is the environmental safeguard, which requires the development of more environmentally friendly materials. Therefore, the attention is ever more shifting from petrochemical resources to more natural (e.g., vegetables) substances. The hope is to be able to get eco-friendly composite materials which include both the matrix and reinforcement of natural derivation and which perform better, or at least similar to the most common composites of petrochemical derivation. This seems not completely achievable yet; what is instead possible is to reduce the problems of waste disposal. In this context, thermoplastic matrix-based composites (TC), thanks to their potential recyclability after their life-cycle, offer some advantages over their thermoset counterparts [1]. Another step forward may be to use natural fibers as reinforcement of thermoplastic matrices. A convenient reinforcement may be basalt.

Basalt is available in nature in volcanic rocks and can be reduced in fibers, which are well suited to be used as reinforcement of both thermoset and thermoplastic matrices to create different types of composite materials [2].

Based on the investigation till now carried out [3,4], the obtained composites seem to have good features, which make them comparable, or superior, to the most commonly used composites. The basalt-based composites could be adequate for the construction of some aircraft parts and of unmanned aerial vehicles like drones, which are ever more applied in different sectors such as surveillance and remote inspection. However, such adequacy should be ascertained since many factors affect the performance of a composite material. This one must be subjected to many tests prior to its introduction in the market for the construction of any goods. Amongst them, it is generally important to assess the material resistance to an impact load. The latter can be inadvertently induced during either manufacturing, through the impact of falling objects, or in service, and can cause barely visible damage. Therefore, the availability of effective non-destructive testing (NDT) techniques is fundamental to get information on the damage induced especially by low energy impact.

Today, many different NDT techniques are available, but none can be considered as superior and very effective; in fact, every technique has its inherent limitations. A good practice is to choose the most adequate technique to the specific application but, frequently, an effective routine may be to use more than one technique in the light of a data integration/fusion approach.

The attention of the present work is focused on the detection of low energy impact damage in basalt-based composites with two techniques: lock-in thermography (LI) and ultrasonic testing (UT). Both techniques were already used successfully to detect the impact damage of carbon-based composites [5] and now are considered again for the inspection of basalt-based composites. Basalt fibers are used as reinforcement of a polyamide matrix and of a polypropylene (PP) one, which is used either pure, or modified with the addition of a coupling agent; the latter improves the fiber/matrix interface strength, giving in practice, a material of different characteristics. Therefore, three different materials are inspected. Specimens are first subjected to low velocity/energy impact tests and then non-destructively examined with the two above mentioned techniques. The obtained results are compared to highlight the advantages and limitations of the two techniques within the inspection of basalt-based composites. In addition to the Introduction, this work is organized into several sections. Section 2, titled Materials and Methods, includes a description of the used materials and specimens and how they are impacted as well as of the two non-destructive techniques: lock-in thermography and ultrasonic testing. Section 3 reports Results separately in Section 3.1 for polyamide matrix-based specimen and in Section 3.2 for polypropylene matrix-based specimens. Section 4 titled: Data Discussion and Concluding Remarks will close the paper.

## 2. Materials and Methods

### 2.1. Description of Specimens

A woven basalt fibers fabric, plain weave type, with a specific mass of  $210 \text{ g/m}^2$ , from Incotology, GmbH is used as reinforcement of two types of matrix: Polypropylene and polyamide. The first is polypropylene, Hyosung Topilene PP J640 (MFI@230 °C, 2.16 kg: 10 g/10 min; Songhan Plastic Technology Co., Ltd., Shanghai, China), which is used pure, or modified by adding 2% in weight of Polybond 3000 (PP-g-MA, MFI@190 °C, 2.16 kg: 405 g/10 min; 1.2% in weight of maleic anhydride, by Chemtura, Philadelphia, PA, USA). The other is polyamide (PA6) Lanxess Durethan B30S-000000 (MFI@260 °C, 5 kg: 102 g/10 min). Then, three types of specimens, named: PPB, PC2B, and PA6B are prepared with a pure PP (PPB), a modified one (PC2B), and a polyamide (PA6B) matrix. For the last, the neat interface without any coupling agent has been chosen even if there is mention in the literature of the enhancement introduced by silane coupling [6].

Each specimen includes 18 balanced basalt fabric layers  $0^\circ/90^\circ$  symmetrically arranged with respect to the middle plane of the laminate  $[(0/90)_9]_s$  configuration), with a basalt fiber content of 50% by volume (the actual relative percentages of fiber and matrix evaluated according to ASTM D 3171-04, Test Method II). The percentage of 50% has been chosen as an optimal value through preliminary tests. Laminates are obtained by alternating layers of matrix films (PP, PC2, PA6) with basalt fibers fabric by the hand lay-up film-stacking technique and compacted with the aid of a compression molding machine (model P400E, Collin GmbH, Germany) under pre-optimized molding conditions (Figure 1). Each specimen is  $300 \text{ mm} \times 300 \text{ mm}$  with a target thickness of 3 mm.

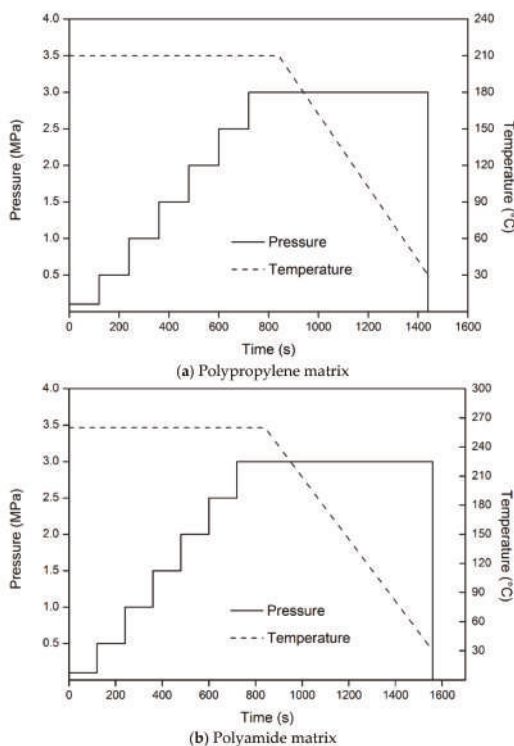


**Figure 1.** Molding compression pressure and temperature against time for polypropylene (PP) based (a) and polyamide (PA6B) based (b) matrices.

Some specific details of investigated specimens in terms of code, thickness, and composition are summarized in Table 1.

**Table 1.** Some specimens details.

| Code | Matrix                                       | Thickness (mm) |
|------|--|----------------|
| PA6B | Polyamide                                    | 3.0            |
| PPB  | Pure polypropylene                           | 3.0            |
| PC2B | Polypropylene added with 2% maleic anhydride | 3.0            |

### 2.2. Impact Tests

Impact tests are carried out with a modified Charpy pendulum with a hemispherical shaped hammer nose, 12.7 mm in diameter. Each specimen is placed inside a special fixture which includes two large plates, each having a window 12.5 cm × 7.5 cm to allow for the contact with the hammer from one side and likely optical view by an infrared imaging device from the other one [7]. The impact energy varied between 5 and 15 J and is set by suitably adjusting the falling height of the Charpy arm. The choice of the impact energy was to induce mostly barely visible damage to different levels without perforation.

### 2.3. Non-Destructive Evaluation

After impact two non-destructive testing techniques are used: lock-in thermography and ultrasonic testing.

#### 2.3.1. Lock-In Thermography

The test setup includes the impacted specimen, the infrared camera, and two halogen lamps (1 kW each) for thermal stimulation of the specimen [8]. The used infrared camera is the SC6000 (Flir systems), which is equipped with a QWIP detector, working in the 8–9 μm infrared band, NEDT <35 mK, spatial resolution 640 × 512 pixels full-frame, pixel size 25 μm × 25 μm and with a windowing option linked to frequency frame rate and temperature range. The camera is equipped with the lock-in module that drives the halogen lamps to generate a sinusoidal thermal wave of selectable frequency  $f$  and with the IRLock-In© software for data analysis.

Lock-in thermography is a well-known technology and will not be herein described in detail; only a sketch of the test setup (Figure 2) and some basics are recalled for easy reading. The thermal wave, delivered to the specimen surface, propagates inside the material and gets reflected when it reaches parts where the heat propagation parameters change (in-homogeneities). The reflected wave interacts with the surface wave producing an oscillating interference pattern, which can be measured in terms of either temperature amplitude, or phase angle  $\varphi$ , and represented as an amplitude, or phase, image, respectively. The basic link of the thermal diffusion length  $\mu$  to the heating frequency  $f$  and to the mean material thermal diffusivity coefficient  $\alpha$  is via the relationship:

$$\mu = \sqrt{\frac{\alpha}{\pi f}}. \tag{1}$$

The depth range for the amplitude image is given by  $\mu$ , while the maximum depth  $p$ , which can be reached for the phase image, corresponds to 1.8  $\mu$  [9–12]. In general, it is preferable to reduce data in terms of phase image because of its insensitivity to either non-uniform heating or local variations of emissivity over the monitored surface. The material thickness, which can be inspected, depends on the wave period (the longer the period, the deeper the penetration) and on the material thermal diffusivity.

As stated in Equation (1), to check the material conditions at a given depth, both the knowledge of the thermal diffusivity and the correct choice of the heating frequency are fundamental parameters. The thermal diffusivity can be evaluated with either the lock-in technique itself or with flash thermography.

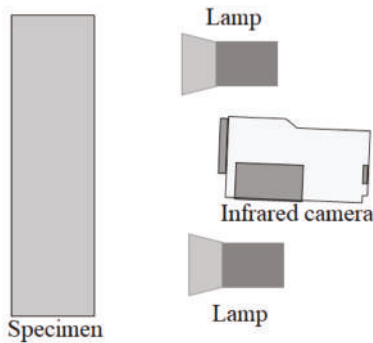


Figure 2. Scheme of the lock-in thermography setup.

### 2.3.2. Ultrasonic Testing

Ultrasonic non-destructive inspection is performed with an ultrasonic flaw detector Olympus OmniScan SX with phased array unit (Figure 3). The Omniscan detector is equipped with a phased array 16:64PR probe and with an ultrasonic (UT) conventional channel allowing for pulse-echo (PE), pitch-catch, or time-of-flight diffraction (TOFD) methods of inspection [13]. To perform the inspection the phased array probe elements are pulsed simultaneously, or with a time lag, in order to promote ultrasonic beamforming that is the constructive interference of multiple-beam components into a single wavefront traveling in the desired direction. Correspondingly, in the acquiring mode, the receiver is able to combine the signals (echoes) coming from multiple elements (reflectors) into a single representation. Exploiting the phasing technology that allows beam shaping and steering, it is possible to generate a wide variety of ultrasonic beam profiles with a single probe assembly, and, at the same time, to dynamically set the beam steering to perform electronic scans.



Figure 3. Some details of the ultrasonic (UT) testing setup.

Phased array ultrasonic instruments, whose operating principle relies on the physics that governs sound wave propagation, apply high-frequency sound waves to either detect buried anomalies or measure the thickness of a testing article [14]. The capability to produce multiple transducer paths within one probe represents a great advantage in defects detection and visualization [15]. Phased array imaging allows seeing relative point by point changes and multidirectional defect responses, which help in flaw detection, discrimination, and sizing [16].

In particular, the ultrasonic device records two parameters of the reflected echo: The amplitude and the echo time of flight with respect to a zero point (pulse transit time). The echo time of flight, in

turn, is correlated with the depth or distance of the reflector, exploiting the sound velocity knowledge of the tested material and the simple relationship:

$$\text{Distance} = \text{velocity} \times \text{time}. \quad (2)$$

The fundamental presentation of ultrasonic waveform data is the A-scan graph, in which amplitude and transit time of the echo are plotted on a grid where the vertical axis represents the amplitude and the horizontal axis represents the time of flight.

A different plotting way is in the form of B-scan, which visualizes the depth of reflectors (a defect/damage) with respect to their position along the scanning axis. The inspected test article thickness is plotted as a function of time or position while the probe is moved along the upper part surface to provide material depth profile. The correlation of echoes data with the transducer positions allows a through-thickness representation of the material and to link track data with the specific inspected areas.

The probe position tracking is performed by the use of an electromechanical encoder, a small wheel connected to the probe, that enables the position and orientation of the probe along the scanning axis to be recorded with the echoes amplitude data (A-scan) allowing the 2D reconstructions. A useful 2D presentation option is the C-scan graph, in which the data are displayed in a top or planar view of the test piece, something similar to an x-ray image, where color represents the signal amplitude or the reflector depth at each point of the inspected test piece.

In the present work, tests are performed by means of an encoded 5 MHz, phased array transducer with 64 active elements arranged in a linear array with a pitch of 1 mm and a straight wedge. The system calibration is performed by considering the specimen thickness as a reference, so no calibration blocks are used.

### 3. Results

Results are presented as phase images for LT and as C-scan and B-scan images, amplitude top and sectional views respectively, for ultrasonic testing (UT); data are compared to highlight the advantages and limitations of the two techniques. As the first and most important observation, the comparison between LT and UT is done only for the PA6B specimen. This is because, from preliminary tests, the surface of both PPB and PC2B specimens are found to be permeable to the ultrasonic coupling medium (water, or gel); this has made the C-scan inspection impossible to perform in consequence of the background noise amplification due to the liquid ingress effect, which blinds the ultrasonic device. Therefore, these two specimens are inspected only with LT.

#### 3.1. Polyamide Matrix-Based Specimen

Firstly, a photo of the PA6 specimen taken after impact is reported in Figure 4. As indicated, the specimen was subjected to four impacts with energies: 5, 9, and 15 J and with two impacts at the same  $E = 9$  J. The location of each impact is also recognizable from the light local surface discoloration.

Three phase images taken from the impacted side (shown in Figure 4) are reported in Figure 5; a reference target of 19 mm × 8 mm, clearly visible on each image, allows for fast estimation of the damage size. From these phase images it is possible to see that:

- There are dark stains in correspondence of the four impacts.
- The size of dark stains increases with the impact energy.
- Going in-depth, the stains first expand by decreasing  $f$  from 0.53 Hz (Figure 5a) to 0.36 Hz (Figure 5b), and after contracting to their initial size to a further reduction of  $f$  to 0.19 Hz (Figure 5c).



**Figure 4.** Photo of the polypropylene added with 2% maleic anhydride (PA6B) specimen with indicated energy and location of the impacts.

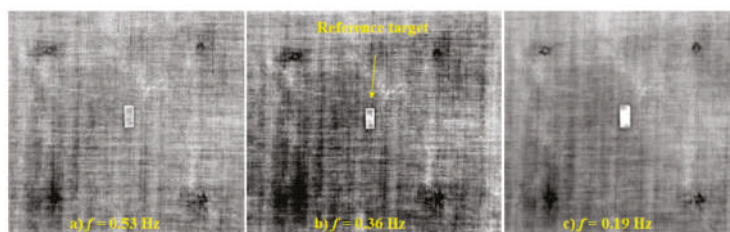


**Figure 5.** Phase images taken on the impacted side of the PA6B specimen at three heating frequencies; (a)  $f = 0.53$  Hz; (b)  $f = 0.36$  Hz; (c)  $f = 0.19$  Hz (see Figure 2 for impact energies location).

In particular, the dark zone centered at the impact point of  $E = 15$  J (Figure 5a) assumes for  $f = 0.36$  Hz (Figure 5b) a well H shaped configuration being representative of the delamination evolution along the vertical fiber's direction. Such a vertical displacement may be explicable owing to the fact that, during the impact, the specimen was positioned inside the lodge with the vertical direction of the fibers (as shown in Figure 5b) along the longer side of the lodge's window (12.5 cm  $\times$  7.5 cm). In addition, it is possible to see threadlike structures resembling cracks in the matrix which are most pronounced around the impact point of 9 J on the bottom (Figure 5b). However, apart from the clearly visible impact coupled stains, there are other dark zones mostly present on the phase image taken at  $f = 0.36$  Hz (Figure 5b), which are distributed away from the impact points and which may indicate that material in-homogeneities likely occurred during the manufacturing process. All of these dark structures fade going more in-depth; they remain clearly evident for  $f = 0.19$  Hz (Figure 5c) mostly around the impact points.

What is observed in Figure 5b is practically confirmed by the C-scan image of Figure 6a. In fact, the black color of Figure 5b is replaced by the dark blue color of Figure 6a to highlight the indentation of each impact and the most important damage.

In particular, it is confirmed the presence of delamination along the direction of the vertical fibers and it is also confirmed the presence of material in-homogeneity around impacts at 15 J, 9 J (on the right bottom), and 5 J and far away from the impact points. In addition, the dark structures around the impact at 5 J of Figure 5 are better depicted as blue-green structures in Figure 6. The comparison between Figures 5 and 6 helps to classify such structures as material in-homogeneities rather than impact-induced damage. As already evidenced, such in-homogeneities display their best contrast for  $f = 0.36$  Hz (Figure 5b) meaning that they are mostly located in the second half of the specimen thickness towards the bottom. It is worth noting that around the impact points in-homogeneities are present for lower  $f$  (Figure 5c) and so extend to the entire thickness. This set of evidence, probably

exacerbated by impact effects, are confirmed in the ultrasonic B-scan sections (Figure 6b), where it is possible to see wide porosity areas through the stratification close to the opposite surface of the impacted side.

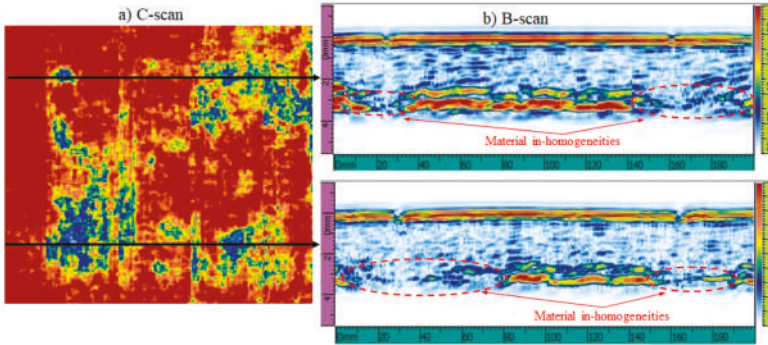


**Figure 6.** C-scan (a) and B-scan (b) images taken on the impacted side of the PA6B specimen (see Figure 4 for impact energies location).

### 3.2. Polypropylene Matrix-Based Specimens

The Figures 7 and 8 show phase images, taken from the impacted side, of the two specimens PPB (Figure 7) and PC2B (Figure 8), which were subjected to three impacts at 5 J, 9 J, and 15 J as indicated on the first image (a) of both Figures 8 and 9. Figure 9 shows a comparison between phase images taken at  $f = 0.19$  Hz from the rear side (opposite to impact) of the three specimens PA6B (Figure 9a), PPB (Figure 9b), and PC2B (Figure 9c).

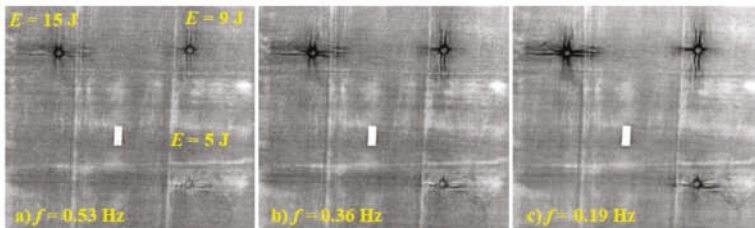


**Figure 7.** Phase images taken on the impacted side of the pure polypropylene (PPB) specimen at three heating frequencies; (a)  $f = 0.53$  Hz; (b)  $f = 0.36$  Hz; (c)  $f = 0.19$  Hz.

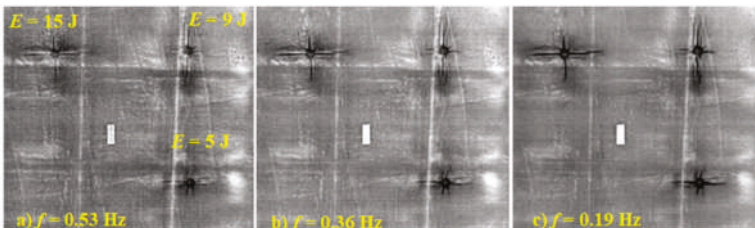


**Figure 8.** Phase images taken on the impacted side of the PC2B specimen at three heating frequencies; (a)  $f = 0.53$  Hz; (b)  $f = 0.36$  Hz; (c)  $f = 0.19$  Hz.

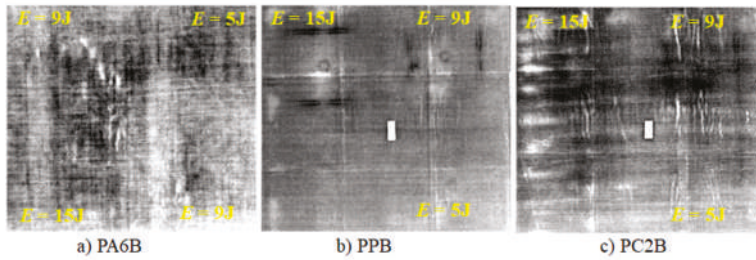


**Figure 9.** Phase images taken at  $f = 0.19$  Hz on the rear side of the three specimens; (a) PA6B; (b) PPB; (c) PC2B.

As a general observation, the occurred damage appears in the form of a cross-shaped structure with a central ring. The cross's branches indicate the main deformation directions while the ring may be assumed to coincide with the imprint of the impactor. The cross is more accentuated for the highest impact energy of 15 J and achieves its best contrast at  $f = 0.19$  Hz (Figure 7c Figure 8c). As a main difference between the two specimens, the cross is depicted by fan-like branches in the PPB specimen (Figure 7) and by almost straight lines in the PC2B one (Figure 8). Such a difference is a symptom of different behavior of the two materials under the impact. It is worth noting that the superimposed layers of the PPB specimen are not fully rigidly connected at their interface but are free to somehow mutually slide. Instead, the stronger bond entailed by the grafting agent in the PC2B specimen prevents slipping effects of layers and allows for bending and deformation through the entire thickness. This may entail wrinkling in the layers furthest from the impact point as shown in Figure 9c.

### 3.3. Measurement of Damage Extension

The extension of the occurred impact damage is evaluated by considering its elongation along horizontal ( $D_H$ ) and vertical ( $D_V$ ) directions as represented in Figure 10. These values are extracted from the phase images through a correspondence pixels/mm by considering the reference target.

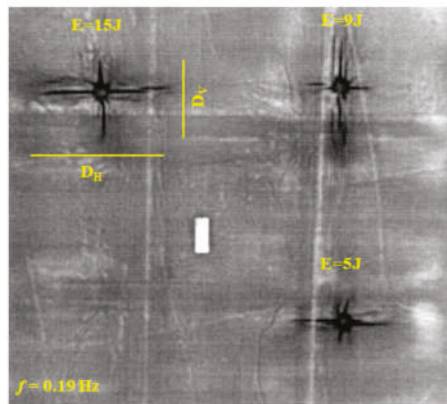


**Figure 10.** Indication of  $D_H$  and  $D_V$  over a phase image.

$D_H$  and  $D_V$  values are supplied only for PPB (Table 2) and PC2B (Table 3) specimens for which the most important damage develops along well-defined directions.

**Table 2.** Values of  $D_H$  and  $D_V$  for the PPB specimen through LT testing.

| $E$ (J) | $D_H$ (mm) | $D_V$ (mm) |
|---------|------------|------------|
| 5       | 40.0       | 24.0       |
| 9       | 46.0       | 54.0       |
| 15      | 75.4       | 42.0       |

**Table 3.** Values of  $D_H$  and  $D_V$  for the PC2B specimen through LT testing.

| $E$ (J) | $D_H$ (mm) | $D_V$ (mm) |
|---------|------------|------------|
| 5       | 58.0       | 24.0       |
| 9       | 38.0       | 74.6       |
| 15      | 75.4       | 44.0       |

Instead, as already shown and described, the PA6B specimen displays patchy damage which cannot be simplified with its displacement in the two directions only; therefore, no measurements are reported for this specimen. Coming back to Tables 2 and 3 it is possible to see the tendency towards longer cuts on the PC2B specimen. This is reliable because improving the interface bond makes the material more brittle and prone to fractures.

#### 4. Data Discussion and Concluding Remarks

The obtained results lend themselves to several considerations:

- The investigated materials are susceptible to defects formation during manufacturing. These defects may include non-uniform distribution of matrix and may be ascribed to non-uniform distribution of temperature and application of pressure during the compression cycle. This is likely to occur because of the compression performed in a press.
- Both lock-in thermography and ultrasonic testing can discover either impact damage, or manufacturing defects in PA6 matrix-based specimens with a general data agreement. This is well documented by a comparison between Figures 3 and 4.
- Polypropylene/basalt specimens being hydrophilic get soaked with the coupling gel and cannot be inspected with gel-based UT. Instead, lock-in thermography, acting in a remote way without any contact, is well suited and effective to detect both manufacturing defects and impact damage, also in polypropylene-based specimens.
- Specimens involving PA6 as a matrix display better mechanical properties and react to impact with less extensive damage with respect to specimens involving polypropylene as a matrix. This because both polyamide and basalt fibers have polar chemical structure, which enables proper interface adhesion even in the absence of a coupling agent. Instead, the a-polar nature of polypropylene requires the addition of coupling agents and/or any prior treatment of fibers to assure good interfacial adhesion.
- The presence of the coupling (compatibilizing) agent has no significant effects on the extension of the impact damage with regards to the branches length on the superficial layer but mostly affects the deformation way of the underlying layers. More specifically, a stronger interface adhesion entails a crumple effect with stretching of the bottom layer. This effect is evident looking at the phase images taken from the rear of specimens PA6B (Figure 9a) and PC2B (Figure 9c) in comparison with the phase image of the specimen PPB (Figure 9b), which appear almost flat.

On the whole, and by taking into account the points listed above, it seems preferable to build composites by embedding basalt fibers inside a polyamide matrix since the obtained composites seem to possess better characteristics and can be inspected with both LT and UT techniques. However, in some specific applications, polypropylene-based composites may be preferable relying on the use of infrared thermography for non-destructive evaluation. It is also worth noting that by means of specific

measures it is possible to improve manufacturing and guarantee surface waterproofing allowing testing with liquid-coupled probes. Of course, the choice of materials involves many other factors such as: performance, suitability, green aptitude, easy inspection, costs, etc., leading to a compromise.

**Author Contributions:** Conceptualization: All authors; specimens preparation: G.S.; impact tests: N.D.B. and E.M.; investigation with LT: S.B., and C.M.; software and data reduction: S.B.; investigation with UT: N.D.B., E.M.; data analysis and discussion: C.M., S.B., N.D.B., and G.S.; writing—original draft preparation: C.M.; revision: G.M.C.; all authors revised and approved the final version.

**Funding:** This research received no external funding.

**Conflicts of Interest:** The authors declare no conflict of interest.

## References

1. Collier, M.C.; Baird, D.G. Separation of a thermotropic liquid crystalline polymer from polypropylene composites. *Polym. Compos.* **1999**, *20*, 423–435. [[CrossRef](#)]
2. Fiore, V.; Scalici, T.; Di Bella, G.; Valenza, A. A review on basalt fibre and its composites. *Compos. Part B Eng.* **2015**, *74*, 74–94. [[CrossRef](#)]
3. Lopresto, V.; Leone, C.; De Iorio, I. Mechanical characterisation of basalt fibre reinforced plastic. *Compos. Part B Eng.* **2011**, *42*, 717–723. [[CrossRef](#)]
4. Sarasini, F.; Tirillò, J.; Valente, M.; Valente, T.; Cioffi, S.; Iannace, L. Sorrentino, Effect of basalt fiber hybridization on the impact behavior under low impact velocity of glass/basalt woven fabric/epoxy resin composites. *Compos. Part A Appl. Sci. Manuf.* **2013**, *47*, 109–123. [[CrossRef](#)]
5. Meola, C.; Boccardi, S.; Carlomagno, G.M.; Boffa, N.D.; Monaco, E.; Ricci, F. Nondestructive evaluation of carbon fibre reinforced composites with infrared thermography and ultrasonics. *Compos. Struct.* **2015**, *134*, 845–853. [[CrossRef](#)]
6. Vikas, G.; Sudheer, M. A Review on Properties of Basalt Fiber Reinforced Polymer Composites. *Am. J. Mater. Sci.* **2017**, *7*, 156–165.
7. Boccardi, S.; Boffa, N.D.; Carlomagno, G.M.; Del Core, G.; Meola, C.; Russo, P.; Simeoli, G. Inline monitoring of basalt-based composites under impact tests. *Compos. Struct.* **2019**, *210*, 152–158. [[CrossRef](#)]
8. Meola, C.; Boccardi, S.; Carlomagno, G.M. *Infrared Thermography in the Evaluation of Aerospace Composite Materials*; Woodhead Publishing Print Book: Sawston, UK, 2016; 180p, ISBN 9781782421719.
9. Busse, G. Optoacoustic phase angle measurement for probing a metal. *Appl. Phys. Lett.* **1979**, *35*, 759–760. [[CrossRef](#)]
10. Letho, A.; Jaarinen, J.; Tiusanen, T.; Jokinen, M.; Luukkala, M. Magnitude and phase in thermal wave imaging. *Electron. Lett.* **1981**, *17*, 364–365.
11. Beaudoin, J.-L.; Merienne, E.; Danjoux, R.; Egee, M. Numerical system for infrared scanners and application to the subsurface control of materials by photothermal radiometry. *Proc. SPIE* **1985**, *590*, 287–292.
12. Busse, G.; Wu, D.; Karpen, W. Thermal wave imaging with phase sensitive modulated thermography. *J. Appl. Phys.* **1992**, *71*, 3962–3965. [[CrossRef](#)]
13. *Advances in Phased Array Ultrasonic Technology Applications*; Manual; Olympus Scientific Solutions Americas (OSSA): Waltham, MA, USA, 2007.
14. Ensminger, D.; Bond, L.J. *Ultrasonics: Fundamentals, Technologies, and Applications*, 3rd ed.; CRC Press: Boca Raton, FL, USA, 2011.
15. Taheri, H.; Hassen, A.A. Nondestructive Ultrasonic Inspection of Composite Materials: A Comparative Advantage of Phased Array Ultrasonic. *Appl. Sci.* **2019**, *9*, 1628. [[CrossRef](#)]
16. Drinkwater, B.W.; Wilcox, P.D. Ultrasonic arrays for non-destructive evaluation: A review. *NDT&E Int.* **2006**, *39*, 525–541.



© 2019 by the authors. Licensee MDPI, Basel, Switzerland. This article is an open access article distributed under the terms and conditions of the Creative Commons Attribution (CC BY) license (<http://creativecommons.org/licenses/by/4.0/>).

# Toward Creating a Portable Impedance-Based Nondestructive Testing Method for Debonding Damage Detection of Composite Structures

Wongi S. Na \* and Ki-Tae Park

Sustainable Infrastructure Research Center, Korea Institute of Civil Engineering & Building Technology, Gyeonggi-Do 10223, Korea

\* Correspondence: wongi@kict.re.kr; Tel.: +82-31-910-0155

Received: 29 May 2019; Accepted: 29 July 2019; Published: 5 August 2019

**Abstract:** Debonding detection of composite structures is a vital task as such damage weakens the structure leading to a failure. As adhesive bonding is a more preferable choice over the conventional mechanical fastening method, detecting debonding as early as possible could minimize the overall maintenance costs. For this reason, a vast amount of research in the nondestructive testing field is being conducted as we speak. However, most of the methods may require well-trained experts or heavy equipment. In this study, the piezoelectric (PZT) material-based method known as the electromechanical impedance technique is investigated to seek the possibility of making the technique very cheap and portable by temporarily attaching the sensor. Furthermore, ANSYS simulation studies using smaller PZT patches as small as  $0.1 \text{ mm} \times 0.1 \text{ mm}$  are simulated to investigate the impedance signatures acquired from the simulations. The results show the possibility of using smaller PZT patches compared to the conventional PZT sizes of  $10 \text{ mm} \times 10 \text{ mm}$  for a successful damage identification process.

**Keywords:** debonding; composite damage; electromechanical impedance; piezoelectric; nondestructive testing; FEM simulation

## 1. Introduction

Detecting damage in composite materials is becoming more and more important with the increase in applications for composites. Up to date, there are many nondestructive testing (NDT) methods for evaluating the structural integrity of a target structure [1–9]. For composites, since bonding of two composite parts with adhesives is the preferred choice over the conventional mechanical fastening approach, detecting debonding is a crucial factor when maintaining a composite structure. Some of the recent studies in this area include effects of sensor debonding failure on mathematical representation of smart composite laminate [10], piezoelectric wafer guided wave-based debonding of carbon fiber reinforced polymer (CFRP) overlay in CFRP-reinforced concrete structures [11], and laser ultrasonic guided waves for detecting debonding of multilayered bonded composites [12]. Although various NDT methods are available for detecting damage, most of the methods require well-trained experts or heavy equipment to perform the procedure. For this reason, a low-cost, portable NDT system that is easy to use can be an important item in the field of NDT. Moreover, with advance in technology, efforts have been made by combining NDT with IoT (Internet of Things) technology, and a well-summarized work in this area can be found in [13].

The electromechanical impedance (EMI) technique is one of the NDT techniques that use a single piezoelectric (PZT) transducer to act as both actuator and sensor. The technique involves measuring the impedance below 500 kHz and monitoring the changes in the signature for damage identification. The one-dimensional equation first introduced by Liang et al. [14] shows that the electrical impedance

of the PZT transducer is directly related to the mechanical impedance of the host structure as shown below. Here, the electrical admittance,  $Y(\omega)$ , is a combined function of the mechanical impedance of the host structure,  $Z_s(\omega)$ , and the PZT transducer,  $Z_a(\omega)$ , respectively. This proves that any change in the host structure can be monitored by measuring  $Y(\omega)$ . Other variables in the equation,  $I$ ,  $V$ ,  $\omega$ ,  $a$ ,  $\epsilon_{33}^T$ ,  $\delta$ ,  $d_{3x}$ ,  $\bar{Y}_{xx}^E$  are the PZT output current, PZT input voltage, input frequency, geometric constant, dielectric constant, loss tangent, piezoelectric constant, and Young's modulus, respectively.

$$Y(\omega) = i\omega a \left( \epsilon_{33}^T (1 - i\delta) - \frac{Z_s(\omega)}{Z_s(\omega) + Z_a(\omega)} d_{3x}^2 \bar{Y}_{xx}^E \right) \quad (1)$$

Currently, there are three ways of conducting the EMI technique. The most-used one is by using an impedance analyzer (e.g., Agilent 4924a), which can measure impedance over 1 MHz depending on specification. However, such equipment can be very costly and weigh over 10 kg making it impractical for field use. Another way of conducting the EMI technique is by combining a function generator with an oscilloscope and using a simple circuit proposed by Peairs et al. [15]. Using this approach, one can conduct the EMI technique for a cost less than 25% compared to the conventional approach, and various authors have tested the reliability of this low-cost version. The cheapest way of conducting the EMI technique is by using the AD5933 evaluation board commercialized by Analog Devices Co. The small size of the device gives the possibility of creating a portable system for conducting the EMI technique. The cost of the AD5933 evaluation board can be as low as under 2% of the cost of the conventional impedance analyzer, which makes the EMI technique a very cheap technique to perform. However, one of the downsides of the device is that it can only measure impedance up to 100 kHz. Since one needs a signature with multiple peaks (e.g., resonance) to successfully identify damage, up to 100 kHz of frequency range might be not enough and could result in an impedance signature without any peak, resulting in failing to detect any damage. Especially for composite materials, due to its non-homogenous property, an impedance signature without any resonance can be commonly seen. To overcome this problem, the concept of sandwiching a metal disc between the PZT transducer and the host structure was proposed in [16], where its reliability was tested using glass fiber epoxy laminates.

To create a portable impedance measuring system, the way of attaching the PZT transducer must be changed. Since the EMI technique requires the PZT patch to be permanently attached to the host structure, one must alter this so that the PZT transducer can be temporarily attached and detached for multiple EMI measurements. The easiest way to achieve this would be to use a double-sided tape with the PZT-metal EMI transducer; the reliability and performance of this idea are tested in this study. In addition to the test, simulation studies on using PZT in smaller sizes are introduced.

## 2. Evaluation of the PZT-Metal Transducer Using Double-Sided Tape

The idea of the PZT-metal transducer proposed in [16] used a commercialized epoxy adhesive for attachment to the host structure. Thus, to make the PZT-metal transducer re-attachable, a simple idea of using a double-sided tape (purchased from [www.alpha.co.kr](http://www.alpha.co.kr)) is evaluated in this section against debonding and crack damage. Figure 1 shows the experimental setup to evaluate the performance of the PZT-metal transducer with double-sided tape attachment. The AD5933 evaluation board is connected to the laptop as shown in the figure where the positive and negative wires from the board are attached to the PZT-metal transducer by soldering. More details on the PZT-metal transducer with its damage detection performance can be found in [16]. For evaluating the performance of the PZT-metal transducer, two glass fiber epoxy laminates of 200 mm × 70 mm with 0.4 mm thickness were adhered to each other using a commercialized epoxy (Loctite Quick-set). After fully curing the epoxy for 48 h at room temperature, the impedance signature was measured from 25 to 75 kHz in 100 Hz steps to be used as a reference signature. Then, debonding was achieved by inserting a chisel tip between the two composite plates and separating them apart 10 mm at a time until 100 mm debonding was achieved. For each 10 mm of debonding, impedance signatures were measured. After 100 mm

debonding was achieved, the final impedance signature was measured with complete debonding of the bottom composite plate. The reason for this was to observe the difference in the impedance signature subjected to debonding that occurs away from the PZT transducer and which that occurs right below the PZT transducer. To check the reliability of the double-sided tape attachment approach, five identical tests (Test 1, Test 2, Test 3, Test 4, and Test 5) were conducted.

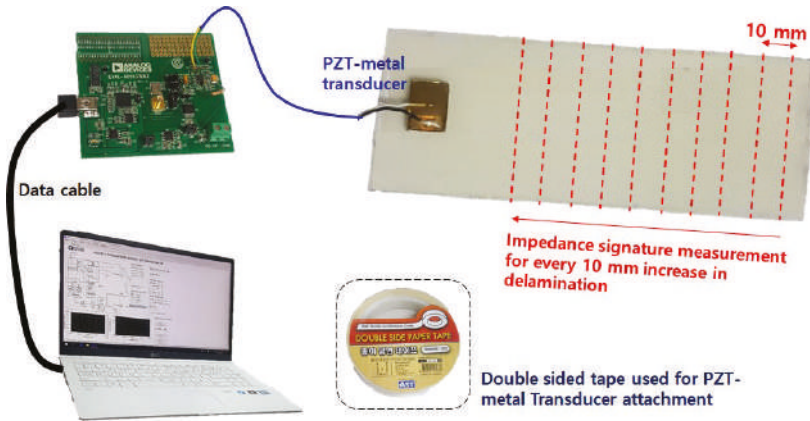


Figure 1. Experimental setup for the piezoelectric (PZT)-metal transducer experiment.

Observing Figure 2a, which represents the impedance signatures from Test 1, debonding has caused the amplitude peak (at 60 kHz) to decrease with increase in debonding area. However the amplitude remains virtually the same for the frequency range at 35 kHz where change is very difficult to see. However, when bottom composite plate is removed, the impedance signature peak increases dramatically at the 60 kHz resonance range. This experimentally proves that signature change is significant when debonding occurs below the PZT-metal transducer. Figure 2b shows the limitation of using the double-sided tape as the five impedance signatures seen in this figure were acquired by removing and reattaching the PZT-metal transducer onto the same area of the composite plate. The change is not significant but such change in signatures can cause false alarms when no damage has been experienced by the structure.

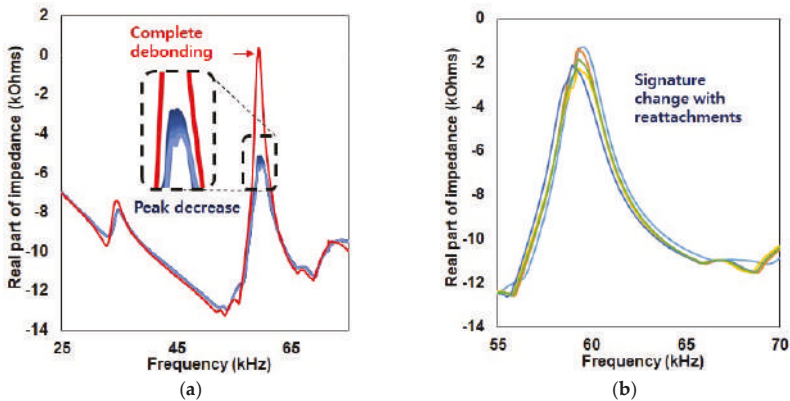


Figure 2. Impedance signature results for: (a) Debonding experiment; (b) re-attachable performance of the PZT-metal transducer.

For evaluating the damage detection performance, the variations between the reference and corresponding signatures (after damage) were quantified using root-mean-square deviation (RMSD) in equations below. In the equations,  $Re(Z_i)$  and  $Re(Z_i^o)$  represents the real part of the reference and the corresponding impedance signatures, respectively.

$$RMSD = \sqrt{\frac{\sum_N [Re(Z_i) - Re(Z_i^o)]^2}{\sum_N [Re(Z_i)]^2}} \tag{2}$$

Looking at Figure 3, the RMSD values with the reference signature being the intact case, the RMSD value was 0.6% with 1 cm debonding and increased to 1.37% with 5 cm debonding. However the RMSD values decreased down to 0.97% with 9 cm debonding. This shows the limitation of debonding detection using the PZT–metal transducer, where it seems that the highest value that can be obtained from this test is 1.37%. With full removal of the bottom composite plate, the RMSD resulted in 9.06%. Table 1 summarizes all the five test results including the data from Figure 3. Although the same tests were conducted, the RMSD results were different. With Test 2, all the RMSD values were below 1% and it was difficult to observe the increasing trend subjected to increase in debonding length. However, debonding below the PZT–metal transducer resulted in 10.29% once again proving that this NDT technique is effective at finding damage below the sensor. For Test 3, the increasing trend was clearly seen with increase in debonding length as the RMSD value started from 0.66% and rose to 2.31% with 8 cm debonding length. Here, the RMSD value with full removal of the bottom plate resulted in 10.98%, which shows that the reliability of finding defects located under a PZT–metal transducer is very effective. Tests 4 and 5 show similar results compared to Test 2 where all the RMSD values were below 1%, where the values generally increase with increase in debonding length. With full removal of the plate, the RMSD values were 11.9% and 15.32% for Tests 4 and 5, respectively.

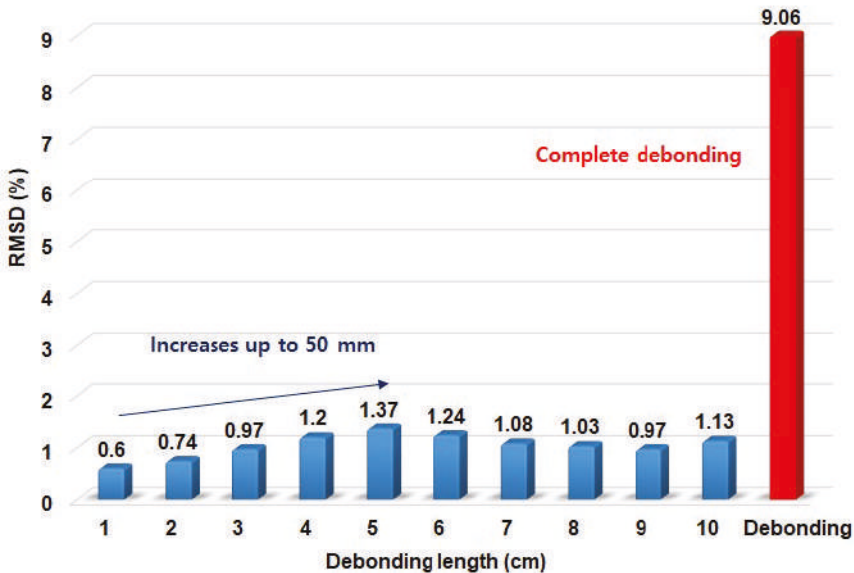


Figure 3. Root-mean-square deviation (RMSD) values for the debonding experiment and total removal of the bottom plate for Test 1.

**Table 1.** Summarized RMSD (%) values for the five tests.

|                           | Test 1      | Test 2       | Test 3       | Test 4      | Test 5       |
|---------------------------|-------------|--------------|--------------|-------------|--------------|
| 10 mm                     | 0.6         | 0.65         | 0.66         | 0.12        | 0.17         |
| 20 mm                     | 0.74        | 0.68         | 1.03         | 0.22        | 0.34         |
| 30 mm                     | 0.97        | 0.61         | 1.25         | 0.28        | 0.5          |
| 40 mm                     | 1.2         | 0.56         | 1.55         | 0.38        | 0.49         |
| 50 mm                     | 1.37        | 0.58         | 1.77         | 0.53        | 0.28         |
| 60 mm                     | 1.24        | 0.57         | 2.05         | 0.66        | 0.34         |
| 70 mm                     | 1.08        | 0.48         | 2.14         | 0.68        | 0.46         |
| 80 mm                     | 1.03        | 0.44         | 2.31         | 0.72        | 0.51         |
| 90 mm                     | 0.97        | 0.65         | 2.3          | 0.76        | 0.55         |
| 100 mm                    | 1.13        | 0.81         | 2.3          | 0.8         | 0.89         |
| <b>Complete debonding</b> | <b>9.06</b> | <b>10.27</b> | <b>10.98</b> | <b>11.9</b> | <b>15.32</b> |

### 3. FEM (Finite Element Method) Simulation for Smaller PZT Patches

From the previous section, although the PZT–metal transducer was able to detect debonding damage of composite plates, the impedance signature changed dramatically when debonding occurred below the attached PZT transducer. For this reason, various tests with smaller PZT sizes should be tested to validate the suitability of using smaller PZT transducers, as using smaller PZT could detect small debonding areas. However, using PZT in smaller sizes (compared to the conventional size of 10 mm × 10 mm with 0.5 mm thickness) would be very difficult to perform experimentally. For an example, it would be impossible to perform an EMI technique using a 0.1 mm square PZT as soldering of the positive and negative sides of the PZT would be difficult. Thus, to first check the reliability of the simulation, commercial FEM software ANSYS Workbench was used with coupled field analysis. Here, finite element couples the effects of interrelated physics within the element matrices making the electromechanical impedance simulation possible. In addition, the convergence criteria in ANSYS was unaltered as the program itself produced acceptable performance compared to the experimental result. Using ANSYS, a model representing the PZT–metal transducer used in the previous section with 6407 nodes and 1096 elements was created as shown in Figure 4. The average element quality was 0.959. In addition, the properties used for the PZT material can be seen in Table 2. The properties for the metal part of the PZT–metal transducer were selected from the ANSYS Workbench engineering database (stainless steel).

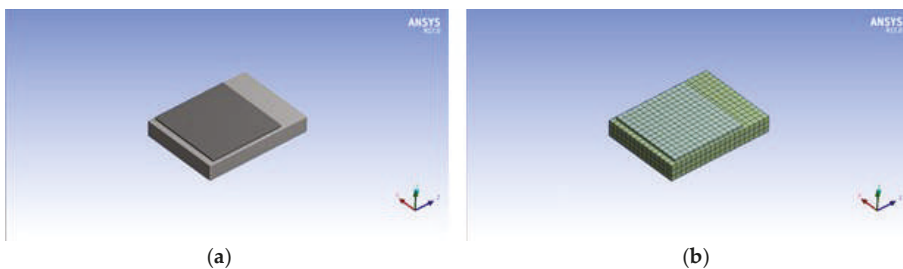


**Figure 4.** ANSYS FEM model: (a) PZT–metal; (b) mesh with 1096 elements.

Table 2. PZT properties for ANSYS simulation study.

| PSI-5A4E                                      |                                 |  |        |
|---|---------------------------------|--|--------|
| Density                                       |                                 |  | 7800   |
| Damping Ratio                                 |                                 |  | 0.0125 |
| Stiffness Matrix [ $c^E$ ]                    | $C_{11} = C_{22}$               |  | 152    |
|   | $C_{12}$                        |  | 102    |
|   | $C_{13} = C_{23}$               |  | 100    |
|   | $C_{33}$                        |  | 127    |
|   | $C_{44} = C_{55}$               |  | 21     |
|   | $C_{66}$                        |  | 25     |
| Piezoelectric Stress Matrix [ $e$ ]           | $e_{31} = e_{32}$               |  | -5.5   |
|   | $e_{33}$                        |  | 16.4   |
|   | $e_{24} = e_{15}$               |  | 12.4   |
| Electric Permittivity Matrix [ $\epsilon^S$ ] | $\epsilon_{11} = \epsilon_{22}$ |  | 950    |
|   | $\epsilon_{33}$                 |  | 890    |

Figure 5a shows the actual impedance signature of the PZT–metal transducer in air using the AD5933 evaluation board, and Figure 5b shows the impedance signature from the ANSYS simulation. Comparing both results, although the shapes of the signature are slightly different, the resonance frequency range from the FEM simulation result matches very well with the actual experimental result. Two large resonance peaks exist, where the larger one is located at around 65 kHz for both results (Figure 5a,b), and the smaller resonance peak for both signatures is located near 40 kHz. Furthermore, the amplitude of the large peak is around twice the size of the smaller resonance peak.

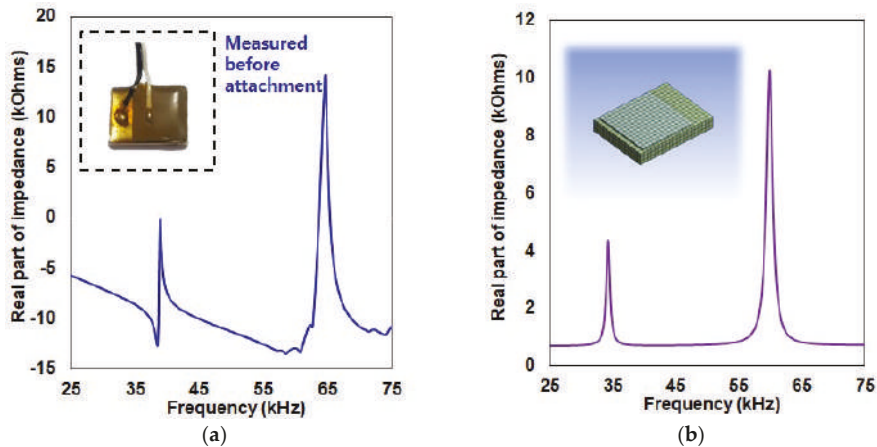


Figure 5. Impedance signature of the PZT–metal transducer before structure attachment: (a) By experiment; (b) by simulation.

Now that we had confirmed that the FEM simulation result was reliable, four more FEM models were created to evaluate the impedance signatures. PZT patches sizing from as small as 0.1–5 mm were created to investigate for resonance. Figure 6a shows the FEM model with a 0.1 mm × 0.1 mm PZT patch with 0.01 mm thickness attached to a square metallic material on the bottom (0.2 mm × 0.2 mm with 0.01 mm thickness), Figure 6b looks identical to Figure 6a but the size is 10 times larger. The PZT size is 1 mm × 1 mm with 0.1 mm thickness with the bottom metal plate of 2 mm × 2 mm with 0.1 mm thickness. Figure 6c has a 5 mm × 5 mm size PZT with 1 mm thickness and a metal size of 6 mm × 9 mm with 0.5 mm thickness. The last FEM model, Figure 6d, has the same dimension as the previous figure

but with the thickness of the metal plate increased to 1.5 mm. All four models were meshed with element quality over 0.9 to achieve the best outcome before obtaining the simulation results.

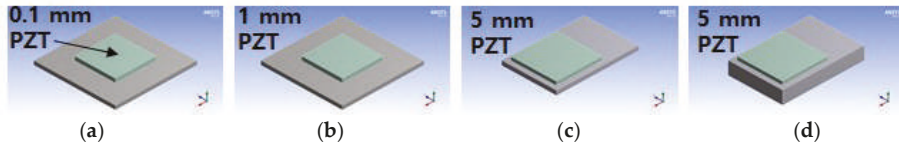


Figure 6. FEM model for smaller PZT sizes: (a) 0.1 mm PZT; (b) 1 mm PZT; (c) 5 mm PZT; (d) 5 mm PZT with thicker metal plate.

Figure 7 shows the impedance signatures acquired from the four FEM models in the frequency range 20–200 kHz. With the 0.1 mm square PZT patch (Figure 6a), there is no resonance at all. This suggests that using such a small PZT will possibly result in a failure when detecting damage unless resonance can be found over the 200 kHz frequency range. Observing the 1 mm square PZT patch (Figure 6b), it has the highest value compared to the rest of the signatures. Larger than the signatures with 5 mm square PZTs (Figure 6c,d). This shows that larger PZT size does not always result in bigger amplitude. The two impedance signatures for the last two FEM models have completely different frequency ranges. The thinner bottom metal layer FEM model resulted in multiple resonance range with five resonance peaks below 150 kHz, whereas the last FEM model with the thicker metal layer had two resonance peaks (very small one at 90 kHz and another one near 200 kHz). Although these simulation results were not verified with experimental results due to the fact that it is virtually impossible to conduct experiments with PZT sizes of 0.1 mm × 0.1 mm × 0.01 mm, the fact remains that PZT sizes smaller than 10 mm × 10 mm can be used to detect damage as long as resonance is found. Furthermore, changing the bottom metal plate can also create resonance to overcome the problem of resonance-free signatures, which may cause the EMI technique to fail at detecting damage.

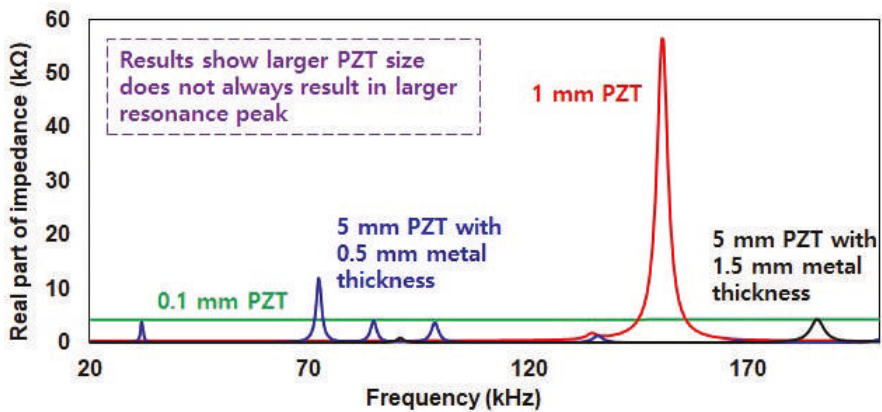


Figure 7. Simulation results for the impedance signatures of the four FEM models.

#### 4. Conclusions

In this study, a work toward creating a cheap and portable nondestructive testing (NDT) method known as the electromechanical impedance (EMI) technique was carried out. Since the EMI technique requires the brittle PZT patch to be permanently attached to the structure for damage detection analysis, the idea of making the attachment temporarily was tested using a double-sided tape. Such an approach made the PZT–metal transducer very easy to be attached and detached. In addition, regardless of the temporary attachment approach, debonding damage of a glass fiber epoxy composite could be

detected by monitoring the changes in the impedance signatures. However, this change was not as significant as the change subjected to debonding that occurred right below the PZT–metal transducer. This study experimentally showed that the debonding damage is best detected when it happens under the PZT patch. Therefore, to seek the possibility of detecting smaller debonding size, the size of the PZT patch had to be smaller than the conventional size of 10 mm × 10 mm with 0.5 mm thickness. Thus, the finite element analysis tool known as ANSYS Workbench was used to conduct simulations with smaller PZT patches as small as 0.1 mm × 0.1 mm with 0.01 mm thickness, virtually impossible to conduct experiment. Four different models were created with small PZT patches to find out that the size of the PZT was not the most important factor as the 1 mm square sized PZT patch showed resonance with highest peak amplitude.

Overall from this work, we found that the EMI technique can be made into a portable system, where the PZT transducer can be attached simply using a double-sided tape. Regardless of the damping effect, which may cause the impedance signatures to be less sensitive when subjected to damage, the results from this study have demonstrated its possibilities. Furthermore by conducting simulation studies, the PZT size can be further reduced for a successful debonding detection of composite structures.

**Author Contributions:** W.S.N. contributed in planning experiments and mainly writing the manuscript; K.-T.P. contributed in conducting experiments and analyzing data.

**Funding:** The research was supported by a grant from “Development of Safety Evaluation Techniques for Infrastructures by Micro–Macro Hybrid Monitoring Data (20190201-001)” funded by the Korea Research Institute of Standards and Science (KRISS).

**Conflicts of Interest:** The authors declare no conflict of interest.

## References

1. Palumbo, D.; Tamborrino, R.; Galietti, U.; Aversa, P.; Tati, A.; Luprano, V.A.M. Ultrasonic analysis and lock-in thermography for debonding evaluation of composite adhesive joints. *NDT E Int.* **2016**, *78*, 1–9. [[CrossRef](#)]
2. Na, W.S. Low cost technique for detecting adhesive debonding damage of glass epoxy composite plate using an impedance based non-destructive testing method. *Compos. Struct.* **2018**, *189*, 99–106. [[CrossRef](#)]
3. Gholizadeh, S. A review of non-destructive testing methods of composite materials. *Procedia Struct. Integr.* **2016**, *1*, 50–57. [[CrossRef](#)]
4. Na, W.S. Distinguishing crack damage from debonding damage of glass fiber reinforced polymer plate using a piezoelectric transducer based nondestructive testing method. *Compos. Struct.* **2017**, *159*, 517–527. [[CrossRef](#)]
5. Babu, J.; Sunny, T.; Paul, N.A.; Mohan, K.P.; Philip, J.; Davim, J.P. Assessment of delamination in composite materials: A review. *Proc. Inst. Mech. Eng. Part B J. Eng. Manuf.* **2016**, *230*, 1990–2003. [[CrossRef](#)]
6. Meola, C.; Boccardi, S.; Carlomagno, G.M. A quantitative approach to retrieve delamination extension from thermal images recorded during impact tests. *NDT E Int.* **2018**, *100*, 142–152. [[CrossRef](#)]
7. Giri, P.; Mishra, S.; Clark, S.M.; Samali, B. Detection of gaps in concrete–metal composite structures based on the feature extraction method using piezoelectric transducers. *Sensors* **2019**, *19*, 1769. [[CrossRef](#)] [[PubMed](#)]
8. Qing, X.; Li, W.; Wang, Y.; Sun, H. Piezoelectric transducer-based structural health monitoring for aircraft applications. *Sensors* **2019**, *19*, 545. [[CrossRef](#)] [[PubMed](#)]
9. Xie, L.; Gao, B.; Tian, G.Y.; Tan, J.; Feng, B.; Yin, Y. Coupling pulse eddy current sensor for deeper defects NDT. *Sens. Actuators A Phys.* **2019**, *293*, 189–199. [[CrossRef](#)]
10. Khan, A.; Kim, H.S. Assessment of sensor debonding failure in system identification of smart composite laminates. *NDT E Int.* **2018**, *93*, 24–33. [[CrossRef](#)]
11. Li, J.; Lu, Y.; Guan, R.; Qu, W. Guided waves for debonding identification in CFRP-reinforced concrete beams. *Constr. Build. Mater.* **2017**, *131*, 388–399. [[CrossRef](#)]
12. Zhang, K.; Zhou, Z. Quantitative characterization of disbands in multilayered bonded composites using laser ultrasonic guided waves. *NDT E Int.* **2018**, *97*, 42–50. [[CrossRef](#)]
13. Tokogonon, C.A.; Gao, B.; Tian, G.Y.; Yan, Y. Structural health monitoring framework based on Internet of Things: A survey. *IEEE Internet Things J.* **2017**, *4*, 619–635. [[CrossRef](#)]

14. Liang, C.; Sun, F.P.; Rogers, C.A. Coupled electro-mechanical analysis of adaptive material systems—Determination of the actuator power consumption and system energy transfer. *J. Intell. Mater. Syst. Struct.* **1997**, *8*, 335–343. [[CrossRef](#)]
15. Peairs, D.M.; Park, G.; Inman, D.J. Improving accessibility of the impedance-based structural health monitoring method. *J. Intell. Mater. Syst. Struct.* **2004**, *15*, 129–139. [[CrossRef](#)]
16. Na, S.; Lee, H.K. Resonant frequency range utilized electro-mechanical impedance method for damage detection performance enhancement on composite structures. *Compos. Struct.* **2012**, *94*, 2383–2389. [[CrossRef](#)]



© 2019 by the authors. Licensee MDPI, Basel, Switzerland. This article is an open access article distributed under the terms and conditions of the Creative Commons Attribution (CC BY) license (<http://creativecommons.org/licenses/by/4.0/>).

Article

# A Weighted Estimation Algorithm for Enhancing Pulsed Eddy Current Infrared Image in Ecp Non-Destructive Testing

Hanchao Li, Yating Yu \*, Linfeng Li and Bowen Liu

School of Mechanical and Electrical Engineering, University of Electronic Science and Technology of China, Chengdu 611731, China; lhc@uestc.edu.cn (H.L.); xhullf@163.com (L.L.); lbw9449@163.com (B.L.)

\* Correspondence: wzwytyt@uestc.edu.cn; Tel.: +86-136-7813-9939

Received: 31 July 2019; Accepted: 13 September 2019; Published: 9 October 2019

**Abstract:** Non-destructive testing (NDT) plays a crucial role in large scale industrial production such as in the nuclear industry and bridge structures where even a small crack can lead to severe accidents. The pulsed eddy current infrared thermography testing method, as a classic non-destructive testing technology, is proposed to detect cracks in the presence of excitation sources that cause temperature changes in the vicinity of defects, which is higher than normal area. However, in the vicinity of the excitation sources, the temperature is higher than normal even if there is no defect. Traditional infrared image enhancing algorithms do not work efficiently when processing infrared images because the colors in the images represent the temperature. To address this, a novel algorithm is proposed in this paper. A weighted estimation algorithm is proposed because each pixel value has a strong relationship with its neighboring pixels. The value of each pixel is determined by calculating the values of its neighboring pixels with a specific step-size and the correlation coefficients between them. These coefficients are obtained by calculating the differences between the pixels. The experimental results indicated that the outline of the welding defect became significantly clearer after being processed using the proposed algorithm, which can eliminate the errors caused by the excitation source.

**Keywords:** non-destructive testing evaluation; infrared thermography testing; defect detection; image enhancement

---

## 1. Introduction

Defects detection such as in bridges and nuclear structures testing, especially the small and surface/subsurface cracks detection, is the main target of non-destructive testing (NDT) [1–3]. These kinds of defects such as welding defect, which can cause severe accidents in large scale industrial production and transportation, have been studied for many years [4]. The application of new materials for industrial processes make it difficult to detect defects using traditional NDT methods such as eddy current testing (ECT) technology. For instance, with the application of new materials in modern aircraft manufacturing, composites are widely used to manufacture the key components of the aircraft. As a consequence, infrared thermography testing which is an important branch of NDT [5–7], is gaining attention as an efficient method for defect detection in new materials [8–10]. Compared to other NDT technologies, infrared thermography testing has significant advantages. It can be used to detect defects for various materials and geometries [11]. It can also be used for the detection and location of welding defects by collecting and processing infrared images [12–15].

Infrared thermography testing technology produces images that show the temperature distribution of the defects and the background [16].

The images are processed to collect as much information as possible to reconstruct the defects. Many researchers have done considerable amounts of work on the processing of infrared images [17,18].

The image processing approach can be classified into two categories namely spatial and frequency domain methods.

In spatial domain infrared image processing methods, the pixels of the image are manipulated directly. This is done by performing mathematical operations on each pixel and the surrounding pixels to obtain the gray value of the pixel. Common spatial domain image processing methods utilize sharp and smooth filters [19–21]. The fundamental purpose of the spatial domain processing method is to distinguish the defects from the background.

The frequency domain method transforms the image into frequency domain using a frequency transform methods such as the Fourier transform (FT) or wavelet transform (WT) [22]. The first step of the frequency domain image processing method is to convert the image into the frequency domain, after which the signal in the frequency domain is filtered. The frequency domain method yields low and high frequencies, which can be distinguished by a frequency transform of the infrared image. The low and the high frequency components are enhanced and suppressed respectively, such that the information of the defects in the image is made clearer.

However, most of the image processing methods only focus on the image itself, ignoring the significant differences between infrared and common images. In particular, infrared images do not show the actual scene being imaged. Instead, they show the distribution of temperature, which is influenced by excitation sources. In this paper, a method for enhancing infrared images is proposed. This method can eliminate the influence of the excitation source, and yield an infrared image with a clearer defect profile.

The essence of infrared thermography non-destructive testing technology is to obtain the temperature by measuring the amount of infrared radiation from the surface of an object. The common excitation sources of infrared thermography testing can be classified into three types: optical, electromagnetic, and mechanical excitation sources. In electromagnetic excitation sources, eddy current pulsed thermography (ECPT) is widely used as it can uniformly generate sufficient heat in a short time, and the heat it provides is generated from the eddy current induced from the excitation source. This allows the object to be heated evenly and makes the outline of the defect in the infrared image clearer [23].

The operating principle of eddy current pulsed thermography can be explained as follows. A high-frequency alternating current is applied to the excitation coil, which induces an eddy current on the surface and inside the conductive object. The induced eddy current flows in the conductive object. The conduction of the eddy current is influenced by the size, shape, and position of the defect, as the eddy current is forced to flow around the defect [24].

Figure 1 shows the spreading process of the eddy current in an object containing a defect. The distribution of the eddy current is influenced by the defect. The eddy current is much denser the edge of the defect than it is in other regions without defects.

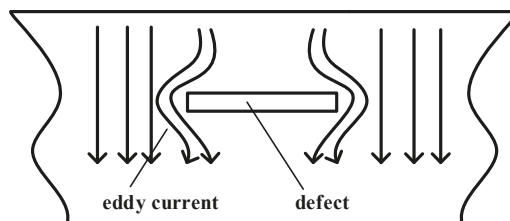


Figure 1. Eddy current at the edge of the defect.

The distribution of heat generated according to Joule’s Law is uniform, because the distribution of eddy current is uniform. Joule’s law is as follows:

$$Q = \frac{1}{\sigma} |J|^2 t, \tag{1}$$

where  $\sigma$  is the electrical conductivity of the object and  $J$  is the eddy current density,  $t$ . It is known from Joule's Law that the heat generated increases as the eddy current density increases.

An infrared thermal imager can detect and record thermal radiation on the surface and display it in the form of a temperature value in the infrared image. Figure 2 shows a schematic of the operating principle of the infrared thermal imager.

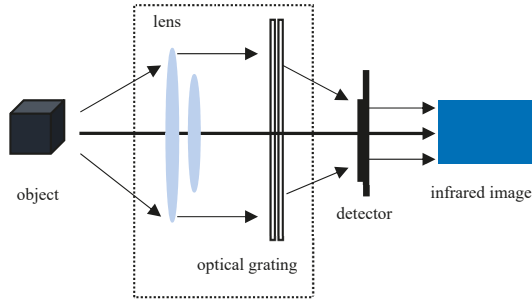


Figure 2. Operating principle of infrared thermal imager.

The different colors in the infrared image show the different temperatures on the surface of the object. A brighter region in the infrared image corresponds to a higher temperature on the surface of the detected object. The presence of an excitation source causes the infrared image collected in the experiment to differ from an image obtained under ideal conditions. However, most researchers have ignored the influence of the excitation source. An excitation source has a significant influence on an infrared image. The temperature of the surface in the presence of an excitation source is significantly higher than that of the surface far from the excitation source. We can find that there is a huge part whose size and shape is similar to the excitation source different from the background in the infrared image. Typically, the region influenced by the excitation source appears brighter in the infrared image, which means that the temperature is higher than the background without a defect underneath. If the defect is directly under the location of the excitation source on the surface, it is difficult to distinguish the defect. The area in the white box in Figure 3 is directly under the excitation source coil. There is a defect under the surface in the left box containing brighter colors. However, it is difficult to determine whether there is a defect inside the area in the right box, because its color is too similar to the background.

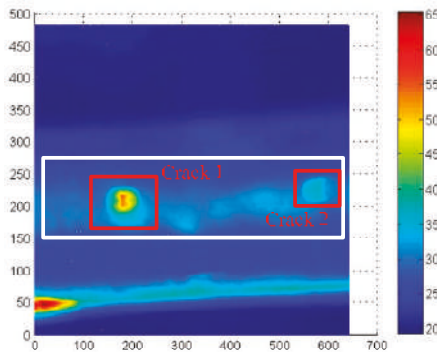


Figure 3. Infrared image.

The infrared image was meshed to analyze the temperature in the image. Figure 4 shows the temperature distribution of the image shown in Figure 3.

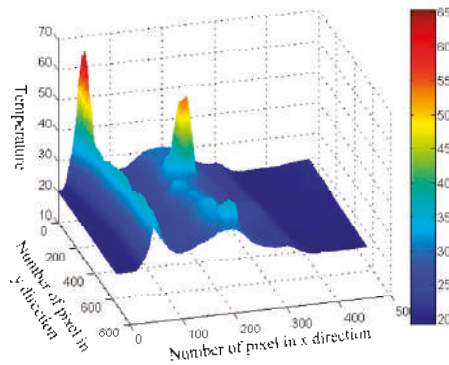


Figure 4. Meshed infrared image.

The temperature in the area directly beneath the excitation source was higher than that in other areas, causing a temperature swell to appear. The highest swell was caused by the defect in the left box in Figure 3. However, the swell caused by the defect in the right box in Figure 3 is not as clear because the excitation source is too large.

To eliminate the influence of the excitation source and make the defect profile clearer in the infrared image, several processing operations are proposed in this paper.

Several operations were applied to the pixels in the infrared image. We considered the value of a target pixel in the infrared image to be influenced by the neighboring pixels. The neighboring eight pixels were chosen to obtain the value of the target pixel.

## 2. Experiment Setup

In the infrared thermal imaging experiment, the specimen was heated to create different thermal distributions in the cracked and undamaged areas. A pulsed eddy current was applied to heat the material from the inside. In this way, the cracked area in the specimen produced considerably more heat than other areas. Generally, cracks distributed at different depths can be detected by NDT methods. The heat information at different depths depends on the rich frequency components during the pulsed eddy current excitation. Deep cracks could not be detected using infrared thermal imaging testing, because the heat transfer distribution became uniform over time as the heat was transferred from deeper regions to the surface. The experimental setup is shown in Figure 5.



Figure 5. Experimental setup.

Figure 5 shows that the excitation coil was restricted by the excitation controller. To detect deep cracks, the period of the square wave signal could be varied by the excitation controller. The specimen used in the experiment was a ferromagnetic material, and the cracks in it were artificial defects with depths of 0.1, 0.8, and 3 mm and width of 0.5 mm. The thermal imager and excitation controller could be simultaneously controlled by the computer (PC), where a 100 ms heating duration is selected for

inspection. This heating time is long enough to elicit an observable heat pattern. The excitation coil is 60 mm width placed above the specimen, and the distance between the thermal imager and specimen is about 600 mm. The signal flow chart in the experiment is shown in Figure 6.

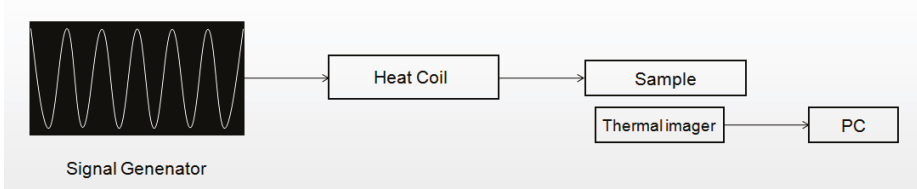


Figure 6. Signal flow chart.

### 3. Proposed Algorithm

The coordinate of the selected pixel is  $(i, j)$ . The pixel value is denoted as  $F(i, j)$ . The values of the neighboring eight pixels with the specified step-sizes are as follows:  $F(i - s, j - s)$ ,  $F(i - s, j)$ ,  $F(i - s, j + s)$ ,  $F(i, j - s)$ ,  $F(i, j + s)$ ,  $F(i + s, j - s)$ ,  $F(i + s, j)$ , and  $F(i + s, j + s)$ , which can be expressed in matrix form as follows:

$$P = \begin{pmatrix} F(i - s, j - s); \\ F(i - s, j); \\ F(i - s, j + s); \\ F(i, j - s); \\ F(i, j + s); \\ F(i + s, j - s); \\ F(i + s, j); \\ F(i + s, j + s); \end{pmatrix} \quad (2)$$

The model of the pixels in the infrared image is shown in Figure 7. The pixel value of a selected pixel,  $F(i, j)$  (yellow box in Figure 7), is considered to be related to the neighboring eight pixels, whose step-sizes are 2 (green boxes in Figure 7). For convenience, the neighboring pixels are expressed by  $a_i$ , arranged in clockwise order from the top left corner.

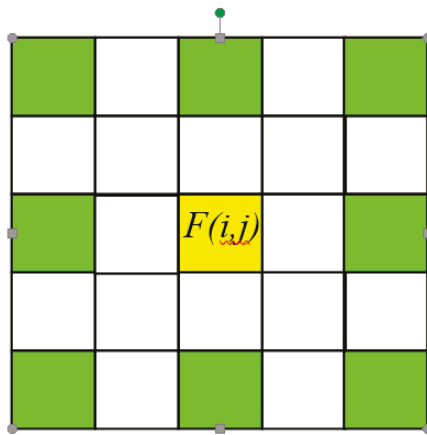


Figure 7. Model of pixels in infrared image.

To find the relationships between  $F(i, j)$  and the neighboring pixels, we subtract the values of neighboring pixels from the value of  $F(i, j)$  and arrange them in a column matrix,  $L$ , as follows:

$$L = \begin{pmatrix} X(i, j) - a_1 \\ X(i, j) - a_2 \\ X(i, j) - a_3 \\ X(i, j) - a_4 \\ X(i, j) - a_5 \\ X(i, j) - a_6 \\ X(i, j) - a_7 \\ X(i, j) - a_8 \end{pmatrix} \quad (3)$$

The differences between  $F(i, j)$  and the neighboring pixels shows the correlations between them. The correlation matrix,  $R$ , representing the correlation between the neighboring pixels is obtained from the difference matrix,  $L$ , as follows:

$$R = L \times L^T, \quad (4)$$

The differences between  $F(i, j)$  and the neighboring pixels are denoted as  $\Delta_1$ – $\Delta_8$ . After calculating the correlation between  $F(i, j)$  and the neighboring pixels, the value of  $F(i, j)$  is calculated as follows:

$$F(i, j) = \sqrt{\sum_{i=1}^8 \sum_{j=1}^8 \Delta_i \Delta_j a_i a_j} \quad (5)$$

Equation (5) can be written as follows:

$$F(i, j) = \sqrt{P^T \times R \times P}, \quad (6)$$

The value of  $F(i, j)$  obtained from the process above is not the exact value, as the sum of the correlation coefficients is not equal to 1. Thus, to obtain the real value of  $F(i, j)$ , the value above must be normalized as follows:

$$F(i, j) = \frac{F(i, j)}{\left(\sum_{i=1}^n \Delta_i\right)^2} \quad (7)$$

The infrared image can finally be obtained by calculating the value of every pixel using the method presented above.

#### 4. Results and Discussion

The infrared image analyzed is shown in Figure 3. The image was collected with the excitation source directly above the surface and two defects under it. The defect on the right side of the image is not clear.

By verifying the value of the step-size, we determined that the method was most efficient when the step-size was 8. Figure 8 shows the result when the step-size was 8. Compared with the initial infrared image, it is evident that the swell caused by the excitation source was eliminated.

Figure 9 shows the contrast between the processed infrared image and the initial image. The infrared image after processing was significantly clearer than the initial image. The bright area influenced by the excitation source was eliminated in the processed infrared image. Furthermore, the bright area in the right box was caused by the defect inside the object became clearer.

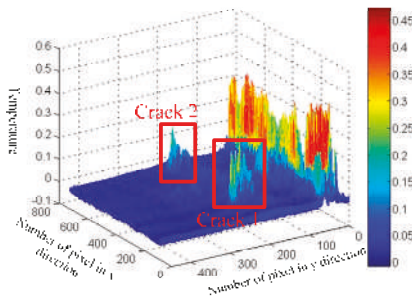


Figure 8. Meshed infrared image after processing.

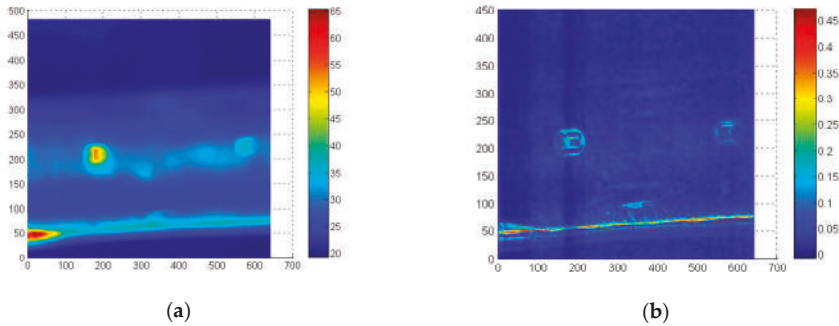


Figure 9. Comparison of initial and processed images: (a) Initial infrared image; (b) Infrared image after processing.

The swell in the infrared image caused by the excitation source was eliminated by using the algorithm provided in this paper. Furthermore, the outlines of the defects were made more distinct. The method presented in this paper improved the defect detection accuracy by enhancing the two crack images, and most importantly, it reduced the background noise which could increase the credibility of crack estimation compared with the original detected infrared image.

It should be noted that this algorithm is designed to reduce the background noise imported through the temperature of the environment and the excitation. Furthermore, in the pulsed eddy current infrared imaging test, multiple cracks will influence the distribution of the temperature so that the low temperature area of a crack will be covered in the background. This is because the thermal imager should adapt to the temperature in the whole vision area to make sure the image is clear. Thus, the proposed method is motivated by this problem. From the results, it can be inferred that when multiple cracks exist in the visible area, this method could reduce the influences produced by the thermal transforming. At stable temperatures, because the temperature between every two crack is similar and smooth but the temperature in the crack area is higher than that of the other areas, this method could be used.

### 5. Conclusions

A novel algorithm was proposed to enhance the infrared images by performing mathematical operations using pixel values with a specific step-size for the detection of welding defects. The pixel value was calculated using the neighboring pixels' values and the correlation between them. The relationship between the neighboring pixels was inferred from the differences between the target and neighboring pixel values. The correlation coefficients between the neighboring pixels were arranged in a matrix. The elements were multiplied by the corresponding pixel values and were subsequently summed and normalized, yielding a final pixel value. The method proposed in this paper

represents each pixel value using the neighboring pixels, eliminating swells in an infrared image due to an excitation source, which make the detection of defects significantly more difficult. The outline of the defect was found to be clearer when the processing was performed using the above-mentioned method.

**Author Contributions:** H.L. contributes to most of the results including modeling construction and analysis of the results, and he also completes the English writing of this paper. Y.Y. proposed the main idea of this article. L.L. and B.L. offer some help in processing data and draw diagrams.

**Funding:** This work is financial supported by the Fundamental Research Funds for the Central Universities under Grant ZYGX2018J067 and the Nature Science Foundation of Guangdong Province under Grant 2018A030313893.

**Conflicts of Interest:** The authors declare no conflicts of interest.

## References

1. Ebrahimkhanlou, A.; Athanasiou, A.; Hrynyk, T.D.; Bayrak, O.; Salamone, S. Fractal and Multifractal Analysis of Crack Patterns in Prestressed Concrete Girders. *J. Bridge Eng.* **2019**, *24*, 04019059. [[CrossRef](#)]
2. Ebrahimkhanlou, A.; Salamone, S.; Ebrahimkhanlou, A.; Azad, A.R.G.; Kreitman, K.; Helwig, T.; Williamson, E.; Engelhardt, M. Acoustic emission monitoring of strengthened steel bridges: Inferring the mechanical behavior of post-Installed shear connectors. In Proceedings of the Nondestructive Characterization and Monitoring of Advanced Materials, Aerospace, Civil Infrastructure, and Transportation XIII, Denver, CO, USA, 4–7 March 2019.
3. Ebrahimkhanlou, A.; Choi, J.; Hrynyk, T.D.; Salamone, S.; Bayrak, O. Detection of the onset of delamination in a post-Tensioned curved concrete structure using hidden Markov modeling of acoustic emissions. In Proceedings of the Sensors and Smart Structures Technologies for Civil, Mechanical, and Aerospace Systems 2018, Anaheim, CA, USA, 26–30 April 2018.
4. Tian, L.; Cheng, Y.; Yin, C.; Ding, D.; Song, Y.; Bai, L. Design of the MOI method based on the artificial neural network for crack detection. *Neurocomputing* **2017**, *226*, 80–89. [[CrossRef](#)]
5. Park, H.; Choi, M.; Park, J.; Kim, W. A study on detection of micro-Cracks in the dissimilar metal weld through ultrasound infrared thermography. *Infrared Phys. Technol.* **2014**, *62*, 124–131. [[CrossRef](#)]
6. Rodriguez-Martin, M.; Lagüela, S.; González-Aguilera, D.; Arias, P. Cooling analysis of welded materials for crack detection using infrared thermography. *Infrared Phys. Technol.* **2014**, *67*, 547–554. [[CrossRef](#)]
7. Dapeng, C.; Hongxia, M.; Zhihe, X. Infrared Thermography NDT and Its Development. *Comput. Meas. Control* **2016**, *4*, 1–6.
8. Plotnikov, Y.A.; Winfree, W.P. Advanced Image Processing for Defect Visualization in Infrared Thermography. *Proc. SPIE* **1998**, *3361*, 331–338.
9. Liu, Z.P.; Hu, L.H.; Zhou, J.M.; Cai, L. Evaluation of Surface Defect Area in Metal Based on Infrared Thermal Image. *Appl. Mech. Mater.* **2014**, *530*, 171–174. [[CrossRef](#)]
10. Min, Q.X.; Feng, F.Z.; Wang, P.F.; Zhang, C.S.; Zhu, J.Z. Recognition of contact interface defect in metal plate based on pulsed phase thermography. In Proceedings of the Prognostics & System Health Management Conference, Beijing, China, 21–23 October 2015.
11. Fan, C.F.C.; Sun, F.S.F.; Yang, L.Y.L. A general quantitative identification algorithm of subsurface defect for infrared thermography. In Proceedings of the 2005 Joint 30th International Conference on Infrared and Millimeter Waves and 13th International Conference on Terahertz Electronics, Williamsburg, VA, USA, 19–23 September 2005.
12. Meola, C.; Carlomagno, G.M. Recent advances in the use of infrared thermography. *Meas. Sci. Technol.* **2004**, *15*, 27. [[CrossRef](#)]
13. Maldague, X. Applications of infrared thermography in nondestructive evaluation. In *Trends in Optical Nondestructive Testing*; Elsevier Science: Amsterdam, NL, USA, 2000; pp. 591–609.
14. Avdelidis, N.P.; Hawtin, B.C.; Almond, D.P. Transient thermography in the assessment of defects of aircraft composites. *Ndt E Int.* **2003**, *36*, 433–439. [[CrossRef](#)]
15. Wang, X. Transient Thermography for Detection of Micro-Defects in Multilayer Thin Films. Ph.D. Thesis, Loughborough University, Loughborough, UK, 2017.

16. Chen, D.; Zhang, X.; Zhang, G.; Zhang, Y.; Li, X. Infrared Thermography and Its Applications in Aircraft Non-destructive Testing. In Proceedings of the 2016 International Conference on Identification, Information and Knowledge in the Internet of Things (IIKI), Beijing, China, 20–21 October 2016.
17. Li, H.J.; Lin, J.G.; Mei, X.; Zhao, Z. Infrared Image Denoising Algorithm Based on Adaptive Threshold NSCT. In Proceedings of the 2008 Congress on Image and Signal Processing, Sanya, China, 27–30 May 2008.
18. Ibarra-Castanedo, C.; Gonzalez, D.; Klein, M.; Pilla, M.; Vallerand, S.; Maldague, X. Infrared image processing and data analysis. *Infrared Phys. Technol.* **2004**, *46*, 75–83. [[CrossRef](#)]
19. Wang, J.; Hong, J. A new self-Adaptive weighted filter for removing noise in infrared images. In Proceedings of the 2009 International Conference on Information Engineering and Computer Science, Wuhan, China, 9–20 December 2009.
20. Voronin, V.; Tokareva, S.; Semenishchev, E.; Agaian, S. Thermal Image Enhancement Algorithm Using Local and Global Logarithmic Transform Histogram Matching with Spatial Equalization. In Proceedings of the 2018 IEEE Southwest Symposium on Image Analysis and Interpretation (SSIAI), Las Vegas, NV, USA, 4–10 April 2018.
21. Bai, J.; Chen, Q.; Wang, X.; Qian, W. Contrast enhancement algorithm of infrared image based on noise filtering model. *Infrared Laser Eng.* **2010**, *39*, 777–780.
22. Liu, T.; Zhang, W.; Yan, S. A novel image enhancement algorithm based on stationary wavelet transform for infrared thermography to the de-bonding defect in solid rocket motors. *Mech. Syst. Signal Process.* **2015**, *62*, 366–380. [[CrossRef](#)]
23. Yin, A.; Gao, B.; Yun Tian, G.; Woo, W.L.; Li, K. Physical interpretation and separation of eddy current pulsed thermography. *J. Appl. Phys.* **2013**, *113*, 064101. [[CrossRef](#)]
24. He, Y.; Pan, M.; Luo, F. Defect characterisation based on heat diffusion using induction thermography testing. *Rev. Sci. Instrum.* **2012**, *83*, 104702. [[CrossRef](#)]



© 2019 by the authors. Licensee MDPI, Basel, Switzerland. This article is an open access article distributed under the terms and conditions of the Creative Commons Attribution (CC BY) license (<http://creativecommons.org/licenses/by/4.0/>).

MDPI  
St. Alban-Anlage 66  
4052 Basel  
Switzerland  
Tel. +41 61 683 77 34  
Fax +41 61 302 89 18  
[www.mdpi.com](http://www.mdpi.com)

*Applied Sciences* Editorial Office  
E-mail: [applsoci@mdpi.com](mailto:applsoci@mdpi.com)  
[www.mdpi.com/journal/applsoci](http://www.mdpi.com/journal/applsoci)



MDPI  
St. Alban-Anlage 66  
4052 Basel  
Switzerland

Tel: +41 61 683 77 34  
Fax: +41 61 302 89 18

[www.mdpi.com](http://www.mdpi.com)



ISBN 978-3-03943-732-0